Aspects of air-sea interaction in atmosphere-ocean models

Dissertation
zur Erlangung des Doktorgrades
der Mathematisch - Naturwissenschaftlichen Fakultät
der Christian-Albrechts-Universität zu Kiel

vorgelegt von

Rafael Abel

Kiel, 2018

GEOMAR

Erster Gutachter: Prof. Dr. Claus Böning

Zweiter Gutachter: Prof. Dr. Peter Brandt

Tag der mündlichen Prüfung: 6.11.2018

Zum Druck genehmigt: 6.11.2018

_____

gez. Prof. Dr. Natascha Oppelt, Dekanin

Abstract

Air-sea interaction is governed by complex processes acting on a variety of spatial scales, which makes it extremely difficult to correctly represent these in ocean and atmosphere general circulation models. In this thesis some aspects of the representation of air-sea interaction in both forced ocean-only and coupled atmosphere-ocean models are being discussed from a new angle. Models of coarse and eddying resolution were used to demonstrate the effect of shortcomings and to present possible solutions to overcome these. Particular attention was paid to improving ocean hindcasts and the effect of mesoscale ocean features.

The main part of this thesis concerns the air-sea interactions in ocean-only models in which the atmospheric conditions are prescribed. The choice of a wind forcing for ocean-only models is not trivial: it is shown that due to imprints of ocean surface currents scatterometer-derived winds negatively bias the global wind power input by 30-40 GW. Wind forcing datasets like the JRA-55-do and the ERA-Interim reanalysis seem to be a better choice. Even if these products correct their winds with the scatterometer winds the negative biases from the scatterometer winds are not passed on to them.

Another issue in ocean-only models is the absence of the thermal feedback due to prescribed atmospheric conditions. In this study, a partial solution is tested using a simple thermally active atmospheric mixed layer model. A 50-year hindcast demonstrates the feasibility of this configuration with significant improvements in the heat fluxes compared to traditional configurations. Of particular importance is the increased strength of the temperature advection feedback associated with the Atlantic Meridional Overturning Circulation.

The mechanical feedback to the atmosphere is also absent in ocean-only models. In two global atmosphere-ocean models it is shown that the mechanical feedback appears to be spatially and temporally highly variable. Background wind speed and atmospheric stability are identified as the main factors for variability in mechanical air-sea coupling. Here, the mechanical feedback to the atmosphere was implemented in an ocean-only model and has led to significant improvement in the total mechanical coupling.

Chapter 4 assesses the relevance of mesoscale ocean imprints on the air-sea fluxes. It shows that mesoscale imprints are already important for the damping of ocean currents at eddy-permitting ($1/4°$) resolution. Switching off the mechanical damping leads to an increase in kinetic energy by 30-50% in western boundary current regions such as the Gulf Stream, Kuroshio and Agulhas regions. The thermal damping is of less importance with kinetic energy modifications of 10-25% for the same regions.

Chapter 5 demonstrates that resolution differences between the oceanic and atmospheric grid common among CMIP6-class models can lead to errors in the air-sea fluxes that in particular hamper the thermal and mechanical damping mechanisms for the surface ocean currents. Consequently, the kinetic energy increases by regionally by up to 13% and globally by about 6%. Strong localized heat flux errors do impact the mean heat uptake neither regionally nor globally. Large scale changes in heat transport and temperature distribution are found to be small.

Zusammenfassung

Wechselwirkungen an der Ozean-Atmosphäre Grenzschicht werden durch komplexe Prozesse verursacht, die auf unterschiedlichsten Raum- und Zeitskalen stattfinden. Deswegen sind diese Prozesse nur unzureichend in Ozean und Atmosphären Zirkulationsmodellen repräsentiert. In dieser Arbeit werden einige Aspekte der Ozean-Atmosphären Wechselwirkungen in angetriebenen Ozeanmodellen und gekoppelten Ozean-Atmosphäre Modellen aus einem neuen Blickwinkel betrachtet. Modelle mit grober Auflösung und teilweise Wirbel-auflösende Modelle werden benutzt um Folgen aus Modelldefiziten aufzuzeigen und mögliche Lösungen zu testen.

Der Hauptteil dieser Arbeit beschäftigt sich mit den Ozean-Atmosphären Wechselwirkungen in angetriebenen Ozeanmodellen, in denen die atmosphärischen Bedingungen vorgeschrieben sind. Es zeigt sich, dass die Wahl des Windantriebes nicht trivial ist: zum Beispiel beinhalten aus Scaterometrie abgeleitete Winde Abdrücke der Ozeanoberflächenströmungen. Dies führt dazu, dass die Windarbeit global um 30-40 GW reduziert wird, wenn man diese Winde benutzt. Eine bessere Wahl scheinen Windantriebsdatensätze wie die JRA-55-do und ERA-Interim zu sein. Auch wenn für diese mit den Scaterometrie-Winden korrigiert werden, gibt es keinen Übertrag der Reduzierung der Windarbeit in diese Datensätze.

Ein weiteres Problem in angetriebenen Ozeanmodellen ist die fehlende Wärmewechselwirkung wegen der vorgeschriebenen atmosphärischen Bedingungen. In dieser Arbeit wird eine partielle Lösung mit einem einfachen wärme-aktiven atmosphärischen Grenzschichtmodell getestet. In einer 50 Jahre langen Simulation wird die Durchführbarkeit gezeigt und dass der Ansatz zu einer deutlichen Verbesserung der Wärmeflüsse führt. Ein weiterer wichtiger Aspekt ist, dass sich die Stärke der Temperaturadvektionswechselwirkung in Zusammenhang mit der meridionalen Umwälzbewegung im Atlantik erhöht.

Ebenfalls fehlt die Impulswechselwirkung zur Atmosphäre in angetriebenen Ozeanmodellen. In zwei globalen Ozean-Atmosphäre Modellen wird gezeigt, dass die Impulswechselwirkung räumlich und zeitlich stark variabel ist. Als Hauptgründe für die Variabilität wurden die Hintergrundwindgeschwindigkeit und die Stabilität der Atmosphäre identifiziert. Die Impulswechselwirkung zur Atmosphäre wurde in das angetriebene Ozeanmodell implementiert und führt dazu, dass sich die Impulswechselwirkung im Allgemeinen deutlich verbessert.

In Kapitel 4 wird die Wichtigkeit von mesoskaligen Ozeananomalien auf die Ozean-Atmosphärenflüsse bewertet. Es wird gezeigt, dass schon ab einer Auflösung von $1/4°$ die mesoskaligen Ozeananomalien eine wichtige Rolle für die thermische und mechanische Dämpfung von Ozeanströmungen spielen. Wenn die mechanische Dämpfung ausgeschaltet wird, erhöht sich die kine-

tische Energie in den westlichen Randstromregionen wie der Golfstrom-, der Kuroshio- und der Agulhasregion um 30-50%. Bei der thermischen Dämpfung sind die Effekte schwächer und führen zu einer Erhöhung von 10-25% für dieselben Regionen.

In Kapitel 5 wird gezeigt, dass Auflösungsunterschiede zwischen den Ozean- und Atmosphärenkomponenten, die häufig in CMIP6-Kategorie Modellen zu finden sind, zu Fehlern in den Ozean-Atmosphäreflüssen führen und insbesondere die thermische und mechanische Dämpfung der Ozeanströmungen verringern. Infolgedessen erhöht sich die kinetische Energie regional um bis zu 13% und global um ungefähr 6%. Lokal wurden starke Änderungen des netto Wärmeflusses festgestellt, die regional und global aber kaum Einfluss haben. Großskalige Änderungen des Wärmetransports und der Temperaturverteilung sind gering.

Contents

1 Introduction

The importance of the air-sea interface for the Earth's climate cannot be overstated: almost all thermal and mechanical energy gain of the oceans happens through this interface. The processes that govern the exchange are complex and involve a host of parameters of the atmospheric and oceanic boundary layer. For most practical applications the air-sea fluxes are estimated in a simplified way by bulk formulations. In this simplified form, the turbulent bulk air-sea fluxes can be estimated by temperature, humidity and velocity differences between atmosphere and ocean. In computer simulations of the ocean and the atmosphere these turbulent fluxes can also be estimated even if the turbulence is not resolved. This has led to a more sophisticated air-sea flux representation in atmospheric and oceanic general circulation models. The air-sea interaction in these general circulation models forms the frame for this thesis. While there have been large improvements in the air-sea interaction in these models open questions remain and some will be addressed here. These questions concern details of the wind stress formulation and wind data to force ocean models, missing mechanical and thermal air-sea feedbacks, the role of small scale air-sea fluxes for the dynamics of the ocean and the air-sea coupling used in atmosphere-ocean models. These five questions are introduced in more detail in the following paragraphs and investigated in the following chapters of this thesis.

Before addressing the individual questions, the concept of *ocean-only models* needs to be introduced. Ocean-only models are dynamical computer models of the ocean, which means that the conditions of the other components of the climate system need to be prescribed. This is particularly important for the atmosphere as a main driver of the ocean. Prescribing atmospheric surface conditions does not allow for any feedbacks from the ocean to the atmosphere. Despite this deficit these models bear two important advantages: (1) They are 'in phase' with reality by using prescribed atmospheric conditions which are based on observations (details of atmospheric forcing data sets are given in chapter 2). This makes it possible to directly compare ocean-only simulations with observations of the ocean. The suppression of feedbacks between atmosphere and ocean additionally allows investigations of causes and consequences which are sometimes hard to distinguish in coupled systems. (2) Equally important is the consideration of computational feasibility: Atmospheric models with high horizontal resolution are typically more expensive than ocean-models with comparable resolution, especially in the case of spectral models using conventional Legendre transforms which become unreasonably expensive with increasing resolution as the computational complexity scales with $\mathcal{O}(N^3)$, where N is the cutoff spectral truncation

wavenumber, i.e. the resolution of the model. Therefore in ocean-only studies more resources can be invested in model resolutions that allow to capture important meso- and small-scale processes. However, the consequences of neglecting feedback mechanisms due to an unresponsive atmosphere in these models remain to be investigated.

The wind is one of the most important sources of energy for the ocean. That energy is brought into the ocean as a momentum flux driving currents and waves. Using boundary layer theory (e.g., Etling, 2008) this turbulent flux can be simplified to a function of the stability of the near-surface atmosphere and the wind speed. Early work (e.g., Large and Pond, 1982) had neglected the ocean surface current velocity as a bottom boundary condition, but more recent work (Hersbach and Bidlot, 2008; Large and Yeager, 2004) argue that not the wind speed, but the relative velocity between atmosphere and ocean should be used. Observations have also confirmed that the momentum flux depends on the relative velocity (Kelly et al., 2001; Cornillon and Park, 2001). Still today many modelling groups use the wind speed and neglect the ocean velocity. For the energy input the small ocean velocity can make a large difference: the consideration of the ocean velocity in the wind stress calculation reduces the wind power input by up to 30% for the large scale circulation (Duhaut and Straub, 2006; Zhai and Greatbatch, 2007; Hughes and Wilson, 2008; Scott and Xu, 2009). Another aspect to consider here, however, is that in forcing datasets for ocean-only models the wind data are often 'corrected' by 'observed' wind products which may contain imprints of ocean surface currents. A spurious imprint of ocean surface currents in forcing datasets could significantly change the wind power input into in the simulated ocean currents. Given various procedures of wind correction (Large and Yeager, 2009; Dee et al., 2011) it is not clear how strong the imprint of surface currents in forcing datasets actually is. This leads to the first scientific research question, adressed in chapter 2 (**Q1**): Is there an imprint of the ocean surface currents in common forcing datasets?

The next topic is closely related to the former: the logical consequence of a reduced energy input into the ocean if the relative velocity is considered is that more energy remains in the atmosphere. This remaining energy may result in an increase of the 10m wind by 30-50% of the ocean current (Renault et al., 2016c, 2017b). This is a small contribution of a few tens of cm s^{-1} when compared to the near-surface winds that can be easily between 10 and 20 ms^{-1}. However, for the wind power input it can be a quite important increase as the anomalous wind points in the same direction as the ocean current. Such a mechanical feedback is not present in ocean-only models as a result of prescribed atmospheric conditions. Recently Renault et al. (2016c) proposed a simple tweak in the wind stress calculation that allow for the feedback in ocean-only models. The feedback and the tweak need to be further investigated in chapter 3, addressing to the following question (**Q2**): Can the air-sea coupling in global ocean-only models be improved by a simple modification of the bulk formulation for the momentum flux (wind stress)?

The principal role of the air-sea fluxes is the heat transfer between ocean and atmosphere, and the mechanical energy input into the ocean by the winds. But the air-sea fluxes also play a role in the damping of ocean currents. In the presence of ocean currents the wind power input is reduced, resulting in a reduction of currents and a more realistic representation of the ocean dynamics (e.g., Dewar and Flierl, 1987; Renault et al., 2016b, 2017b). This process is called *mechanical damping*. Recent findings, however, suggest that mesoscale turbulent heat fluxes also play an important role in the ocean dynamics by providing a significant *thermal damping* (Ma et al., 2016). A direct comparison of the mechanical and thermal damping however is missing, leading to the question addressed in chapter 4 (**Q3**): What is the relative importance of the thermal and mechanical damping for the ocean dynamics?

Coupled atmosphere-ocean models are powerful tools to investigate long-term climate variability and provide useful future projections. Constraints in computational complexity of spherical atmospheric models have let to a discrepancy in the horizontal resolution between the atmospheric and oceanic component with the ocean being better resolved. This makes the air-sea flux calculation between the atmospheric and oceanic model non-trivial and often requires interpolation from a finer oceanic grid to an coarser atmospheric grid. This interpolation, however, leads to a loss of information of small scale oceanic features hampering the thermal and mechanical damping. In chapter 5 this question is addressed (**Q4**): What are the consequences for the simulation of the ocean if the oceanic component is better resolved than the atmospheric component in a atmosphere-ocean models?

The last topic concerns the need to prescribe atmospheric temperature and humidity in ocean-only models. In such a case the atmospheric temperature and humidity cannot adjust to the underlying SST. This is particularly important when deficiencies in the ocean-models result in Sea Surface Temperature (SST) biases (Wang et al., 2014; Flato et al., 2014). Then unrealistic heat fluxes are driving the ocean. One example is a too zonal North Atlantic Current which is common among ocean models with moderate resolution. This results in a large scale SST and heat flux bias on the order of a few $°C$ and tens of $W\,m^{-2}$, respectively. Another well-known example is the temperature advection associated with the Atlantic Meridional Overturning Circulation (AMOC): The prescribed atmospheric conditions in ocean-only models have a strong hold on the North Atlantic SST, i.e. damping the SST anomalies that would result from anomalous advection. This results in a reduction of the positive *temperature advection feedback* that describes the feedback between heat advection and convection (Rahmstorf and Willebrand, 1995; Lohmann et al., 1996). The latter studies demonstrated that the temperature advection feedback can be reintroduced in coarse ocean-only models using simple atmospheric models. In state-of-the-art ocean-only models the atmospheric conditions are still prescribed resulting in a too weak temperature advection feedback and generating overly sensitive AMOC conditions (Griffies et al., 2009). This forms the scientific research question addressed in chapter 6 (**Q5**): Can a simple

atmospheric mixed layer (AML) model reduce large-scale heat flux errors and re-introduce the temperature advection feedback in a state-of-the-art ocean-only model?

2 The momentum flux forcing of ocean models: Background and imprints of ocean currents in wind forcing data sets

This chapter summarizes the arguments for using the relative velocity between wind and ocean currents in the momentum flux calculation — an important aspect for the fidelity of the ocean simulation. Additionally it focuses on the choice for the wind forcing of the momentum flux calculation. This chapter reports on the imprints of ocean currents in QuikSCAT derived winds that lead to a negative bias in the power input to the ocean. Furthermore it addresses the question if the wind correction processes of the forcing products ERA-Interim and JRA-55-do contain similar imprints of ocean currents.

Contents

2.1 Introduction

The main source of energy for the ocean are winds. The energy transfer from the atmosphere to the ocean is mostly related to small-scale turbulence in atmosphere. However, it is possible to estimate this energy transfer based on properties of the the mean flow, i.e. near-surface winds and surface ocean currents (e.g., Large and Pond, 1981). Therefore even models that generally do not resolve such small-scale turbulence like General Circulation Models (GCM) can estimate the energy transfer. GCMs with only an ocean component, *ocean-only models*, thus require information of the near-surface winds. However, the choice of the wind forcing is not trivial and some open questions related to that form the frame of this chapter.

The most reliable and realistic wind forcing would be based on direct observations. Unfortunately, in particular over the ocean direct wind observations are sparse. Wind measurements over the oceans are available from satellite-mounted scatterometers, but they actually depend on the relative motion between the winds and the surface currents (Kelly et al., 2001; Cornillon and Park, 2001). To give some background on the functionality of scatterometers: by design scatterometers measure microwave radar backscatter from small scale waves on the ocean surface. The surface roughness and height of these waves are directly related to the wind stress, i.e. the force the winds exert on the ocean. Empirical retrieval algorithms or Geophysical model functions (GMF; e.g., Ricciardulli and Wentz, 2011) then attribute the backscatter signal to wind speeds and directions. However, the backscatter signal is related to the relative velocity between atmosphere and ocean and therefore scatterometer winds are actually the relative velocity between winds and surface currents. From this scatterometer wind one could readily and correctly estimate the wind stress that is applied to the real ocean. For ocean simulations this bears a problem: the surface current field in observations and in a simulation can exhibit large differences, in particular in regions that are not determined by steady mean currents. Therefore a spurious wind stress would be provided to the ocean simulation due to imprints of observed ocean currents in scatterometer winds. Thus adds an undesired source of error to the ocean model simulation when scatterometer winds are used as forcing (Xu and Scott, 2008).

More suitable and widely used wind forcing products are therefore often based on so called reanalysis models, which are atmospheric models initialized by synoptic observations and forced by realistic sea surface temperatures. In these reanalysis models the winds do not contain imprints of ocean surface currents . Some correct the winds on a long-term mean basis the ocean surface currents. It is, however, common practice to correct the winds in the forcing products with scatterometer winds (Large and Yeager, 2009; Kobayashi et al., 2015) or assimilate the winds directly (Dee et al., 2011). More details of the procedure are presented in appendix B. Even if the correction procedures vary, it is thought that the imprints of ocean surface currents present in the scatterometer winds are then brought into the forcing data sets (pers. comm. W.G. Large).

The aim of the study is to identify the imprints of ocean currents in forcing datasets. First it is shown that on small spatial scales there are imprints of ocean currents in scatterometer winds that are absent in a coupled atmosphere-ocean model. This leads to negative signals in the wind work. Finally it is investigated if these imprints are found in forcing datasets.

2.2 Background on momentum flux

It is instructive to precede the analysis by a basic consideration about some pertinent aspects of the air-sea momentum flux in reality and in OGCMs. A detailed momentum flux derivation as for the bulk formulation is given in appendix A. It lays out, that ocean surface should be considered for the momentum flux calculation.
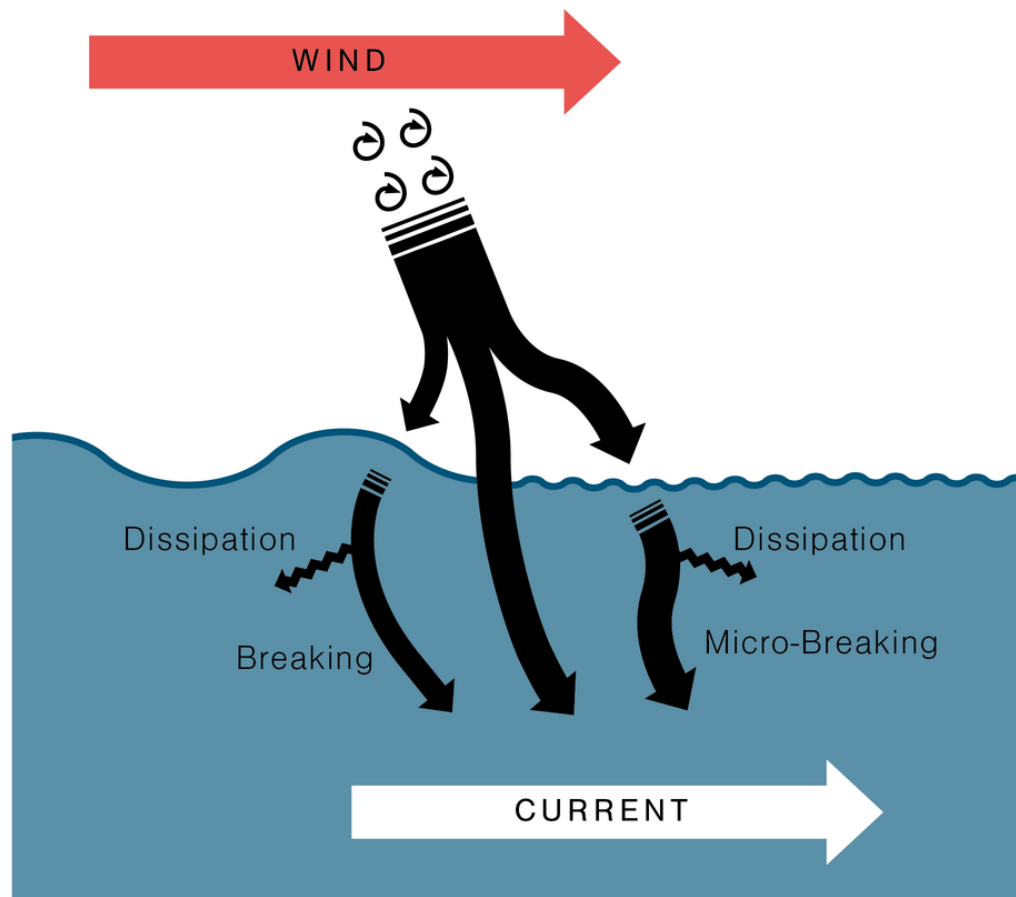
Figure 2.1: Schematic of the momentum transfer from the winds to ocean currents. Near-surface winds are associated with turbulence in the atmosphere that transfers energy downward into ocean waves and currents (depicted by black arrows from left to right). The long waves tend to have a longer life time and transfer energy non-locally to the current field. In a fully developed sea-state small waves transfer energy to the currents locally via mirco-breaking. All wave breaking processes are associated with energy loss to dissipation. Some part of the momentum flux is directly transferred to the ocean currents.

Energy of the mean winds is transferred to the ocean mainly by turbulence (e.g., Etling, 2008). This energy is then provided to two components of the ocean: waves and directly to the ocean currents (Csanady, 2001, ;schematic overview in Fig. 2.1). A large share is transferred to the short, centimeter-length waves that are well-known as surface ripples. These waves live only for a short time and provide shear-stress via micro-breaking to the ocean surface currents. A likewise large share is transferred to longer waves with wavelength larger than a meter. These waves can travel for tens to hundreds of kilometres until they ultimately break at a coast or in the open ocean. When they break in the open ocean momentum is transferred to the ocean currents as shear stress. Most energy of wave-breaking is transferred to the ocean currents and some energy is dissipated into mixing. Another part of the momentum flux is provided directly to the current fields as shear stress. All pathways are equally important, the exact split remains unknown, but depends on wind speed and wave age (Csanady, 2001).

2.2.1 Momentum flux in Ocean General Circulation models

As many other processes in the climate system also the momentum flux and the transfer to the ocean cannot be directly resolved in Ocean General Circulation Models (OGCMs), so that the air-sea flux, including the effect of waves on surface roughness and the force on the ocean need to be parameterized. The momentum flux, τ, is generally calculated using bulk formulations of the form:

$$\vec{\tau_{rel}} = \rho_a C_D |\vec{U}_a - \vec{u}_o|(\vec{U}_a - \vec{u}_o), \tag{2.1}$$

where ρ_a is atmospheric density, C_D the drag coefficient, U_a winds and u_o ocean surface currents. Among others the COARE (e.g., Fairall et al., 2003; Edson et al., 2013), ECMWF (ECMWF, 2014) and NCAR (e.g., Large and Pond, 1981; Large and Yeager, 2004) bulk algorithms are widely used. Note that the choice of the bulk formulation can account for up to 20% difference in the air-sea fluxes (Brodeau et al., 2017).

The transfer of energy to ocean waves is generally not accounted for in OGCMs as they are not coupled to a wave model. The effect of the waves on the sea surface roughness is parameterized following Charnock's law, i.e. $z_0 = \alpha u_*^2/g + 0.11\nu/u_*$. The Charnock coefficient is $\alpha \approx 0.011$, varying with sea-state, ν is the kinematic viscosity of air. COARE3.5 and the ECMWF bulk algorithms use the Charnock law (when ECMWF is not coupled to a wave model directly). The NCAR bulk formulation has an equivalent expression. However the expressions are significantly different (Fig. 10a in Brodeau et al., 2017), where the sea-state dependence in NCAR is much smaller.

Direct energy input into the wave field is generally not considered. For example in NEMO

(Madec, 2011) the wind stress is applied as a vertical diffusive flux at the first level of the ocean model in the form:

$$\left(\frac{A^{vm}}{e_3}\frac{\partial \vec{u}}{\partial k}\right)\bigg|_{z=1} = \frac{1}{\rho_0}\vec{\tau}, \tag{2.2}$$

where A^{vm} is the vertical eddy viscosity, e_3 the vertical grid resolution and k the depth level. Other widely used ocean models, like the MITgcm, POP, MPIOM and MOM have equivalent formulations (respectively, MITgcm code: http://mitgcm.org/download/; Smith et al., 2000; Marsland et al., 2003; Pacanowski and Griffies, 2000).

2.3 Data and Methods

2.3.1 QuikSCAT winds and windstress

Observational wind and wind stress measurements used here are from the QuikSCAT V3 product (CERSAT,IFREMER) on a 0.25° grid for the period from 2000 to 2009 (Bentamy et al., 2013). Scatterometers, like SeaWinds on QuikSCAT, actually measure radar backscatter which is due to centimeter-length surface waves which are generated by the wind stress. Therefore the scatterometer measures the wind stress exerted by the relative velocity between surface winds and surface currents. Using so called Geophysical Model Functions (GMF) the backscatter signal is processed to wind speeds and directions. An important part of this study is that the GMFs attribute the backscatter signal to the winds and neglect ocean surface currents. This means that the winds provided from QuikSCAT are actually the winds relative to a moving ocean.

The wind stress is estimated using the Large et al. (1994) bulk formulation. Note that in Fig. 2.2 and 2.3 the QuikSCAT V3 product wind stress is used. Error estimates of QuikSCAT winds are about 0.75 ms^{-1} for the along-wind and 1.5 ms^{-1} for the across-wind component (Chelton and Freilich, 2005). The product is provided at a spatial resolution of 0.25° but the effective resolution is about 1° (Desbiolles et al., 2017).

2.3.2 SLTAC geostrophic currents

Satellite altimetry provides useful information about the sea surface height. Given the sea surface height geostrophic currents can be calculated. The dataset used here is SLTAC geostrophic currents (former known as AVISO) that are readily calculated and have a horizontal resolution of 0.25° and temporal resolution of one day. Global Ocean Gridded L4 sea surface heights and derived variables were made available by E.U. Copernicus Marine Service (CMEMS). Reported error estimates range from 5 to 15 cm s^{-1} depending on sea surface variability. For this study data from 2000-2009 is used.

2.3.3 Coupled atmosphere-ocean model

The mechanical coupling is investigated in the eddying atmosphere-ocean model experiment GC2.1-N512O12, that employs the atmospheric Met Office Unified Model at N512 resolution ($\sim$25km) and ocean components based on Nucleus for European Modelling of the Ocean (NEMO; Madec, 2011) ORCA12, with a nominal resolution of $1/12°$. Turbulent surface fluxes in this model are calculated using a bulk formulation (Smith, 1988) with Charnock's coefficient of 0.018, using relative winds and coupling frequency of 1 hour. The atmospheric model has 85 vertical levels. Unresolved turbulent motions are parametrized to achieve realistic vertical structures in temperature and wind profiles (Walters et al., 2017). For an extensive documentation of the model configuration and a discussion of the impacts of a resolved ocean mesocale in the simulations the reader is referred to Hewitt et al. (2016). The model had been integrated for 19 years (year 20 experienced some data loss).

2.3.4 ERA-Interim and JRA-55-do

Forcing datasets for ocean circulation models are commonly based on reanalysis products which are essentially Atmospheric General Circulation Models forced by observed SST. ERA-Interim is the latest ECMWF reanalysis product with T255 resolution ($\sim$0.7°; Dee et al., 2011). The JRA-55-do forcing is based on the JRA-55-do reanalysis product (Tsujino et al., 2018, , 2018 submitted) and is available at TL319 resolution ($\sim$0.56°). Both the ERA-Interim reanalysis product and the JRA-55-do forcing winds have been corrected by QuikSCAT winds. This correction is described in more detail below. Wind stress from ERA-Interim and JRA-55-do wind is estimated using Large et al. (1994) bulk formulation in this study.

## 2.4 Imprints of ocean currents on Scatterometer winds

Scatterometers are designed to get estimates of surface winds over the oceans. However, they measure microwave radar backscatter from small scales waves at the ocean surface. As discussed above the height of these waves depends on the Reynolds stress due to winds on the surface ocean. The objective of the following analysis is to identify the signatures of surface currents on scatterometer wind stress and winds. While it has already been reported by Kelly et al. (2001) and Cornillon and Park (2001) that the wind speed derived from scatterometer measurements is the relative velocity between ocean and atmosphere, it needs to be emphasized that therefore scatterometer derived winds might lead to undesired results when used to force an ocean models. This is because the ocean surface current velocity inherent in scatterometer winds originates from an ocean state that differs largely from the ocean-model state. Therefore it would introduce spurious momentum fluxes, when used as a forcing.

First we have to recall that the wind stress equation (Eq. 2.1) describes the energy flux between the near-surface atmospheric winds and the ocean surface currents. For the ocean currents the wind stress is the top boundary condition and for the winds it is the bottom boundary condition. In order to highlight the influence of the ocean current (u_x, u_y) in the following the curl $(du_x/dy - du_y/dy)$ is discussed. So suppose there is a positive curl of the ocean current. This would result in a negative curl of the wind stress (if the influence of the winds is neglected) as $curl(\tau) \propto -curl(u^2)$. This negative wind stress curl would then also result in a positive wind curl, as the wind stress acts against the wind and therefore $curl(wind) \propto -curl(\tau)$. A positive curl of the wind results in a positive curl of the wind stress and a positive curl of the ocean current. In the following it is tested if these theoretical relation can be found in observed ocean currents, wind stress and wind and also in a coupled model.

The ocean current signals in scatterometer derived winds are thought to be most pronounced in regions with strong currents such as the Gulf Stream. Off the coast of Florida we find a strong positive curl in the surface current velocity (SLTAC geostrophic currents) on the left-hand side of the Gulf Stream and a negative curl on the right-hand side (Fig. 2.2a). The wind stress and the winds curl (both QuikSCAT) show a similar pattern but with reversed signs, i.e. the curl of the surface current is positive, when the curl of the wind stress and the wind are negative. This is in agreement with the theoretical arguments above. How strong this relationship is, can be defined by the coupling coefficient s_{st}, which is the slope of the linear regression between the curl of the ocean currents and the curl of the wind stress. For the Gulf Stream it is found to be $s_{st} = -0.56$ (Fig. 2.3a). We also note, that there is quite a large spread, but the measure s_{st} has already been used for other modelling studies (Renault et al., 2016a, 2017b) and for observations (Renault et al., 2017a). In these studies the spread had been masked using binned scatter plots.
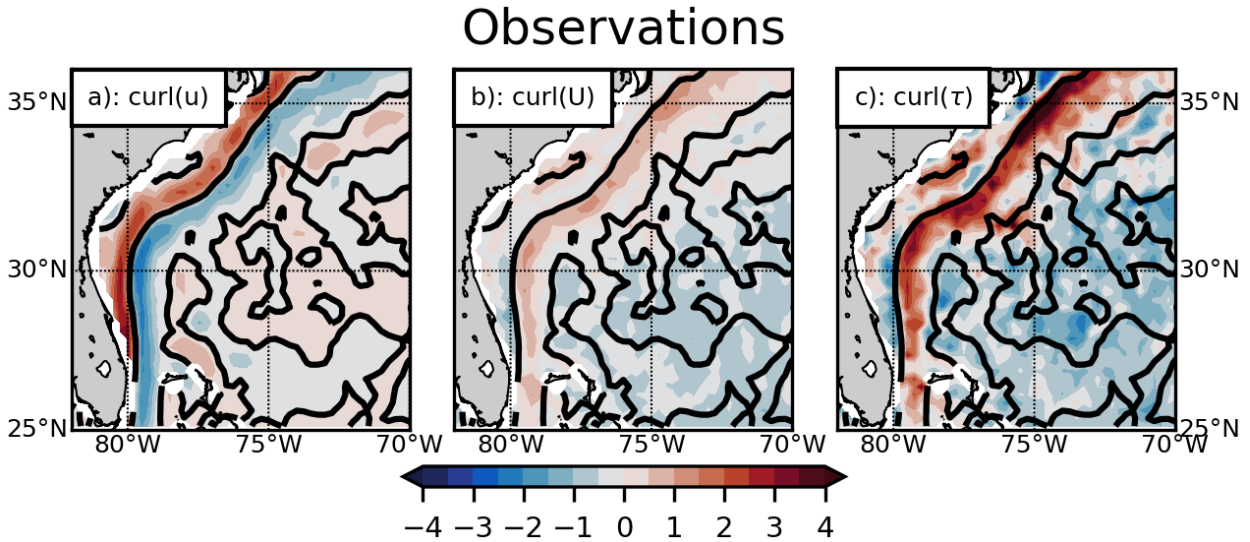
Observations

Figure 2.2: Relationship between ocean surface currents, wind stress and wind in observations. (a) curl of SLTAC geostrophic surface currents $[10^5 s^{-1}]$, (b) curl of QuikSCAT winds $[10^5 s^{-1}]$, (c) curl of QuikSCAT wind stress $[10^7 Nm^{-3}]$ time-mean for the year 2005. Black contours denote zero-line of the curl of SLTAC geostrophic currents. Note that all subplots share the same color-scale, but have different units.
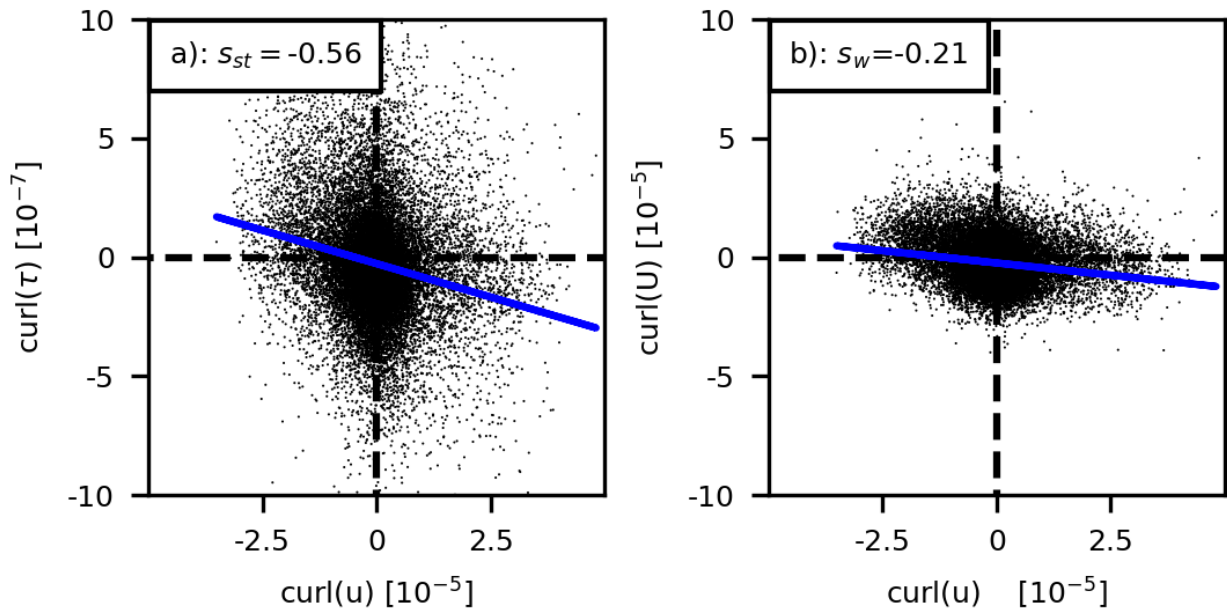
Figure 2.3: Relation between curl(u) and (a) curl(τ) and (b) curl(U) at 10 m over the Gulf Stream (25°-37°N and 83°-70°W) for SLTAC geostrophic surface currents and Quikscat winds for the year 2005. The slope of the linear regression between two components results in the coupling coefficients (a) s_{st} and (b) s_w.

For the relationship between the curl of the ocean surface currents and the curl of the wind another coupling coefficient can be defined: s_w is the slope of the linear regression between the curl of the ocean surface currents and the curl of the wind. We find that the ocean current signal is also present in the winds derived from scatterometer measurements and results in a negative coupling coefficient $s_w = -0.21$ for the Gulf Stream (Fig. 2.3b). This negative s_w apparently contradicts recent findings (Renault et al., 2016a, 2017b) and the theoretical arguments above

where a positive relationship has been found. This contradiction can be explained by the wind stress measurement technique used by scatterometers: scatterometers measure the wind stress which is a function of the wind minus the surface currents. By mistake the wind stress is then attributed to the wind alone neglecting the influence of the ocean currents. Therefore the relation s_w for scatterometer wind and SLTAC geostrophic currents is wrongly negative.

In an Atmosphere-Ocean GCM (here the Met Office GC2.1-N512O12) the momentum exchange between atmosphere and ocean is implemented by Eq. 2.1. This makes it a perfect test bed to investigate the relationship between the currents, winds and wind stress over the Gulf Stream. The ocean component does reproduce the pattern found in the observations of the curl of the ocean current with positive curl on the left-hand side and negative curl on the right-hand side of the Gulf Stream (Fig. 2.4). The pattern of the wind stress curl shows a similar large scale pattern like the observations and has a reversed sign with respect to the curl of the ocean currents, i.e. the relation expected from Eq. 2.1. A more quantitative picture is given by the scatter plots and the linear regression (Fig. 2.5). There a more concise (less spread) relationship s_{st}, which is also stronger than in the observations ($s_{st} = -1.17$). Unlike the observational relationship between the curl of the wind and the curl of the ocean currents the model gives a positive relation which is in agreement with the theoretical considerations ($s_w = +0.31$). This means that the wind curl is increased in the presence of a curl of the ocean currents.

Figure 2.4: Relationship between ocean surface currents, wind stress and wind in the coupled model GC2.1-N512O12. (a) curl of surface currents $[10^5 s^{-1}]$, (b) curl of 10m winds $[10^5 s^{-1}]$, (c) curl of wind stress $[10^7 Nm^{-3}]$. Black contours denote zero-line of the curl of SLTAC geostrophic currents. Note that all plots share the same color-scale, but have different units.
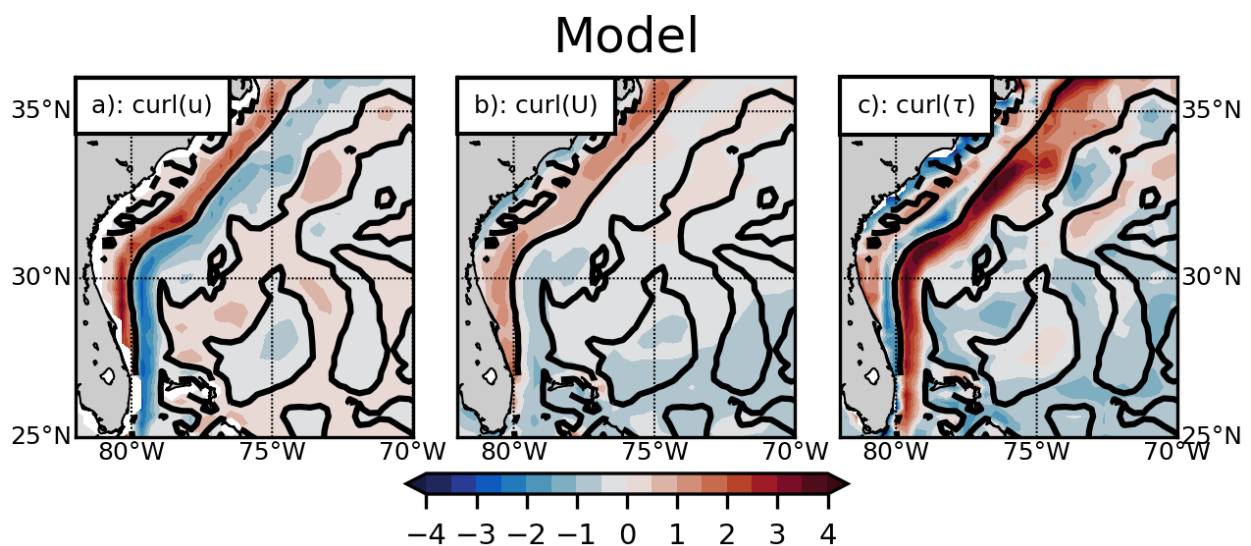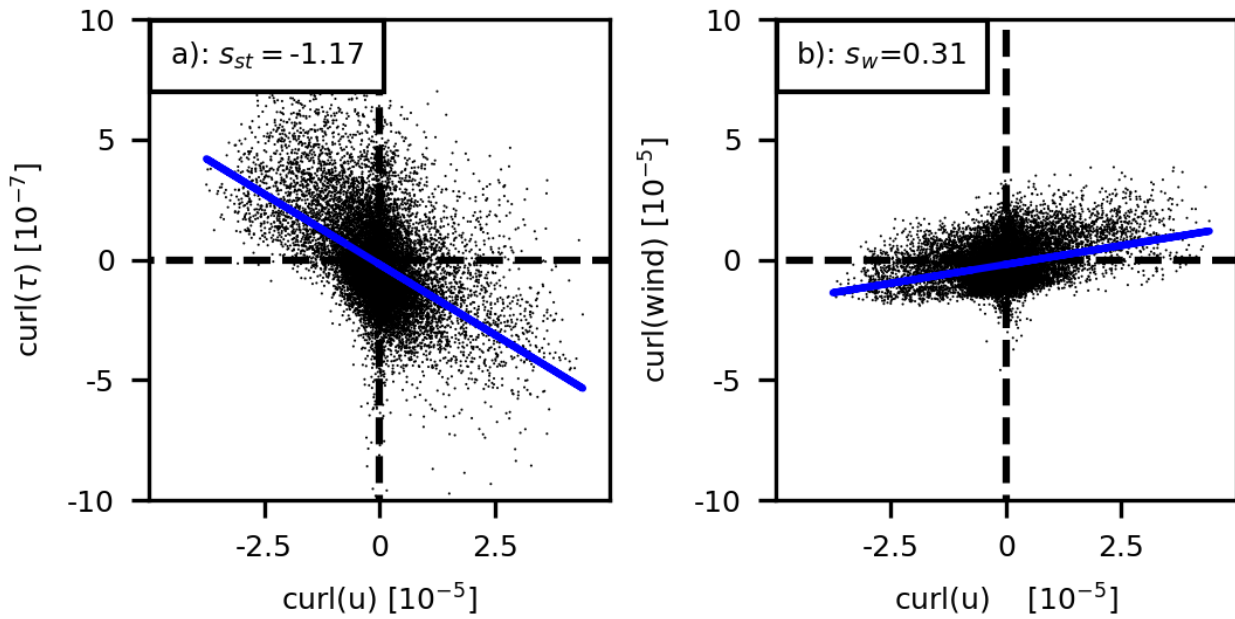
In combination, the contradictory results for the ocean current and wind relationship for the coupled model ($s_w = +0.31$) and the scatterometer derived winds ($s_w = -0.21$) expose a fun-

Figure 2.5: Relation between curl(u) and (a) curl(τ) and (b) curl(U) at 10m over the Gulf Stream (25°-37°N and 83°-70°W) in the coupled model GC2.1-N512O12. The slope of the linear regression between two components results in the coupling coefficients (a) s_{st} and (b) s_w.

damental issue, namely the imprints of ocean currents in the scatterometer derived winds. In the next section we will see that this issue is particularly problematic for the wind work. There due to these imprints ocean the ocean currents the wind work is negatively biased.
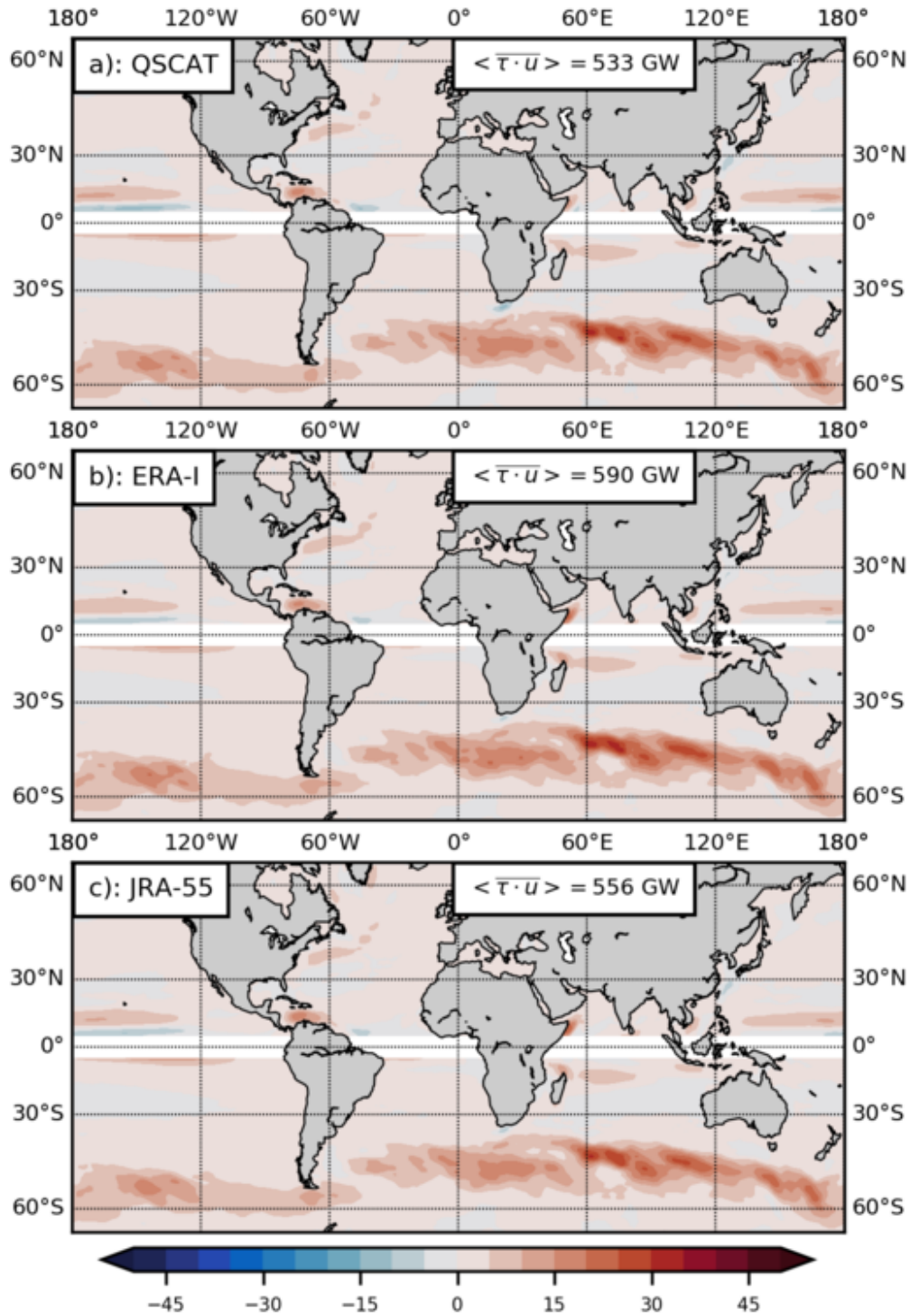
2.5 Wind work

The wind stress acts on the ocean and does work on the currents. This wind work is defined by the dot-product between the wind stress and the surface currents, $\vec{\tau} \cdot \vec{u}$. The aim of this section is to show that there are substantial differences in the time-mean wind work estimated with different forcing datasets. Note that the wind work is estimated using the absolute wind, i.e. neglecting ocean currents in the wind stress. Additionally the time-dependent and small-scale components of the wind work will be used to carve out the imprints of the ocean currents.

The time-mean wind work is mostly positive, i.e. the ocean gains energy and by far the most is gained in the Southern Ocean, but also in parts of the western boundary currents (Fig. 2.6a). There are also regions where the wind work is negative when the prevailing winds blow against the mean current, e.g. the equatorial counter currents that flow against the trade winds. The global time-mean integral wind work for QuikSCAT winds and SLTAC geostrophic surface currents is here estimated to be 525 GW (on a 0.25° grid from 80°S-80°N, excluding the equatorial region 5°S-5°N). The different wind products that are compared here, have different spatial resolutions, ranging from 0.25° (QuikSCAT) to 0.7° (ERA-Interim). In order to allow for a meaningful comparison between the products and to eliminate small scale signals a comparison is done for winds on a 0.7°-grid, then the QuikSCAT wind work is slightly higher with 533 GW. The wind work for the forcing products is 590 and 556 GW for ERA-Interim and JRA-55-do, respectively, with very similar spatial distributions (Fig. 2.6 and Tab. 2.1). This estimation shows that on a global mean the wind work with ERA-Interim winds is about 10% larger and about 4% larger for JRA-55-do with respect to the QuikSCAT estimate.

Now we come back to the main objective: the imprints of ocean currents in scatterometer winds and if these are present in forcing data sets. First, we will demonstrate that the ocean current imprints manifest in the wind work on small spatial and temporal scales. We start with the time-dependent wind work, $< \overline{\tau' \cdot u'} >$. The time-dependent wind work gets negative if the ocean current and the wind stress opposing each other. Routinely, when using relative winds to estimate the wind stress the ocean currents induce a negative signal as the following scaling demonstrates: Neglecting the wind in the wind stress calculation for a moment, the zonal component would reduce to $\tau_x = \rho_a C_D| - u_x|(-u_x)$, where τ_x and u_x are the zonal components of the wind stress and ocean current, respectively. This contribution to the wind work is always negative as $\tau_x \cdot u_x \propto -(u_x^2) < 0$. In the following the time-dependent part of the wind work is estimated using absolute winds in order to eliminate the negative current-induced signal and highlight the ocean current imprints that are in the wind. The estimate of the observed time-dependent wind work (based on QuikSCAT wind stress and SLTAC surface currents) reveals pronounced negative contributions in regions with strong currents like the western boundary currents regions and in particular the Agulhas retroflection (Fig. 2.7a). In contrast when the wind stress is estimated

Figure 2.6: Wind work, $\tau \cdot u$ [10^{-3} Wm^{-2}] with SLTAC geostrophic currents and wind stress estimated from (a) QuikSCAT winds, (b) ERA-Interim winds and (c) JRA-55-do winds. All winds have been interpolated on a 0.7 grid to allow for consistent comparison. Globally integrated values are shown within the figure and are estimate from 80°S-80°N excluding the equatorial region 5°S-5°N. The equatorial region (5°N/S) has been masked as the geostrophic approximation is not reliable there. The wind work has been smoothed on 5° after calculation to enhance visual clarity.

with ERA-Interim and JRA-55-do winds basically no negative contributions to the time-dependent component of the wind work are found (Fig. 2.7b,c). The global integrals support this point: the time dependent wind work on the $0.7°$-grid is estimated to be -5 GW, 28 GW and 29 GW for QuikSCAT, ERA-Interim and JRA-55-do, respectively. This let's us deduce two conclusions: (1) QuikSCAT winds contain ocean current imprints and (2) these imprints are small if not negligible in ERA-Interim and JRA-55-do.

Another approach to investigate the current imprints on the wind is to estimate the wind work using spatial high-pass filtered wind stress instead of a temporal filter. The small spatial scale signal of the wind work can be estimated as $\overline{<\tau>_{0.7°}\cdot u}$ - $\overline{<\tau>_{5°}\cdot u}$, where $<\cdot>_{x°}$ denotes spatial low-pass filter of $x°$. In this difference only the signal on spatial scales larger than $0.7°$ and smaller than $5°$ in the wind work remains. The contribution of this small scale wind stress to the total wind work is relatively small. The small scale wind work for QuikSCAT is 14 GW, for ERA-Interim 59 GW, and for JRA-55-do 52 GW (Tab. 2.1). In contrast to the time-dependent component of the wind work, the small scale wind work is found to be mostly positive. The relative difference between the the various wind products is, however, qualitatively consistent for the time-dependent wind work and the small scale wind work: the globally integrated time dependent part of the wind work has been estimated to be smallest for QuikSCAT and the ERA-Interim and JRA-55-do are about 35-45 GW larger.

In summary, both the time-dependent wind work and the small scale wind work demonstrate a qualitatively consistent result: as a consequence of the imprints of ocean currents in QuikSCAT winds the time-dependent and small scale wind work have negative or small contributions to the total wind work. If these quantities are estimated with ERA-Interim and JRA-55-do winds the contributions are much larger. Therefore it can be concluded that these wind products have much smaller imprints on small spatial and temporal scales. This result is rather unexpected in particular for ERA-Interim winds, as in their production process QuikSCAT winds are assimilated.

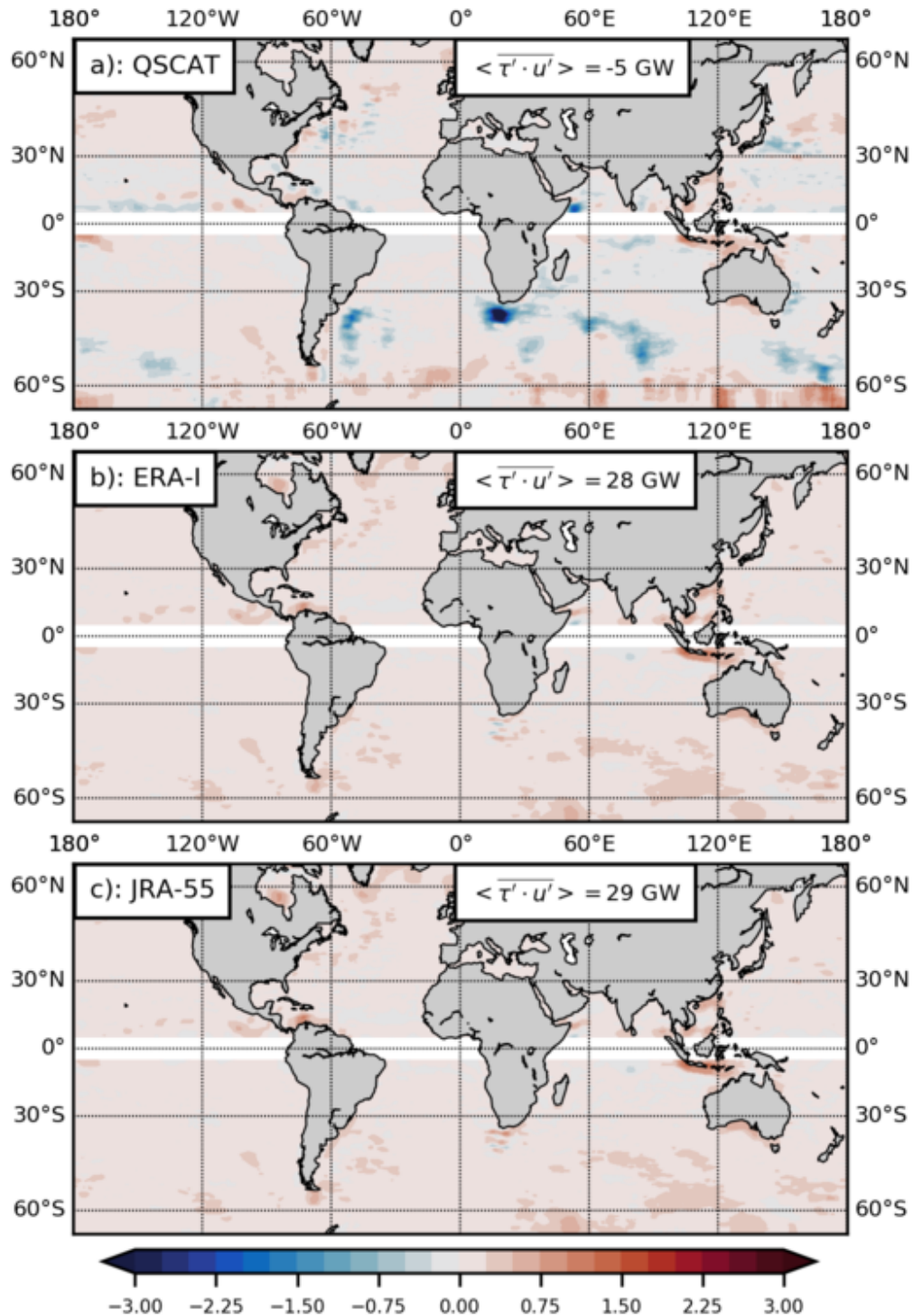**Figure 2.7:** Time dependent Wind work, $\tau' \cdot u'$ [10^{-3} Wm^{-2}] with SLTAC geostrophic currents and wind stress estimated from (a) QuikSCAT winds, (b) ERA-Interim winds and (c) JRA-55-do winds using absolute winds. All winds have been interpolated on a 0.7 grid to allow for better comparison. Globally integrated values are shown within the figure and are estimate from 80°S-80°N excluding the equatorial region 5°S-5°N. The equatorial region (5°N/S) has been masked as the geostrophic approximation is not reliable there. The wind work has been smoothed on 5° after calculation to enhance visual clarity.

	QuikSCAT	ERA-Interim	JRA-55-do
0.25°	525	-	-
0.56°	530	-	557
0.70°	533	590	556
5°	519	531	504
0.70° -5°	14	59	52

Table 2.1: Power inputs estimates, $\overline{\tau \cdot u}$ [Gigawatt; GW] to the geostrophic currents (80°S-80°N, excluding the equatorial region 5°S-5°N) based on wind products from scatterometer measurements (QuikSCAT) and forcing datasets based on daily values from 2000-2009. The wind stress was calculated using Large et al. (1994) bulk formulation. The wind stress has been re-gridded on various grids, see left column before the power input was estimated.

2.6 Summary & Conclusions

A specific aspect of the air-sea momentum flux concerns the use of the relative motion between atmospheric wind and oceanic surface currents which is often referred to as *relative winds*. There is theoretical (Hersbach and Bidlot, 2008; Etling, 2008, and section appendix A) and observational evidence (Kelly et al., 2001; Cornillon and Park, 2001) that relative winds should be used to estimate the momentum flux. Model studies have provided some evidence that the use of relative winds leads to a more realistic representation of the ocean (e.g., Dewar and Flierl, 1987; Renault et al., 2016b, 2017b).

To force an ocean-only model information about the near-surface winds is necessary. While direct measurements are sparse, satellite-mounted scatterometers provide wind measurements that are derived from the stress exerted by the winds and surface currents at the ocean surface. More precisely, these wind measurements describe the relative velocity between atmosphere and ocean. In agreement with previous studies (Hughes and Wilson, 2008; Renault et al., 2017a) the analysis presented here confirmed that ocean currents imprint on QuikSCAT winds. The results of this study show that the wind work estimated with QuikSCAT winds is negatively biased by about 30-40 GW. This has led to the question if forcing products that are corrected by QuikSCAT winds are also negatively biased. Based on the methodology employed in this study no evidence of imprints of ocean currents have been found in the forcing datasets ERA-Interim and JRA-55-do. For JRA-55-do this is already expected as the calibration method uses long-term means which hardly cover the relative wind signal which is associated with small spatial scales and short time scales. On the other hand ERA-Interim directly assimilates scatterometer winds and therefore it was expected to find imprints of ocean currents. The lack of these signals is not clear, but is probably related to the exact assimilation procedure that we are not aware of.

Finally it can be concluded that due to a lack of imprints of surface currents in the ERA-Interim and JRA-55-do wind data, these products could be readily used to force ocean models with relative winds. On the other hand the use of QuikSCAT winds does introduce a negative bias on the wind work, hampering its use in forcing ocean models. These statements are based on the analysis of the imprints of ocean currents on small spatial and temporal scales, leaving the potential implications of large scale imprints to future studies.

Appendix

Appendix A: Momentum flux derivation

Close to the ocean's surface the atmospheric winds generate turbulence. This results into a vertical flux of horizontal momentum and can be expressed as the Reynolds momentum flux (e.g., Etling, 2008):

$$\tau = \overline{\rho}\,\overline{w'u'},\tag{2.3}$$

where $\overline{\rho}$ is mean density and $\cdot'$ denotes the fluctuations of the vertical and zonal velocities w and u, respectively. Since the motions in the surface layer (Prandtl layer) are thought to be always turbulent and the momentum flux is constant with height, we can define a friction velocity u_*:

$$u_* = \sqrt{\frac{\tau}{\rho}} = \sqrt{-\overline{w'u'}}.\tag{2.4}$$

Using the Monin-Obukohov similarity theory the vertical profile of the wind can be described as:

$$\frac{\partial u}{\partial z} = \frac{u_*}{\kappa(z+z_0)}\Phi_M(\frac{z+z_0}{L}),\tag{2.5}$$

where $\kappa \approx 0.41$ is the Kármán constant, z_0 roughness length, L the Obukhov length and Φ_M a profile function. The profile function is defined for neutral, stable and unstable conditions (further details in Etling (2008)). The integration of Eq. 2.5 gives the wind speed at height z:

$$u(z) - u(z=0) = \frac{u_*}{\kappa}ln(\frac{z+z_0}{z_0}) - \Psi_M(\frac{z+z_0}{L}) + \Psi_M(\frac{z_0}{L}),\tag{2.6}$$

where $\Phi_M(x) = 1 - x\Psi'_M(x)$. It is important to mention that typically at the boundary $u(z=0) = 0$ is assumed. However at sea there is generally a surface current u_o present, which means that the boundary condition should be $u(z=0) = u_o$.

Generally at least two wind speeds at different heights are needed to define the logarithmic wind profile and infer the friction velocity u_*. In most cases this is not a practical solution and therefore the empirical drag coefficient C_D was established which relates the friction velocity u_* to the wind speed in 10 meter:

$$\tau = \rho_a u_*^2 = \rho_a C_D u_{rel}^2 = \rho_a C_D |U_a - u_o|(U_o - u_o)\tag{2.7}$$

This is the bulk formulation for momentum, which relates the wind stress τ to the relative motion between atmosphere and ocean u_{rel}. From the fact that (2.6) requires a bottom boundary

condition at $z = 0$ it is evident that the surface motion of the ocean should be used. Therefore the bulk formulation for momentum requires the relative velocity $u_{rel} = U_a - u_o$ between 10m wind speed. The idea of this part follows Hersbach and Bidlot (2008).

Appendix B: Wind vector correction in forcing datasets

The correction procedure used in JRA-55-do is based on the procedure used for the CORE.v2 forcing (Large and Yeager, 2009). The CORE forcing is not used for this study as the relatively coarse resolution of 1.875° does not satisfy the needs of this study. For the CORE forcing the correction of the NCEP vector winds (U_N, V_N) has been done with respect to the QuikSCAT vector winds (U_Q, V_Q). The multiplicative speed factor R_S and the rotation correction δ have been calculated point-wise for all latitude and longitude points ϕ and λ, respectively:

$$R_S(\lambda, \phi) = \langle (U_Q^2 + V_Q^2)^{1/2} \rangle / \langle (U_N^2 + V_N^2)^{1/2} \rangle \tag{2.8a}$$

$$\delta(\lambda, \phi) = f(S_N) \left[tan^{-1} \left(\frac{\langle V_Q \rangle}{\langle U_Q \rangle} \right) - tan^{-1} \left(\frac{\langle V_N \rangle}{\langle U_N \rangle} \right) \right], \tag{2.8b}$$

where $\langle \cdot \rangle$ denotes averages over the 5-year QuikSCAT period (2000-2004) and S_N is the magnitude of the vector average NCEP wind over the same period. Large and Yeager (2009) increased the wind almost everywhere with strong regional differences, but up to 40% in the Southern Ocean and even up to 70% in the Barents Sea (details in their Fig. 2). The rotation correction (positive counter-clockwise) is up to -25° in the North Atlantic and North Pacific and about 10° averaged over the Southern Ocean. In coastal regions the corrections are smaller.

JRA-55-do has some smaller corrections with positive correction factor in the tropics and sub-tropics and decrease in the subtropical and subpolar regions. The higher spatial variability of the winds due to better horizontal resolution might be responsible for the larger spatial variability of the offset factor R_S varying between +1.3 and -1.4 (see their Fig. 7 and 8). The rotation adjustment is quite similar to Large and Yeager (2009), but the corrections are smaller in amplitude.

The ERA-Interim Reanalysis project (Dee et al., 2011) assimilates scatterometers winds directly during production. Thereafter no post-production correction is applied to the winds. We are not aware of the details of assimilation procedure. But the correction for JRA-55-do is thought to have an smaller impact, as the correction is done against a temporal mean and the ERA-Interim correction is thought to happen on a time-step basis.

3 Feedback of mesoscale ocean currents on atmospheric winds in high-resolution coupled models and implications for the forcing of ocean-only models

Including the ocean surface currents in the wind stress calculation can alter the momentum flux from the atmosphere to the ocean. In an ocean-only simulation the mechanical feedback to the atmosphere is included using a simple tweak in the momemtum flux calculation. For the first time we investigated the spatial and temporal variability of this feedback in two global atmosphere-ocean models and were able to demonstrate that the background wind speed and atmospheric stability are the main factors. A tentative implementation of this feedback in an ocean-only models revealed that the tweak improves the mechanical coupling in this model.

Contents

3.1 Introduction

During the last decade, studies of satellite observations and high-resolution coupled ocean-atmosphere models have revealed some intriguing impacts of mesoscale ocean fronts and eddies on the near-surface winds. Spurred by the identification of an imprint on the surface wind of gradients in sea surface temperature (SST) associated with meandering oceanic fronts (Xie, 2004; Chelton et al., 2004), a particular emphasis of research has been on the mechanisms of the thermal air-sea coupling. At mid-latitudes, air-sea interaction at larger scales exhibits a negative correlation between SST anomalies and surface wind, reflecting a passive role of the ocean to the atmospheric forcing (e.g. Mantua et al., 1997; Okumura et al., 2001). The interaction is reversed at smaller spatial scales where SST anomalies exert an influence on wind speeds and wind stress via perturbations of the atmospheric boundary layer (Wallace et al., 1989; Samelson et al., 2006; Spall, 2007; Small et al., 2008), leading to a positive SST - wind stress correlation for quasi-stationary frontal regions (Bryan et al., 2010; Roberts et al., 2016) and transient eddies (Frenger et al., 2013). It is well established that the SST - wind (stress) coupling can have important repercussions for tropospheric weather patterns (Minobe et al., 2008), while in turn, the damping of SST anomalies by enhanced winds constitutes a negative feedback on the oceanic mesoscale (Shuckburgh et al., 2011). Thermal heat fluxes due to mesoscale SST anomalies also have important implications for the energetics of western boundary currents (Ma et al., 2016).

Another aspect of mesoscale air-sea coupling concerns the imprint of surface currents. It has long been recognized that current-induced vertical shear in the horizontal velocities at the ocean's surface can influence frictional air-sea coupling and thus can cause surface motions to decay (Dewar and Flierl, 1987; Pacanowski, 1987). Accounting for the ocean surface current in the wind stress formulation used in ocean circulation models, i.e. the use of 'relative winds' across the interface instead of 'absolute winds' in the bulk parameterization of the turbulent momentum flux, was found to significantly (up to 30%) reduce the energy input to the large-scale circulation (Duhaut and Straub, 2006; Zhai and Greatbatch, 2007; Hughes and Wilson, 2008; Scott and Xu, 2009) and by up to 70% in the near-inertial frequency band (Rath et al., 2013). In eddying models the eddy kinetic energy (EKE) was found to be reduced (Zhai and Greatbatch, 2007; Seo et al., 2016) due to increased surface drag and reduced wind energy transfer (Hutchinson et al., 2010), with implications for primary production (Eden and Dietze, 2009). In a regional model study it was shown that for the wind stress formulation, the effect of mesoscale current anomalies was much more important that the effect of mesoscale SST anomalies (Seo et al., 2016). Regionally the large-scale wind curl is quite important for the wind power input to mesoscale features: When the large-scale wind curl has the same sense of rotation as the eddies it spins up the eddies; if the senses of rotation have opposing signs eddies are spun down (Xu et al., 2016; Byrne et al., 2016). Thermal effects due to mesoscale SST anomalies influence the boundary layer above, which induces changes in the winds and therefore may also alter spin up and spin down effects

(Byrne et al., 2016).

While previous work on the role of surface currents in the air-sea momentum transfer focused on the effect of wind stress changes, recent studies also began to consider their implications for the near-surface winds. Moulin and Wirth (2016) investigated the local exchange of momentum between idealized turbulent layers of the ocean and the atmosphere at the scale of ocean eddies, showing that owing to the large difference in inertia between the two components, the atmosphere can be influenced by persistent ocean features, while its short time fluctuations tend to be independent of the ocean dynamics. Renault et al. (2016c) investigated the influence of mesoscale ocean eddies on the momentum exchange in a regional high-resolution coupled ocean-atmosphere model of the California Current System (CCS). They showed that the current feedback can conceptually be split into two parts: its effect on the wind stress which induces a damping on surface currents, and a concomitant effect on the near-surface winds which partly counteracts the damping and re-energizes the atmosphere (and subsequently the ocean). They found that the near-surface winds are enhanced by about 20% of the surface ocean current. These findings have been confirmed by satellite based observations (Renault et al., 2017a). Based on their findings for the CCS, Renault et al. (2016c) suggest that for uncoupled ocean-only models, the partial re-energization should be taken into account in the bulk formula for the wind stress.

The present study extends the approach of Renault et al. (2016c) by examining the air-sea momentum transfer at the oceanic mesoscale in two versions of a global atmosphere-ocean model with 'eddy-permitting' and 'eddy-resolving' ocean components. More specifically, using the coupled simulations, our objectives are (1) to identify the imprint, including its spatial distribution, of mesoscale ocean current features on the near-surface winds over the global ocean by inspecting spatially high-pass filtered surface currents and near-surface winds; (2) to investigate its repercussion for the surface momentum flux, i.e., the effect of the current - wind feedback on the current - wind stress relation. Using an ocean-only model set-up, we also investigate a tentative implementation of the diagnosed spatially-variable, monthly-mean distribution of the current-wind coupling in the bulk wind stress formulation and show that this approach is surprisingly good at reproducing the mechanical coupling seen in the fully coupled models.

3.2 Methods & Models

3.2.1 Methods

Both atmospheric surface winds and ocean-surface currents determine the wind stress

$$\vec{\tau} = \rho_a C_D |\vec{U} - \alpha \vec{u}| (\vec{U} - \alpha \vec{u}), \tag{3.1}$$

where ρ_a is air density, C_D the drag coefficient, $\vec{U}$ the 10m wind , $\vec{u}$ the ocean surface current and α a parameter representing the influence of ocean currents. Since C_D is also function of the relative velocity $\vec{U} - \alpha\vec{u}$ and the surface stability, it also depends on the choice of α. Since the wind speed is typically an order of magnitude larger than the ocean current speed, it is a challenge to detect the imprint of ocean currents on the wind stress. Fortunately the inherent spatial and temporal scales of the atmosphere and the ocean are very different. While at mid-latitudes atmospheric mesoscale variability is typically associated with time scales of hours to days and spatial scales of hundreds to thousands of kilometers, the oceanic variability is most energetic at time scales of days to weeks with spatial scales of tens of kilometers.

For assessing the imprint of the oceanic variability, we use monthly-mean model output from coupled atmosphere-ocean and forced ocean-only simulations and apply a spatial Hann-type high-pass filter to remove variability on scales longer than approximately 150km (see Appendix A for discussion of this choice and associated sensitivities). Model output closer than 150km to the coast is not used as orographic and coastline effects may also introduce small-scale distortions to the wind field (Perlin et al., 2007; Renault et al., 2016a).

The smallest spatial scales present in the data are emphasized further by considering the curl of the wind, of the wind stress, and of the ocean surface currents in the quantification of the current-wind and current-stress linkages. Here we assume a linear relationship in the form

$$curl(\vec{U}) \quad = s_w \; curl(\vec{u}) \tag{3.2}$$

$$curl(\vec{\tau}) \; 10^2 \quad = s_{st} \; curl(\vec{u}), \tag{3.3}$$

where the coupling coefficients s_w and s_{st} are estimated by linearly regressing the curl of the near-surface wind and the curl of the stress, respectively, against the vorticity of the ocean currents. We note that other studies used bin averaging for the same quantities (Renault et al., 2016c), and for the relationship between the SST gradient and the wind curl or wind gradient (Chelton et al., 2007); however, a bin averaging was found not to be necessary here. Note also that the factor 10^2 is simply used to ensure that the coupling coefficients are O(1).

As a means to account for the partial re-energization of the near-surface winds in the atmo-spheric forcing of uncoupled ocean models, Renault et al. (2016c) proposed to tweak the bulk formulation of the surface momentum flux by using Eq. 3.1 with $\alpha = 1 - s_w$. From their regional model results Renault et al. (2016c) estimated an $s_w = 0.23 \pm 0.01$ for the CCS. We extend this approach here by estimating the spatial distribution of the coupling coefficient s_w from two global coupled simulations.

3.2.2 Models

The analysis related to our objectives (1) and (2) uses output from the eddying atmosphere-ocean model experiments GC2-N512 (hereafter C1/4) and GC2.1-N512O12 (hereafter C1/12), that employ the atmospheric Met Office Unified Model at N512 resolution ($\sim$ 25km) and ocean components based on Nucleus for European Modelling of the Ocean (NEMO; Madec, 2011) ORCA025 and ORCA12, with a nominal resolution of $1/4°$ and $1/12°$, respectively. Turbulent surface fluxes are calculated using a bulk formulation (Smith, 1988) with Charnock's coefficient of 0.018, using relative winds ($\alpha = 1$) and coupling frequencies of 3-hourly for C1/4 and 1-hourly for C1/12. The atmospheric model has 85 vertical levels (Appendix D). Unresolved turbulent motions are parametrized to achieve realistic vertical structures in temperature and wind profiles (Walters et al., 2017). For an extensive documentation of the model configurations and a discussion of the impacts of a resolved ocean mesocale in the simulations we refer to Hewitt et al. (2016). A discussion of the impact of the oceanic mesoscale on the thermal air-sea interaction, i.e. the SST - wind stress relationship, has been given by Roberts et al. (2016). Here we consider the interaction due to momentum transfer at the oceanic mesoscale. The models were integrated for 19 years (year 20 experienced some data loss) and the last 15 years are used for the analysis. Even if 20 year runs might be too short for the deep ocean to spin up, they are sufficient for the surface coupling investigated in this study.

We also discuss some potential impacts of the current-wind coupling using a standard eddy-permitting ocean-only model (ORCA025). The model is based on NEMO (version 3.4) and uses a tripolar grid at a nominal resolution of $1/4°$, and 46 vertical levels with a resolution of 6m near the surface and 250m at depth. The surface-forcing fields build on the interannually varying Coordinated Ocean-Ice Reference Experiments (COREv2, Large and Yeager, 2009; Griffies et al., 2009) and have a temporal resolution of 6 hours and a spatial resolution of $2°$ that is interpolated on the model grid. Turbulent air-sea fluxes are calculated using the bulk formulae given by Large and Yeager (2004). The simulations were started from a 30-yr spinup (1980-2009), which was initialized with the World Ocean Atlas 1998 (Antonov et al., 1998; Boyer et al., 1998) and carried out using forcing for the period 1989-2004. Four ocean-only experiments were performed: with absolute winds ($F_{\alpha=0}$), relative winds ($F_{\alpha=1}$), and two experiments that use spatially and temporally variable α given by the distribution of the coupled experiments C1/4 ($F_{\alpha=C1/4}$) and C1/12 ($F_{\alpha=C1/12}$). The analysis uses the last 15 years of each integration.

3.3 Results

3.3.1 Ocean current feedback on near-surface winds

Generally the momentum exchange between the atmosphere and the ocean is from the atmosphere to the ocean. Here we show that on small spatial scales the ocean surface currents can excite anomalous near-surface winds. In particular, in coupled models, the wind stress also acts as the bottom boundary condition for the atmosphere and thus has an impact on the near-surface winds. This gives rise to a relation between the curl of the ocean currents and the curl of the wind over energetic oceanic regions such as the Gulf Stream Extension (Fig. 3.1a,b) in coupled simulations, reflecting an influence of intense mesoscale ocean currents on the near-surface wind. The slope of the linear regression of both quantities gives the coupling coefficient for the wind (s_w). Both coupled experiments, C1/4 ($s_w = 0.48 \pm 0.05$) and C1/12 ($s_w = 0.47 \pm 0.03$), yield similar estimates for the coupling coefficient, here shown for the month of June. In the uncoupled, ocean-only model driven by the JRA-55 dataset, no such relation is found (Fig. 3.1c) despite the presence of small spatial scales in the wind field used for the forcing. It follows that on small spatial scales in the coupled models, the surface currents influence the surface wind and not the other way round.
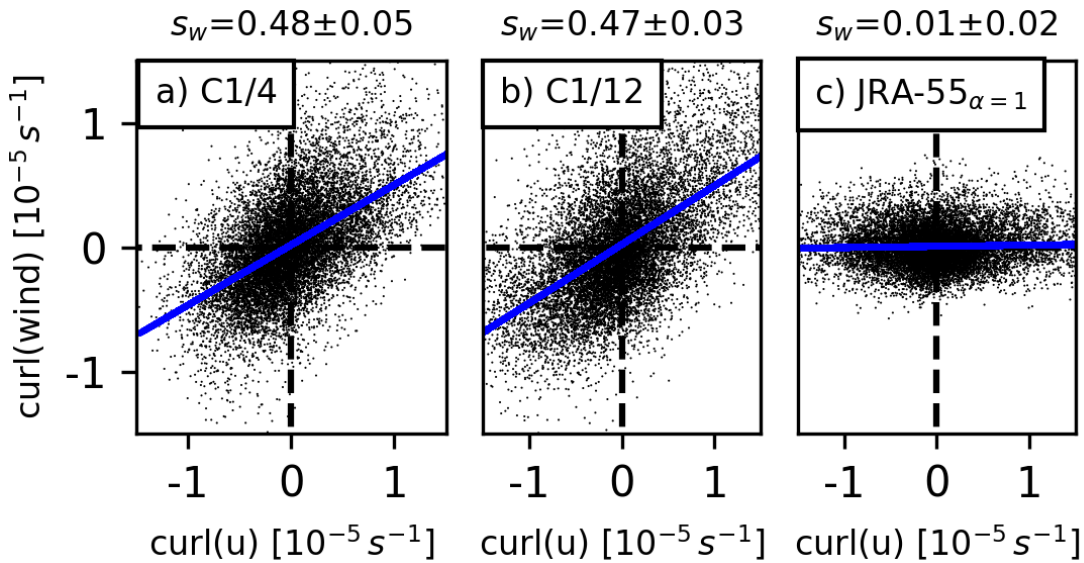
Figure 3.1: Relation between curl(u) and curl(wind) at 10m with linear regression (blue) over the Gulf Stream (GS) Extension (35-45°N, 62-72°W) for the coupled models (a) C1/4 and (b) C1/12, and (c) for the ocean-only model driven by the JRA-55 forcing dataset, all for June. Finding no relation between the small scale ocean surface currents and the near-surface winds in the ocean-only simulation (c) demonstrates that the atmosphere is not the driver in the coupled simulations. The slope of the linear regression (s_w) is shown at the top. The standard error of the slope is calculated employing a binomial method (see Appendix C).

The influence of ocean surface currents on near-surface winds does show a strong spatial variability. Therefore s_w is estimated in 2°x2° boxes over the global ocean. The largest mean values of s_w (up to 0.5) are found over the Western Boundary Current Extension (WBCE) regions and
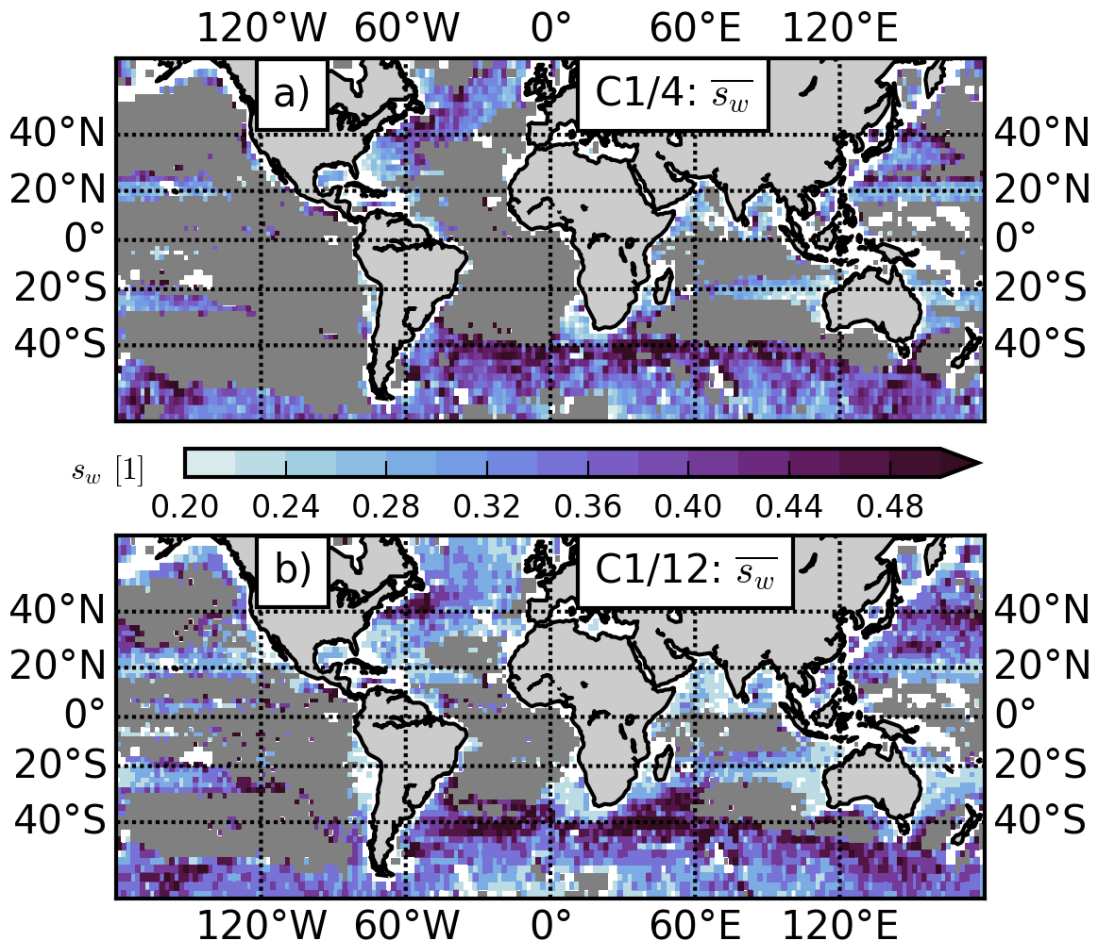
Figure 3.2: Mean of s_w monthly values for (a) C1/4 and (c) C1/12. Note that the last 15 years of the simulations are used for the analysis. Grey shading denotes areas where the curl of the ocean currents is too small so that the estimates of s_w are biased to too large values (see Fig. A2).

the ACC, while in less energetic regions the s_w values tend to be smaller (Fig. 3.2; note that in weakly-energetic regions like the subtropics the method fails to diagnose a robust relationship, for more details we refer to Appendix B). Both coupled experiments C1/4 and C1/12 show a similar pattern.

It is fair to assume that the impact of the ocean surface currents on the near-surface wind depends on the state of the atmospheric boundary layer. Accordingly, the coupling coefficient s_w shows a strong seasonal cycle in both coupled experiments, with larger values in summer than in winter (Fig. 3.3a): e.g., the values are up to 0.5 in summer and values of 0.2 in winter over the Gulf Stream Extension. The general behaviour is similar in both coupled experiments, with some quantitative differences in the amplitudes of s_w. Over the ACC (Fig. 3.3b) almost no seasonal cycle is found with $s_w \approx 0.35$ (C1/4) and $s_w \approx 0.31$ (C1/12).

The seasonality in the coupling coefficient and the different behaviour between GS and ACC regimes can be rationalized in terms of the stability of the near-surface atmosphere, as given by
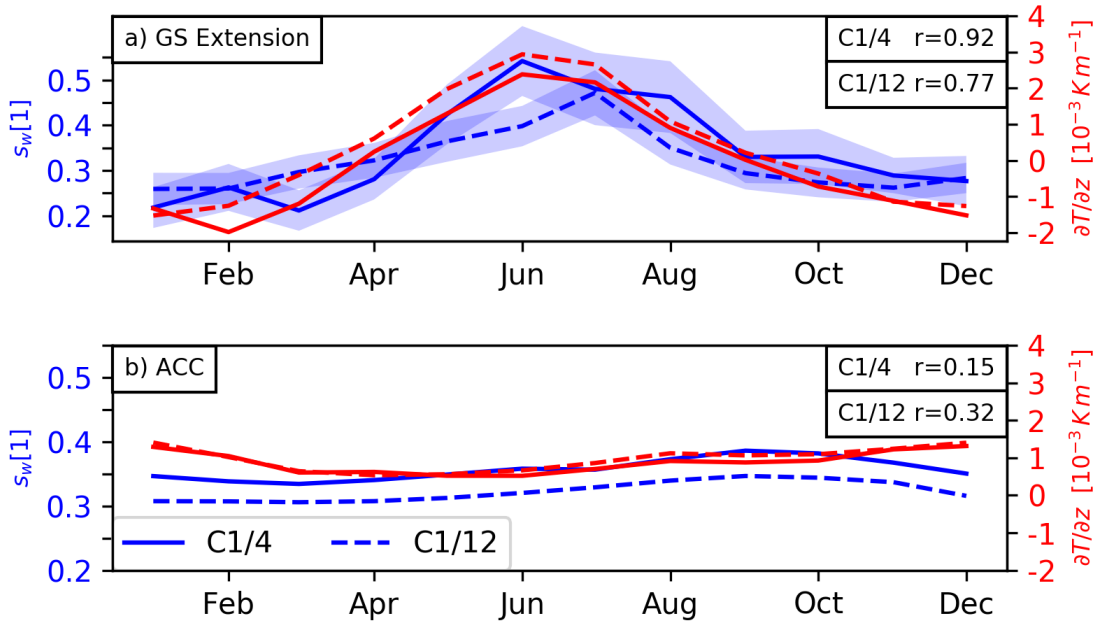
Figure 3.3: Seasonal cycle of coupling coefficient s_w (blue) and vertical temperature gradient between the first two model levels (red) T(53m) minus T(20m) for (a) GS Extension and (b) the ACC (80-40°S); C1/4 (solid) C1/12 (dashed). Correlation coefficients (r) between the coupling coefficient s_w and the vertical temperature gradient are shown at the upper right for the different experiments and regions. Blue shading denotes the standard error of the slope and is calculated employing a binomial method (see Appendix C). For b) the error is of equivalent magnitude, but not shown for visibility reasons.

the vertical temperature gradient between the first two levels of the atmospheric model, 20m and 53m, (Fig. 3.3 red curves). The relationship between the atmospheric stability and the coupling coefficient s_w suggests that the influence of the ocean surface currents is spread over a deeper atmospheric layer when its stability is weak. More specifically, for the GS Extension region (35-45°N, 62-72°W), cold winds from the continent during winter lead to strong turbulent heat fluxes over the Gulf Stream that destabilize the near-surface atmosphere, reflected by a negative vertical temperature gradient. This implies that influence of the ocean currents on the near-surface wind in winter happens over a deeper layer than during summer when the near-surface atmosphere is stable (positive vertical temperature gradient). Accordingly the change in the near-surface wind is smaller in winter as the gain of momentum is distributed over a deeper layer, resulting in a smaller s_w than in summer. During summer months the near-surface layers are relatively shallow which leads to stronger changes in near-surface winds due the presence of ocean currents, i.e. larger s_w. While the amplitude of the seasonality is similar in the north-western Pacific (Kuroshio regime), it is much smaller in the ACC regime where the monthly mean vertical temperature gradients are always positive, resulting in a large mean s_w and very little seasonal variability (Fig. 3.4). The lack of a seasonality in the near-surface stability of the atmosphere also results in low correlation between the stability and s_w.

The strength of the seasonal cycle of s_w does vary with region. An illustration of the spatial
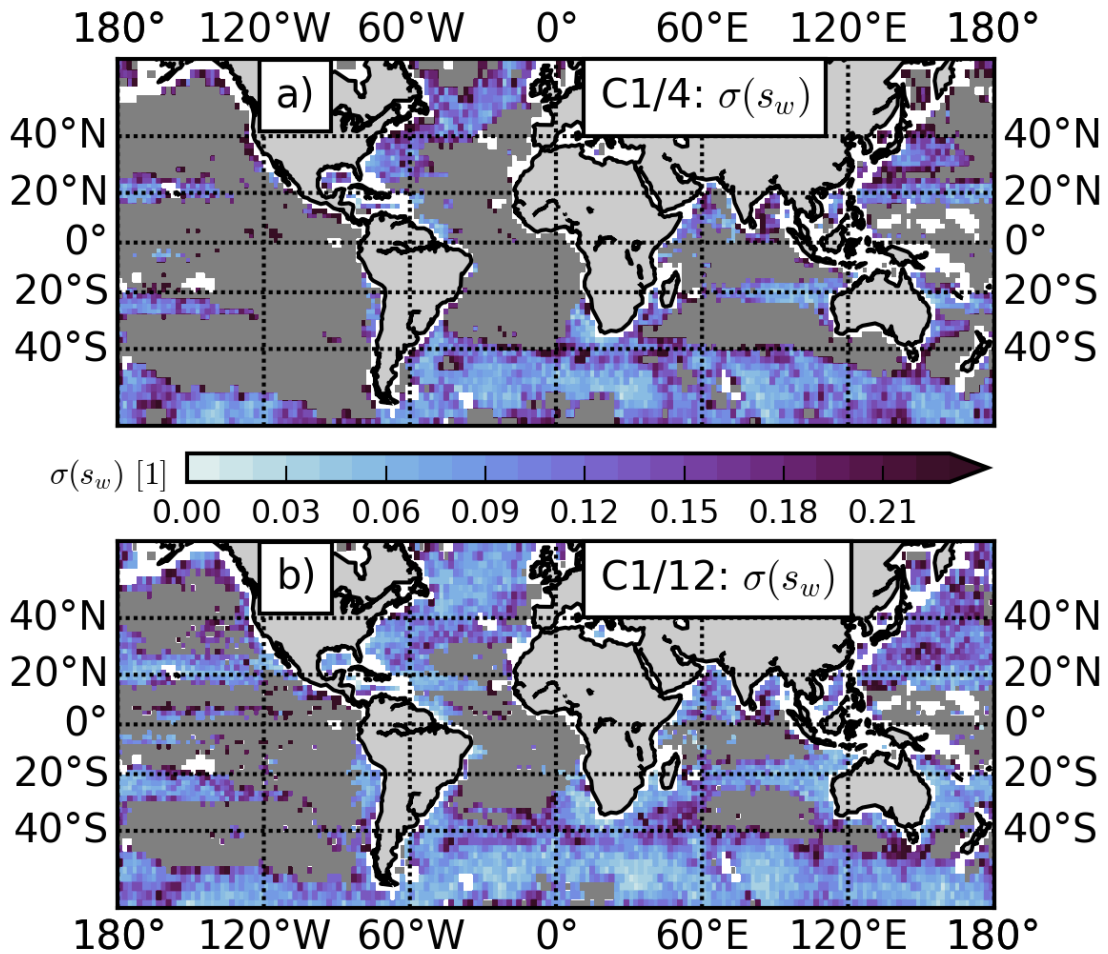
Figure 3.4: Standard deviation of s_w monthly values for (a) C1/4 and (c) C1/12. Grey areas defined as in Fig. 3.2.

distribution of the amplitude is given in Fig. 3.4, which shows the temporal standard deviation of the monthly-mean values of s_w. The main pattern is the contrast between the strong seasonality of the northern hemisphere WBCs and weak seasonality of the core of the ACC reflecting the different seasonality in the stability of the near-surface atmosphere. This is emphasized in Fig. 3.5, showing the correlation between the variability of s_w and near surface stability ($\partial T/\partial z$).

The stability of the near-surface atmosphere tends to determine the strength of the coupling coefficient s_w. Over the WBCE regions the variability of the near-surface stability is high and with that the variability of the coupling coefficient s_w is also high. Positive correlations in Fig. 3.5 illustrate that relation. For the WBCE of the Gulf Stream, the Kuroshio, the Malvinas, as well as for the CCS and the tropical and the subtropical oceans (i.e., for those parts not greyed out), the correlations are positive indicating a relation between the near-surface stability and the coupling parameter s_w. For most of the Southern Ocean positive correlations are found. However, in some regions the correlations found are not significant at a 90% level which might be due to other processes that superimpose the relation between the near-surface stability and the coupling
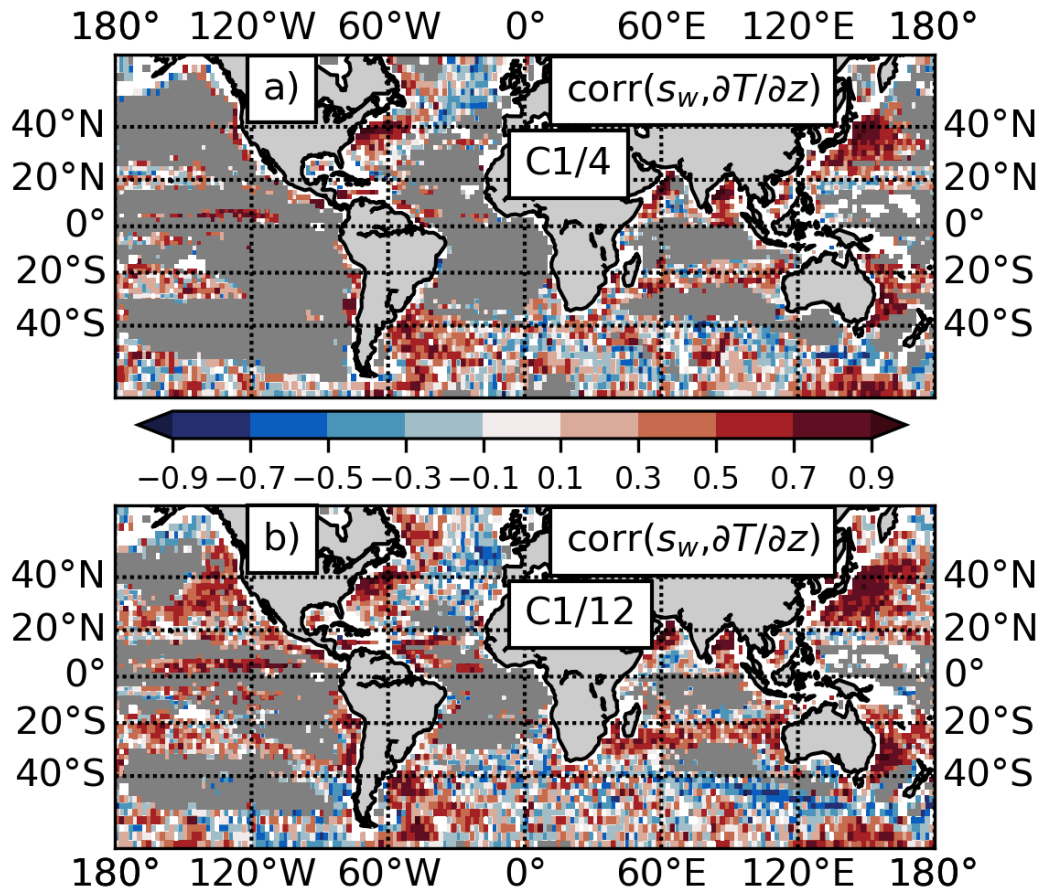
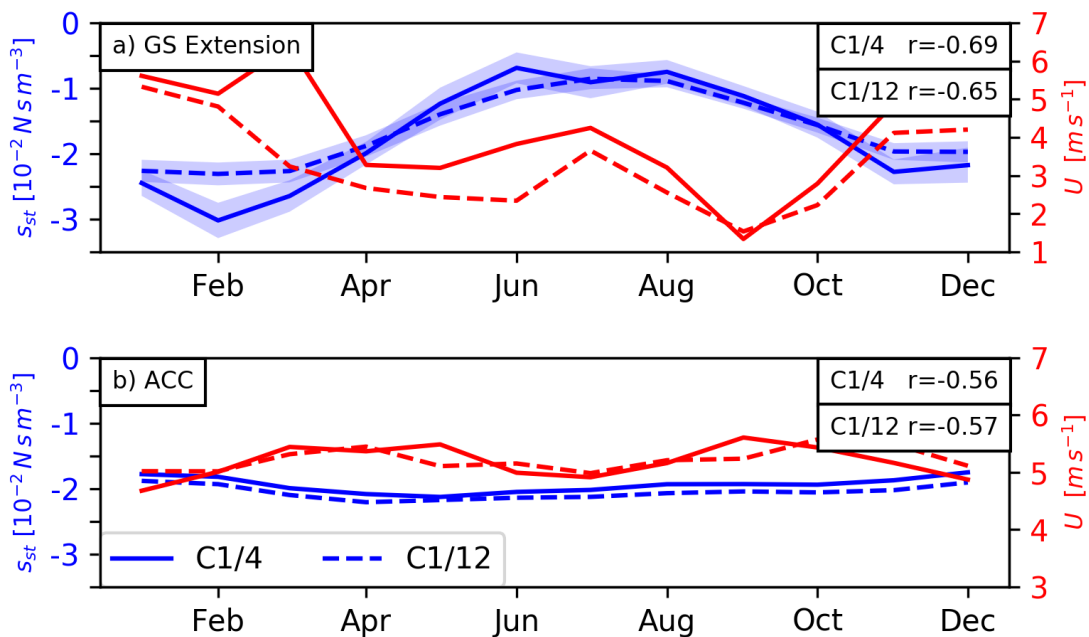**Figure 3.5:** Correlation between the coupling coefficient s_w and near surface stability between the first two model levels ($\partial T/\partial z$) for (a) C1/4 and (b) C1/12. Positive correlations reflect that in unstable conditions low s_w values are found and in stable conditions high s_w values are found. Only p values smaller than 0.1 are considered. Grey areas defined as in Fig. 3.2.

coefficient s_w.

### 3.3.2 Imprint of ocean surface currents on the wind stress

The presence of ocean surface currents is accounted for in the wind stress formulation (Eq. 3.1). The strength of the coupling can be expressed by the coupling coefficient s_{st} which is estimated by the slope of the linear regression between the curl of the ocean surface currents and the curl of the wind stress. The more negative s_{st} the stronger the coupling and the stronger the damping of surface currents, as the exited stress acts against the surface currents. In the Gulf Stream Extension region we find large values of s_{st} up to -3 in winter and smaller values as low as -1 in the summer consistently in both coupled simulations, indicating stronger damping in summer than in winter (Fig. 3.6). The coupling strength is largely determined by the background wind directly, but also through the drag coefficient C_D which is to leading order a function of the background wind. We find that the background wind has a maximum in winter and a minimum in summer and is negatively correlated with s_{st} ($r \approx -0.6$) based on monthly means. Over the ACC the background winds are stronger but the temporal variability is less pronounced which results in stronger coupling coefficients s_{st} with less temporal variability and correlation coefficients of similar magnitude compared to the Gulf Stream Extension.

Figure 3.6: Seasonal cycle of coupling coefficient s_{st} (blue) and monthly mean background wind speed U (red) for (a) GS Extension and (b) the ACC (80-40°S); C1/4 (solid) C1/12 (dashed). Correlation coefficients (r) between the coupling coefficient s_w and the background wind speed U are shown at the upper right for the different experiments and regions. Blue shading denotes the standard error of the slope and is calculated employing a binomial method (see Appendix C). For b) the error is of equivalent magnitude, but not shown for visibility reasons.

In a global perspective the coupling coefficient s_{st} has a strong spatial variability consistently found in both coupled simulations (Fig. 3.7). Large mean s_{st} values up to -3 are found over

the Gulf Stream Extension region, the Kuroshio Extension region and the ACC in particular in the Atlantic and Indian Ocean sectors. These areas are commonly associated with strong winds. Regions with small s_{st} are mostly equatorward from 40°N and S and have typically much smaller background winds than in the westerly wind regions. The patterns of C1/4 and C1/12 are surprisingly similar indicating only a minor influence from the horizontal resolution.
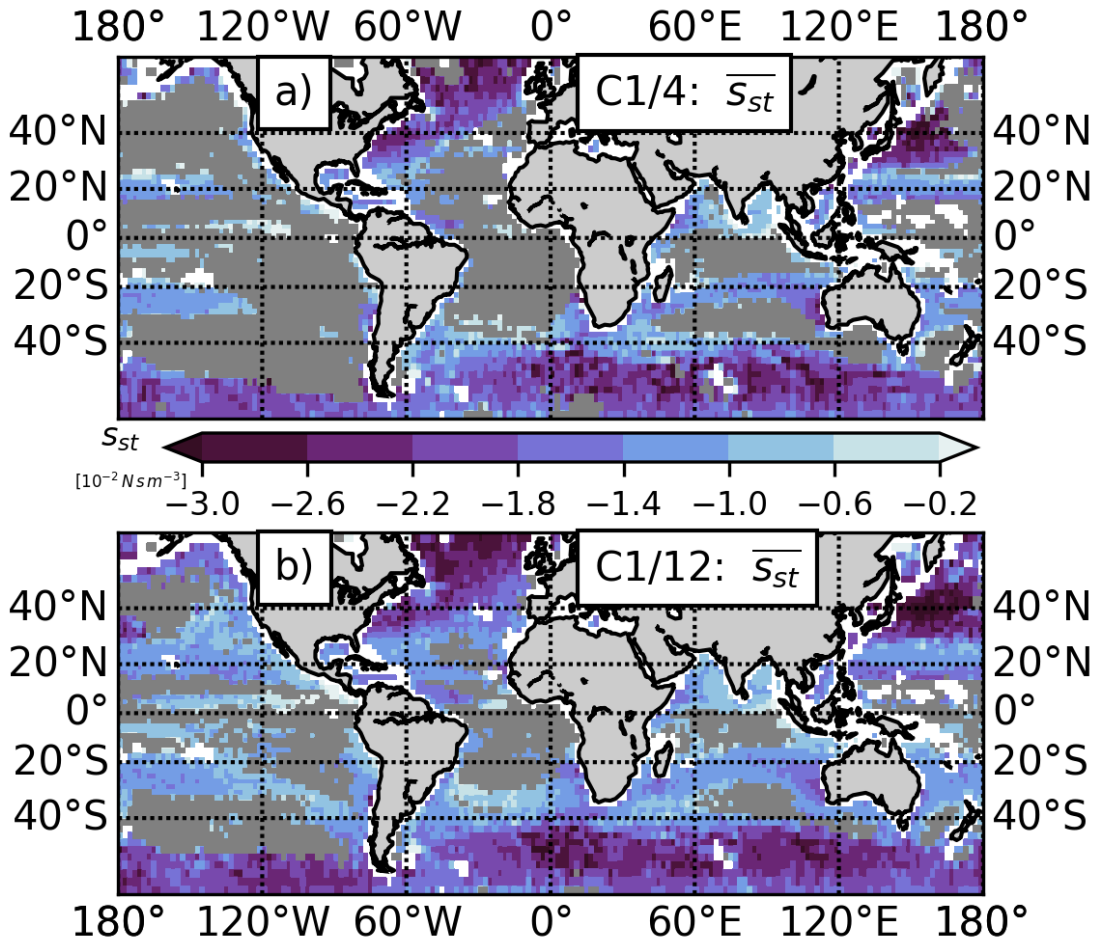
Figure 3.7: Mean of s_{st} DJF monthly values for (a) C1/4 and (c) C1/12. Grey areas defined as in Fig. 3.2.

The relation between the coupling coefficient s_{st} and the background wind holds in most regions as indicated by negative correlations (based on monthly means; Fig. 3.8) in particular over the Gulf Stream and Kuroshio Extension, large areas in the Southern Ocean, the Indian Ocean and other subtropical regions. However, in some regions the correlations found are not significant at a 90% level which might be due to other processes that superimpose on the relation between background wind speed and the coupling coefficient s_{st}.

We use s_{st} as a measure of the fidelity of the momentum flux representation and illustrate the coupling coefficients for C1/4, C1/12, $F_{\alpha=0}$, and $F_{\alpha=1}$ for the Gulf Stream Extension in the month of January in Fig. 3.9. In comparison to the s_{st}-values for the coupled models (-2.23 ± 0.05
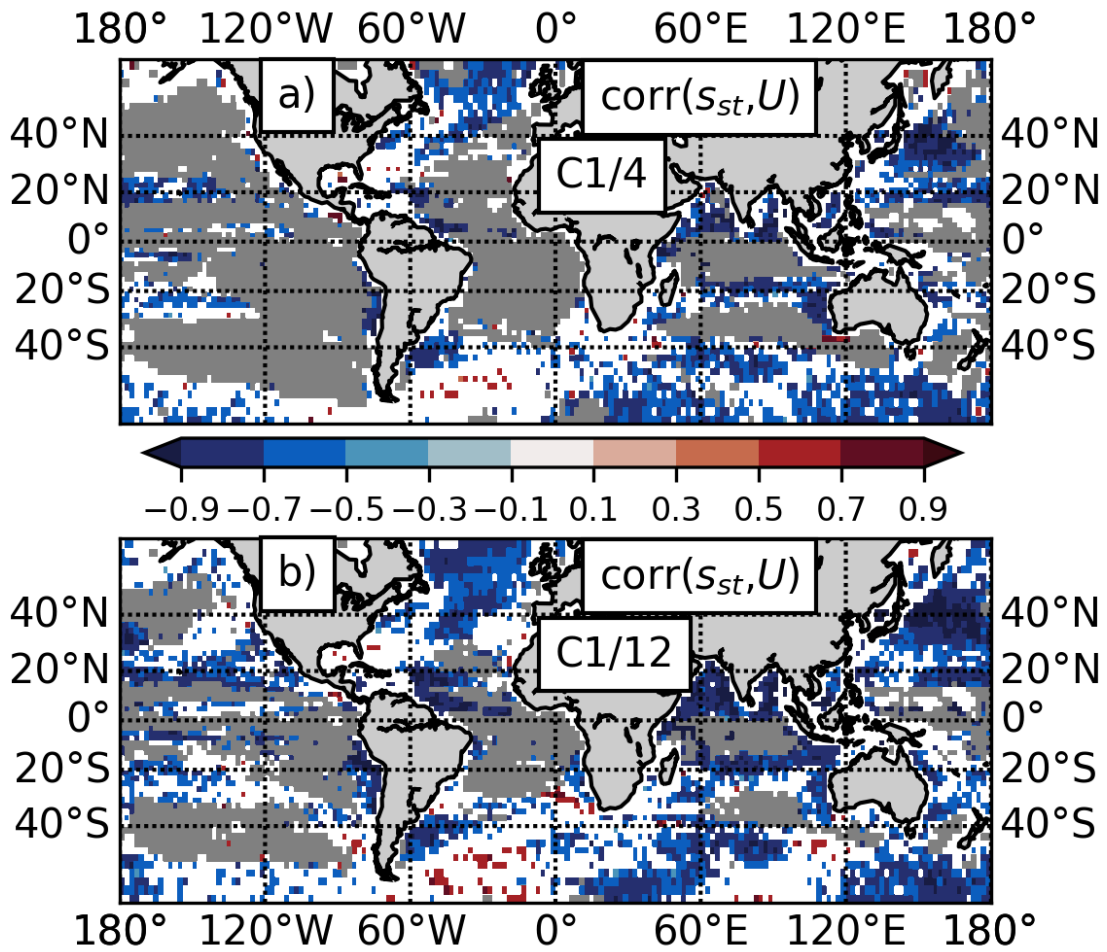
Figure 3.8: Correlation between the coupling coefficient s_{st} and background wind speed U for (a) C1/4 and (b) C1/12. Negative correlations reflect that under strong wind conditions large negative s_{st} values are found and that for low wind conditions small s_{st} values are found. Only p values smaller than 0.1 are considered. Grey areas defined as in Fig. 3.2.

for C1/4 and -2.26 ± 0.05 for C1/12), the coefficient in the relative wind simulation ($F_{\alpha=1}$) indicates a much too strong effect ($s_{st} = -3.28 \pm 0.03$), whereas there is no coupling in the absolute wind simulation ($F_{\alpha=0}$, $s_{st} = 0.04 \pm 0.03$).

This discrepancy in the coupling coefficient s_{st} between the ocean-only and coupled simulations is not due to different background winds, but due to the lack of feedback from the ocean currents to the surface wind in the ocean-only experiments. In the coupled model simulations, this feedback amounts to a re-energization of the atmospheric winds by the ocean currents. As we showed in the previous section this re-energization is present in the coupled simulations and excites a curl in the wind that has the same sense of rotation as the curl of the ocean current. This re-energization leads to more positive coupling coefficients s_{st} in the coupled simulations than the ocean-only simulations $F_{\alpha=1}$ and $F_{\alpha=0}$.
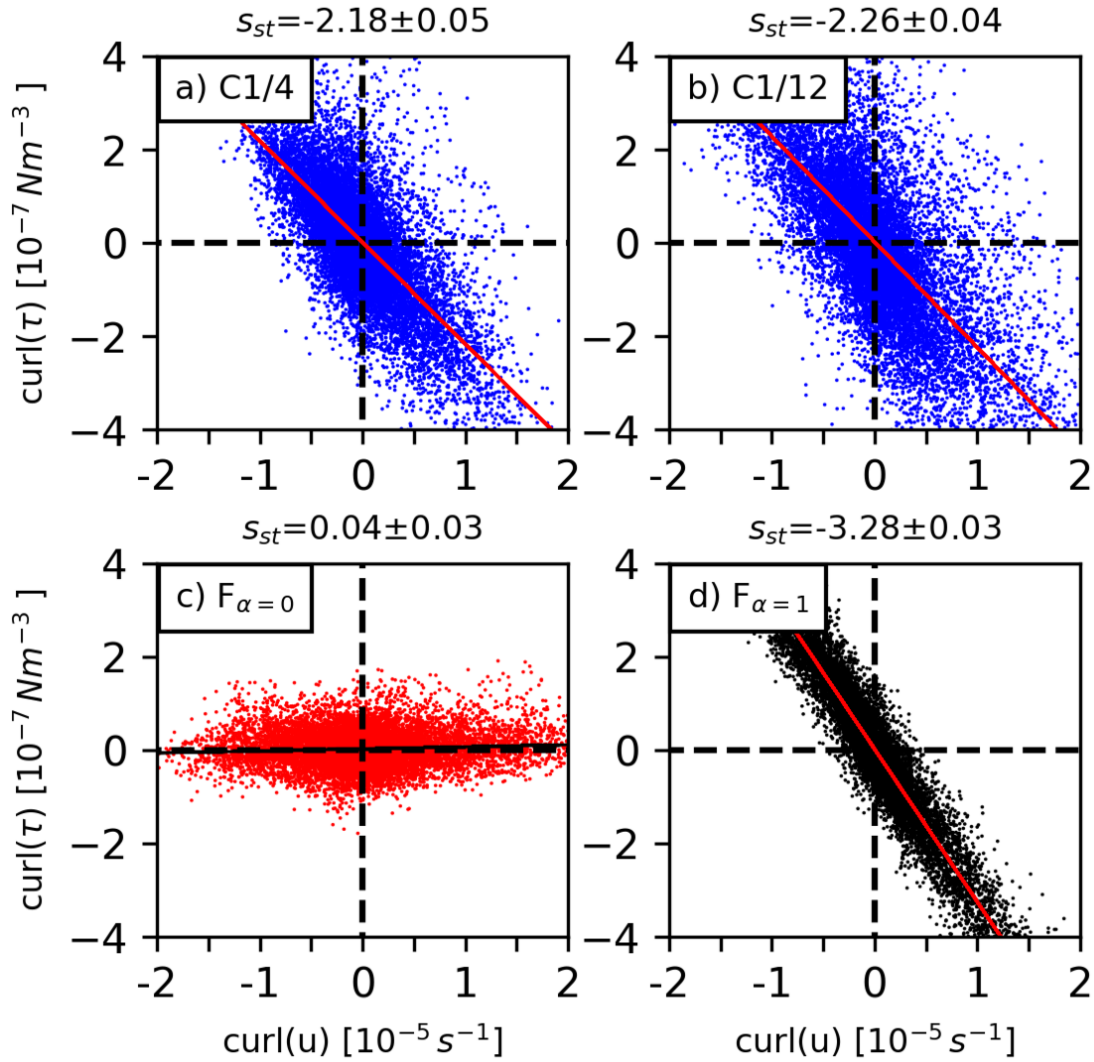
Figure 3.9: Ocean-surface current and wind stress coupling coefficient s_{st} for (a) C1/4 (blue), (b) C1/12 (blue), (c) $F_{\alpha=0}$ (red), and (d) $F_{\alpha=1}$ (black), over the Gulf Stream Extension (35-45°N, 62-72°W) for January. Linear regressions are depicted by solid lines; slopes and errors of the slopes are shown in the titles.

3.3.3 Preliminary assessment of the re-energization effect tentatively implemented in uncoupled models

In the previous sections we showed that in coupled atmosphere-ocean models, the near-surface winds get re-energized by the surface currents. In uncoupled ocean models such a mechanism is missing due to the fact that the atmospheric state is specified. The direct consequence of this deficiency are too negative coupling coefficients s_{st} in ocean-only models in the 'relative wind' configuration. As a correction Renault et al. (2016c) suggest to modify the velocity used in the bulk formulation (Eq. 3.1) by $U + s_w \cdot u - u$, so that the wind U is re-energized by $s_w \cdot u$, where u is the ocean current velocity. We then use $\alpha = 1 - s_w$ in Eq. 3.1 to force ocean-only models. As a test of its potential use in forced ocean-only models, following the suggestion of Renault et al. (2016c), a monthly-varying climatology of s_w is calculated from C1/4 and C1/12 with 2°×2° resolution, and used in Eq. 3.1 with $\alpha = 1 - s_w$. For the areas with grey shading in Fig. 3.2 the
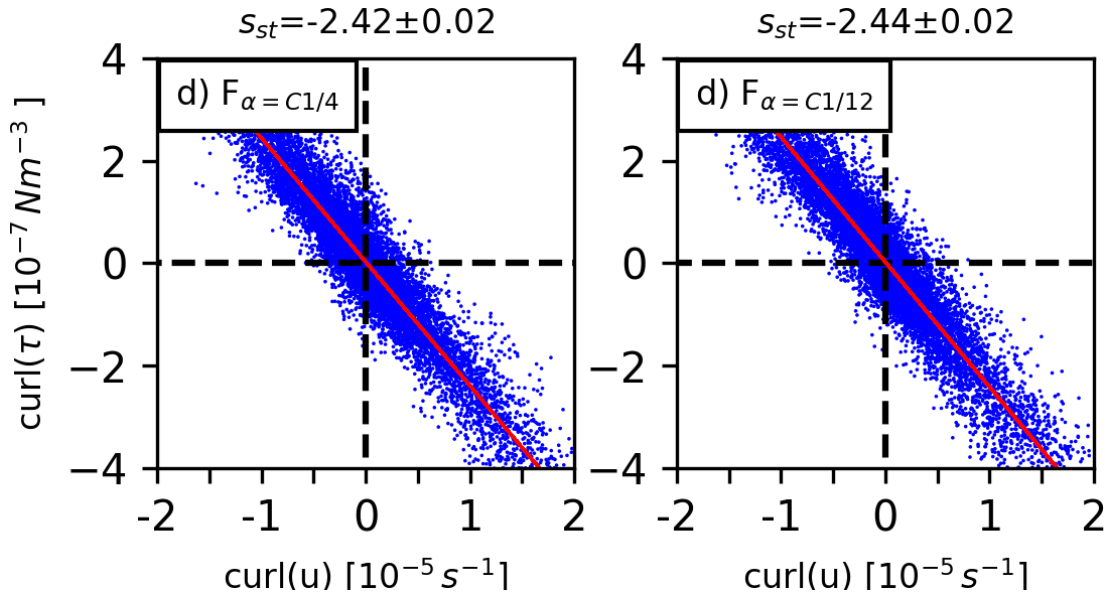
Figure 3.10: Ocean-surface current and wind stress coupling coefficient s_{st} for (a) $F_{\alpha=C1/4}$, (b) $F_{\alpha=C1/12}$ over the Gulf Stream Extension (35-45°N, 62-72°W) for January. Linear regressions are depicted by solid lines; slopes and errors of the slopes are shown in the titles.

global mean values of $\alpha = 0.65$ (C1/4) and $\alpha = 0.69$ (C1/12) are applied. The bulk forcing with this α ($F_{\alpha=C1/4}$, $F_{\alpha=C1/12}$) is used as part of a series of ocean-only experiments. When modifying the bulk formulation by using the global distribution of α-values obtained above, the forced ocean-only experiments are able to produce coupling coefficients ($F_{\alpha=C1/4}$: $s_{st} = -2.42 \pm 0.03$ and $F_{\alpha=C1/12}$: $s_{st} = -2.44 \pm 0.03$) that are close to the estimates of the coupled experiments in the Gulf Stream Extension region (Fig. 3.10). This implies that the wind stress (or 'top drag') experienced by mesoscale ocean features is of comparable strength in C1/4, C1/12, $F_{\alpha=C1/4}$, $F_{\alpha=C1/12}$, demonstrating that ocean-only simulations with the partial re-energization tweak proposed by Renault et al. (2016c) produce comparable coupling coefficients as the fully coupled simulations, at least in the Gulf Stream Extension region. Differences in the near-surface atmospheric state like the background wind speed and bulk algorithms are likely to account for differences between the coupled and ocean-only simulations (Brodeau et al., 2017), but seem to be of minor importance.

The spatial distribution of the coupling coefficients s_{st} obtained in the ocean-only experiments $F_{\alpha=C1/4}$ and $F_{\alpha=C1/12}$ reproduce the patterns of the coupled experiments with minor differences as shown for December to February (DJF) means (Fig. 3.11). We note larger s_{st} values in the ACC region by up to 0.9 and over the Kuroshio region in the coupled simulations. It is not clear why there is such a difference. As the relation between background winds and s_{st} is not significant in large regions in the Southern Ocean it might be possible that in the coupled simulation other processes are also important for the wind stress calculation that are not captured in the ocean-only simulations. Another possibility might be arising from differences in the bulk formulations
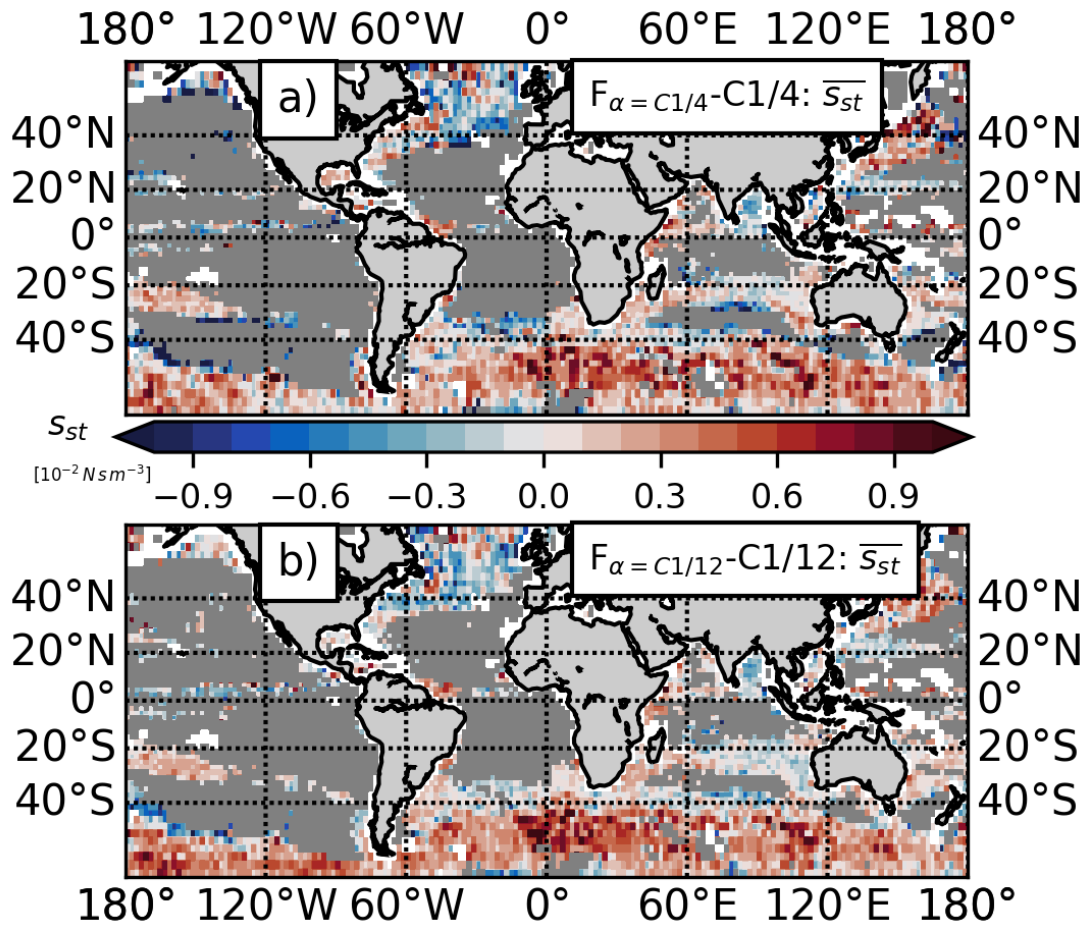
Figure 3.11: Mean of s_{st} differences of DJF monthly values for (a) $F_{\alpha=C1/4}$-C1/4 and (c) $F_{\alpha=C1/12}$-C1/12. Positive values means that the coupled simulations have stronger (more negative) s_{st} values. Grey areas defined as in Fig. 3.2.

(Brodeau et al., 2017).

A more quantitative comparison of the different experiments is given in Fig. 3.12, showing histograms of s_{st}. Both the absolute and relative winds experiments do not compare well with the coupled experiments with global mean values of $s_{st} = -0.02$ ($F_{\alpha=0}$) and $s_{st} = -2.30$ ($F_{\alpha=1}$). Better results are given by the experiments where we estimated the α-values from the coupled experiments. While the global mean of s_{st} in $F_{\alpha=C1/4}$ (-1.53) are very close to the global mean of C1/4 (-1.51), for $F_{\alpha=C1/12}$ (-1.61) there is a slightly larger difference compared to C1/12 (-1.51). The distributions however show small differences: for s_{st} values between -2.25 and -1.5 the ocean-only experiments have higher probability density estimate when compared to the coupled experiments. It is likely that the differences in background winds are contributing to the differences in the distributions (not shown).

This first assessment of the idea by Renault et al. (2016c) to modify the momentum flux formulation for forced ocean-only models to account for the re-energization found in the coupled
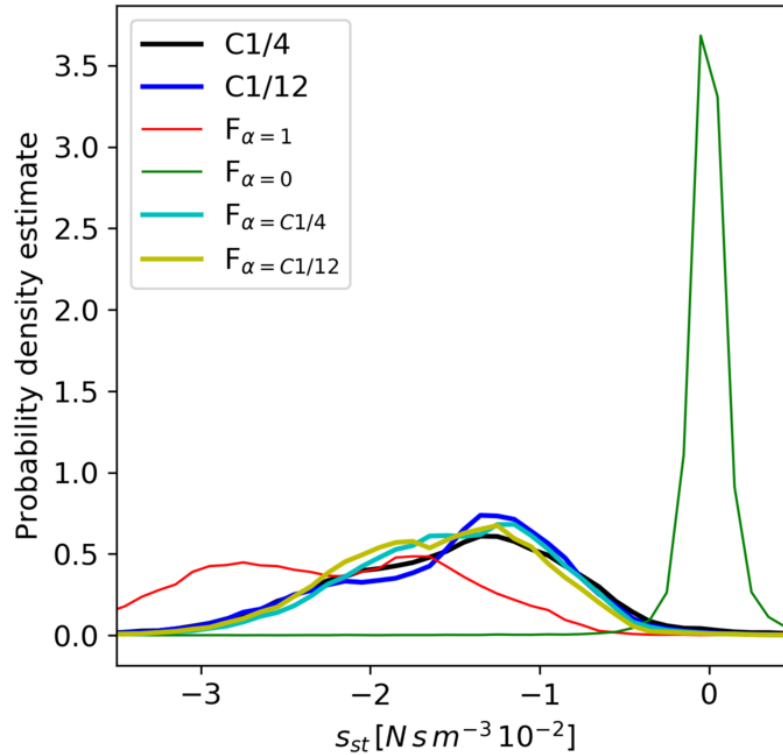
Figure 3.12: Normalized histogram (or probability density estimate) of ocean-surface current and wind stress coupling coefficient s_{st} for $2° \times 2°$ boxes from 60°S to 60°N (to exclude sea-ice regions). Grey areas in Fig. 2 are excluded.

simulations demonstrates proposed wind stress formulation is physically more consistent with respect to the coupled simulations than ocean-only models that do not take account of the re-energization.

3.4 Summary & Conclusions

In two high resolution coupled atmosphere-ocean models, we find a linkage between ocean surface currents and surface winds at the oceanic mesoscale. This linkage can be interpreted as a feedback from the ocean to the atmosphere as the linkage is missing in forced ocean-only models. Conceptually the feedback works as follows: Over ocean currents the wind work and energy transfer into the ocean is reduced leaving the winds stronger than in cases without ocean currents. This leaves imprints of the ocean currents in the winds. The strength of the coupling is illustrated by the coupling coefficient s_w. The strength of the coupling has pronounced spatio-temporal variability in a range of about 0.2 and 0.5 with large values over the WBC. The near-surface stability was identified as the main parameter for the variability of s_w. In conditions with strong near-surface stability the atmospheric surface layer is shallow and changes in the winds due to ocean surface currents are stronger than with a deep atmospheric surface layer. This is reflected in high positive correlations between the near-surface stability and s_w in particular over the WBC, i.e. a large share of the variability there is due to the near-surface stability.

The relationship between the ocean currents and the wind stress at the mesoscale can be described by another coupling coefficient s_{st}. This coupling coefficient can be seen as a measure of the mechanical damping of ocean surface currents as the stress excited by the ocean surface currents acts against them. The coupling was found to be mainly driven by the background wind speed, i.e. when winds are strong the coupling is stronger. These findings have been confirmed by observations (Renault et al., 2017a).

The most important part of this study concerns the issue that the mechanical coupling is found to be stronger in forced ocean-only models than in coupled atmosphere-ocean models. It is argued that the mechanical coupling is too strong in the forced ocean-only models because the feedback to the atmosphere is missing. Renault et al. (2016c) proposed a tentative implementation of the feedback by modifying Eq. 3.1 with $\alpha = 1 - s_w$. In the present study this tweak is tested for the first time using the spatially and temporally varying coefficient s_w estimated from the coupled models, the forced ocean-only models appeared to capture the principal features of the coupling coefficient s_{st} over energetic oceanic regions. For example, over the Gulf Stream Extension in January the coupling coefficient is about $s_{st} = -3.3$ in a forced ocean-only model. With the tweak in the momentum flux equation the coupling coefficient lowers to in the forced ocean-only model $s_{st} \approx 2.4$ which is only about 0.2 larger than the estimates from the coupled atmosphere-ocean models. It needs to be pointed out that the improvement in the coupling coefficient s_{st} for ocean-only models is quite important as it does show that the mechanical atmosphere-ocean coupling is more physically consistent with respect to the coupled models.

The present results extend the findings of the regional model study of Renault et al. (2016c) to the global ocean-atmosphere system. The strength of the feedback agrees with the findings of Renault et al. (2016c) who found for the CCS, based on a similar methodology, coupling coefficients of $s_{st} = -1.2 \pm 0.35$ and $s_w = 0.23 \pm 0.1$ based on 5 year data from their coupled model. These agree with the higher resolution model version C1/12 estimates for the coupling coefficient for a 5 year period in the CCS: $s_{st} = -1.26 \pm 0.13$ and $s_w = 0.28 \pm 0.04$. These findings are remarkably close given the differences in model setup and methodology. We also note that while thermal feedbacks from the ocean are not excluded from the coupling coefficients diagnosed from the coupled simulations, their influence on the re-energization effect has been shown to be small in a regional modelling system for the California Current System (Renault et al., 2016c).

We note several limitations of the method applied here: (1) For small curls of the ocean currents, the coupling coefficients appear to be biased, and cannot be robustly estimated (cf. Fig. A2). (2) The temporal and spatial scales of the atmosphere and ocean are not entirely separated. Therefore the results slightly vary with the cut-off length of the filter. (3) The results may depend on the parameterization of the vertical momentum flux in the atmospheric model. Further

research should examine turbulence resolving atmospheric models, perhaps in conjunction with prescribed ocean currents, to understand how the state of the atmosphere modifies the response of near-surface winds in the presence of ocean currents.

The misrepresentation of damping of surface currents due to missing re-energization of near-surface winds is an important topic and needs to be explored in further studies. We suggest three major constitutive steps: (1) to study the re-energization of near-surface winds due to surface currents in uncoupled turbulence resolving atmospheric models, e.g. LES models and explore the possibility to develop a parameterization for s_w based on atmospheric state parameters; (2) to validate the LES model results against the turbulence schemes as used in AGCMs; (3) when a parameterization of the re-energization effect is available, it could be tested in a suite of global experiments involving fully coupled atmosphere-ocean models and uncoupled ocean models. The construction of a forcing data set for the uncoupled simulations needs very careful treatment in order to be as close to the atmosphere from the coupled system as possible. Such a set-up would allow to minimize errors that are due to differences in the forcing such as temporal and spatial resolution of wind and differences in bulk formulations.

Appendix

Appendix A: Energy spectra

An inspection of high-resolution coupled model output (Fig. A1) suggests an upper bound of about 200km for the transition between wavelengths where the atmosphere is more energetic and wavelengths where the ocean is more energetic. We find that this scale separation is sometimes more pronounced, and in some regions not even valid. We show this exemplary for three regions: in a large box in the South Pacific, the atmospheric velocity spectral density dominates at all scales; in a rather small box in the North Pacific, we find a transition from atmospheric domination to oceanic domination at wavelengths of about 200km; in the Gulf Stream Extension, below wavelengths of 150km, atmospheric and oceanic velocity spectral densities are at the same level. As we are attempting to find a signal that is imprinted by the ocean on the atmosphere we need to consider energetic regions of the ocean. With conditions such as in the South Pacific, we will not be able to detect the oceanic imprint (discussed in Appendix B).
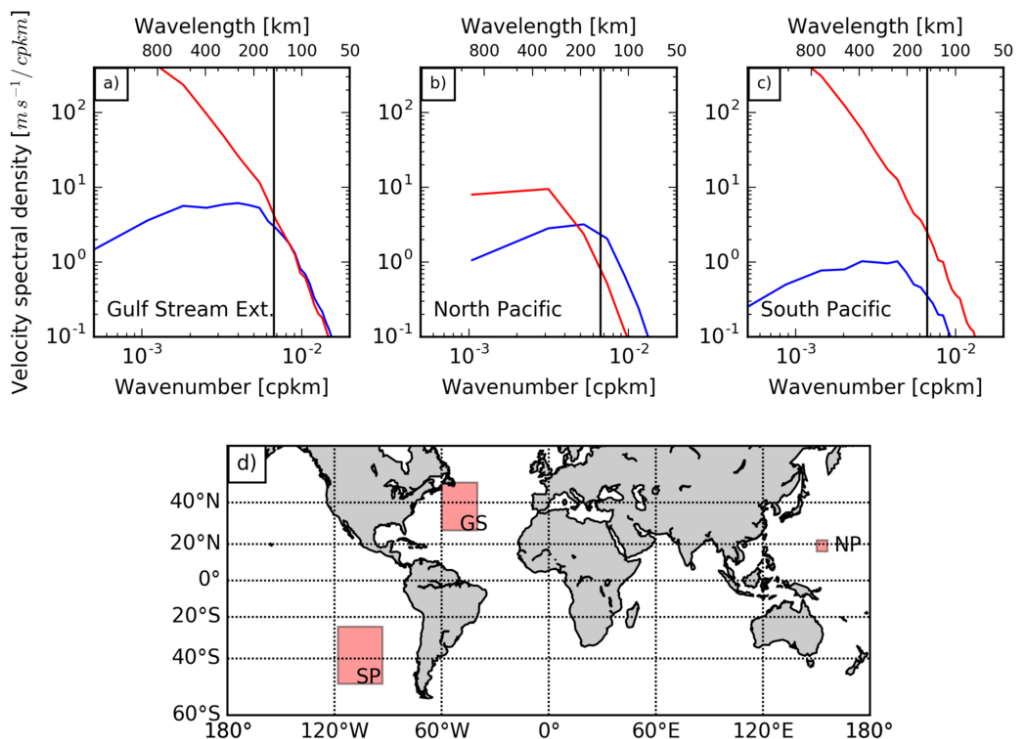
Figure A1: Isotropic wavenumber spectra of ocean velocity (blue) and wind speed (red) for (a) Gulf Stream Extension, (b) North Pacific and (c) South Pacific in C1/4 monthly output. The positions of the boxes are shown in (d). Vertical black lines represent the 150km wavelength to illustrate the cutoff length of the high-pass filter used for this study. The idea of using a high-pass filter is to exclude wavelengths where atmospheric variability is larger than oceanic. We see in the North Pacific (b) that at higher wavenumbers oceanic spectral density is larger that atmospheric and in the Gulf Stream Extension (c) they have the same order of magnitude. The 150km high-pass filter seems to be a good choice for the North Pacific box and for the Gulf Stream Extension box. In the South Pacific atmospheric variability dominates at all wavenumbers. This is also a region where we were not able to estimate coupling coefficients (see Fig 3.2).

Appendix B: Biased scatter plots

As seen in Fig. 3.1 the relationship between $curl(u)$ and $curl(wind)$ does not follow exactly the suggested linear fit. This becomes particularly problematic if the difference between the largest and smallest value of $curl(u)$ is relatively small, i.e. little spread along the x-axis. With such little spread of $curl(u)$ the estimation of the slope of the linear regression tends to be biased towards large values. This can be seen when mapping the spread of $curl(u)$ to the estimated s_w (Fig. A2). There we see that s_w and $\sigma(s_w)$ get large if $(max(curl(u)) - min(curl(u))) < 1$. We choose to ignore these values and mark them as grey areas in the figures with global maps.
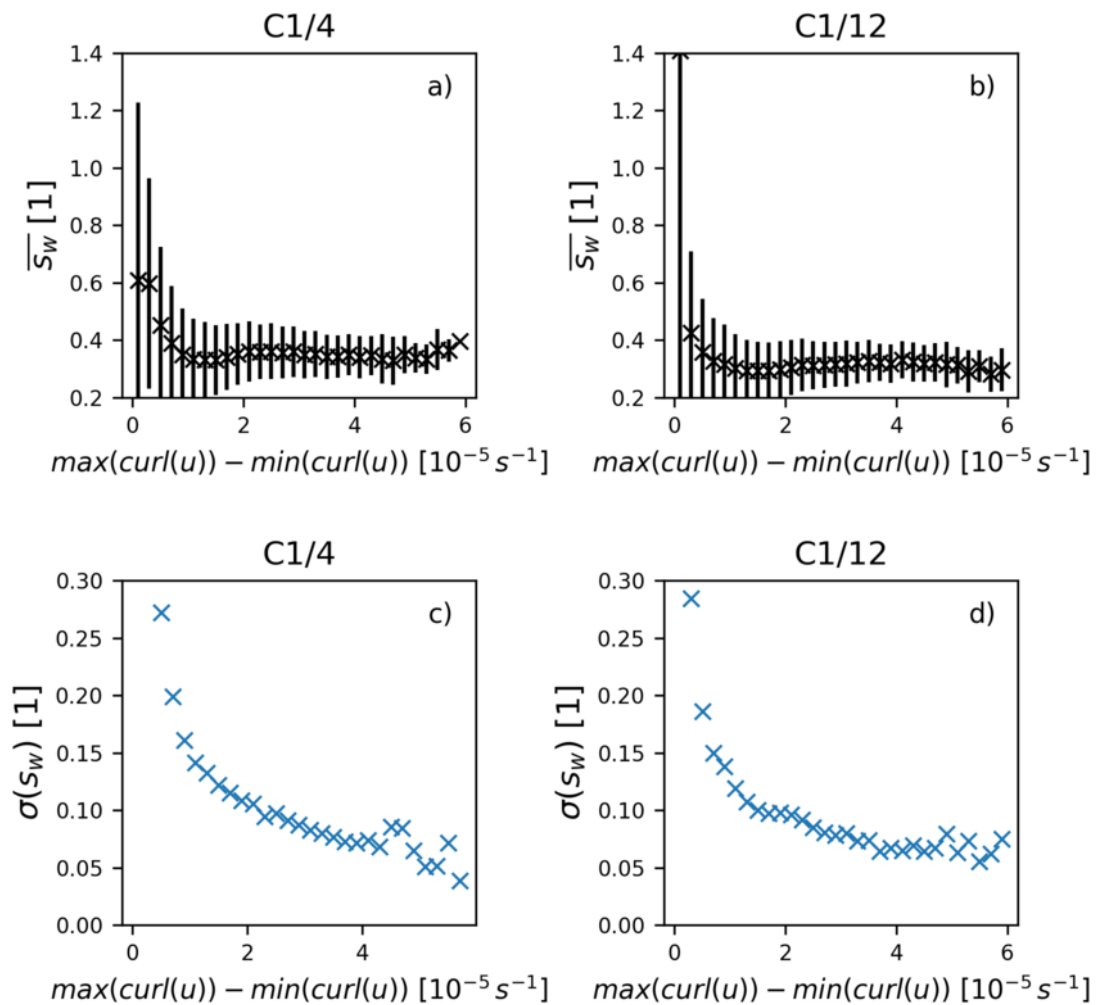
Figure A2: Coupling coefficient s_w as a function of $max(curl(u))$ - $min(curl(u))$ for (a) C1/4, (b) C1/12 and standard deviation of s_w for (c) C1/4, (d) C1/12. For small $|curl(u)|$ s_w and $\sigma(s_w)$ get larger. We see this as a problem of the method and therefore neglect values where range $|curl(u)| < 1$. Similar behaviour is seen for s_{st} and neglected as well. This results in the grey areas in Fig. 3.2, 3.5 and 3.9.

Appendix C: Degrees of Freedom estimation

The standard error of the slope of the linear regression is estimated by:

$$SE = \sqrt{\frac{SS_y/SS_x - b^2}{DOF}}, \tag{3.4}$$

where $SS_y = \sum(y_i - \bar{y}_i)^2$, $SS_x = \sum(x_i - \bar{x}_i)^2$, $\bar{\ }$ denotes mean, b is slope of linear regression and DOF are the degrees of freedom (DOF).

Given any three dimensional data set (two space and one time dimension) there will be coherence, meaning that time and space points can be dependent on each other. Therefore the DOF estimation needs to consider both temporal and spatial DOF. For the temporal DOF of freedom we follow Bretherton et al. (1999), estimating the ratio of effective sample size (ESS, N^*) to sample size N

$$N^*/N = \frac{1 - r_1 r_2}{1 + r_1 r_2}, \tag{3.5}$$

while $r_{1,2}$ is the lag-one autocorrelation for dataset 1,2. If only one dataset is used $r_1 = r_2$. For the spatial DOF estimation we use an adapted binomial method (B-method) of Livezey and Chen (1983) and Wang and Shen (1999), where a random time series is correlated with every spatial point since by chance some points will give a significant correlation with that random time series, the points with significant correlation share coherence, which is exploited to estimate the coherence of the field.

To estimate the total DOF of the given three-dimensional (with two spatial and one temporal dimension t) climate data set we combine the spatial (DOF_S) and temporal DOF estimation

$$DOF_{total} = DOF_S \cdot t \cdot N^*/N \tag{3.6}$$

Details of the estimation and a python-based program can be found at `https://github.com/RafaelAbel/DOF_estimation`.

Appendix D: Model vertical levels

Here we give a reduced list of the vertical levels of the atmospheric model. For a full list of the vertical levels we refer readers to Walters et al. (2017).

Level	Height (m)
1	10.00
10	730.00
20	2796.67
30	6196.67
40	10930.12
50	17012.40
60	24710.70
70	35927.89
80	58978.35
85	82050.01

Table A1: Reduced list of the total 85 vertical levels in the atmospheric model GA6.

4 Damping of ocean currents by mesoscale thermal and mechanical air-sea fluxes

This chapter presents the analysis of the mesoscale thermal and mechanical damping of surface currents in an global ocean model with moderate resolution $(1/4°)$. It reports that even at moderate resolution these damping mechanisms substantially contribute to the strength of surface currents. For the first time the relative importance of the thermal and mechanical damping mechanisms is directly compared and the results demonstrate that the mechanical damping is more effective to damp ocean surface currents.

Contents

4.1 Introduction

The importance of the atmosphere-ocean interface for Earth's climate system cannot be over-stated because most energy in mechanical form by winds and thermal form by heat or radiative fluxes enters the oceans through that interface. But there is also energy transfer from the ocean into the atmosphere: the air is warmed or cooled directly via sensible air-sea fluxes and longwave radiation, and energy in form of moisture is released into the atmosphere associated with the latent heat flux. Mostly these thermal fluxes (sensible, latent heat flux and outgoing long-wave radiation) are associated with a loss of energy from the ocean to the atmosphere and a reduction of sea surface temperatures (SST). This reduction happens non-uniformly on spatial scales and tends to reduce spatial gradients in SST. Accompanied with the reduction of SST gradients is the reduction of potential energy available for ocean dynamics often referred to as *thermal damping*. The mechanical wind power input is modified by the presence of ocean surface currents: ocean currents locally reduce the mechanical wind power input often referred to as *mechanical damping*.

In a recent study Ma et al. (2016) showed that the turbulent heat fluxes (THF; sensible and latent heat fluxes) associated with mesoscale SST anomalies provide a damping to the kinetics of mesoscale features and are important for the whole dynamics of Western Boundary Current (WBC) systems. The role of the THF for the ocean currents can be explained using the Lorenz energy cycle (more details in the methods section): as part of the baroclinic energy pathway, Eddy Potential Energy (EPE) is transformed to Eddy Kinetic Energy (EKE), i.e. mesoscale motions like oceanic eddies. EPE is associated with anomalies in the local buoyancy and these are influenced by SST and/or sea surface salinity anomalies. The SST or buoyancy spatial anomalies are damped by the THF and reduce the EPE that is available for the baroclinic pathway and finally results in a reduction of EKE.

When winds blow over the ocean they exerted stress on the ocean, generate waves and drive the surface ocean. This wind stress $\vec{\tau_{rel}}$ can be parameterized based on the difference between the wind $\vec{U_a}$ and the ocean current $\vec{u_o}$ using a bulk estimate:

$$\vec{\tau_{rel}} = \rho_a C_D |\vec{U_a} - \vec{u_o}|(\vec{U_a} - \vec{u_o}), \tag{4.1}$$

where ρ_a is the atmospheric density, C_D the drag coefficient. This formulation is referred to as *relative winds* as the relative velocity is considered. Even if the ocean currents speed is typically small with respect to the wind speed it plays an important role in reducing the work the winds do on the ocean currents. This reduction is referred to as *mechanical damping*. It can be qualitatively shown that the ocean currents reduce the wind work (Duhaut and Straub, 2006). The wind work is defined as the dot-product between wind stress and ocean currents, i.e. $P = \vec{\tau} \cdot \vec{u_o}$. To isolate the effect of ocean currents the wind stress can also be estimate neglecting the ocean currents and is termed *absolute winds*, i.e. $\vec{\tau_{abs}}$. Following Duhaut and Straub (2006) the dif-

ference in wind work is then $P_{diff} = P_{rel} - P_{abs} \approx -\rho_a C_D |\vec{U_a}| (|\vec{u_o}|^2 + (\vec{u_o} \cdot \vec{i})^2)$, when winds are large with respect to ocean currents and $\vec{i}$ is the a unit vector pointing in direction of $\vec{U_a}$. Note that quadratic terms in $\vec{u_o}$ have been neglected. In ocean models it can be shown that the mechanical damping leads to large reductions of the energy of the surface currents. So did Seo et al. (2016) show that mesoscale mechanical damping reduces the EKE in the California Current System (CCS) by 42%. Renault et al. (2016c) found a reduction by 27% in the CCS when using relative winds. Also for WBC the damping is particularly strong and reduces the EKE by 27% in the Gulf Stream (Renault et al., 2016b) and by 25% in the Agulhas Current system (Renault et al., 2017b). All these findings are based on ocean models with nominal resolutions of $1/10°$. Details on the thermal and mechanical damping mechanisms can be found in the methods section.

In this study, the mechanical and thermal damping mechanisms are investigated in a global ocean-only model with $1/4°$ resolution (ORCA025). In a suite of simulations the damping mechanisms artificially suppressed by spatially low-pass filtering the SST and ocean currents before the air-sea fluxes are calculated. Differences to a control simulation are then the result of the suppression of the damping mechanisms. The following questions will be addressed: How strong are the damping effects on surface kinetic energy? Are there significant changes in the main Western Boundary Current (WBC) regions? Is the mechanical or thermal damping mechanism stronger?

In section 2 the role of the air-sea fluxes in damping ocean surface currents is laid out in more detail. In section 3 the model and methods are introduced. In section 4 we first test how efficient the damping mechanisms are turned off, what their effects are on surface kinetics with focus on the WBCs. We demonstrate that the thermal and mechanical damping also play an important role at eddy-permitting resolution in particular in WBCs. The mechanical damping is found to be stronger than the thermal damping. In the Agulhas region the path of Agulhas rings is affected.

4.1.1 Background

The mechanical and thermal damping of ocean currents can be explained as part of the Lorenz Energy Cycle (LEC, Lorenz, 1955). With the continuous increase in computing power during the last decade it became possible to run Ocean General Circulation Models (OGCM) at resolutions (e.g., at about $1/10°$) that are able to permit ocean eddies. This made it possible for von Storch et al. (2012) to estimate a LEC for the global ocean. On a global mean through Reynolds averaging the LEC describes the time-mean balances between four energy reservoirs, their inputs by forcing, and outputs primarily through dissipation and conversions between the reservoirs. The main focus of this work is to investigate how thermal and mechanical surface forcing description change the oceanic energy cycle with focus on the kinetics. As schematically shown in Fig. 4.1 the reservoirs are available potential energy (MPE) and kinetic energy (MKE)

of the mean circulation, and available potential energy (EPE) and kinetic energy (EKE) of the time-varying circulation. The energy reservoirs MPE, MKE and EKE are to first approximation isolated, meaning generation and dissipation are nearly balanced. The forcing can be separated into mechanical and thermal, and largescale (top) and small- or meso-scale (bottom) of Fig. 4.1. In a global coupled atmosphere-ocean model von Storch et al. (2012) estimated that the LEC is by about 60% forced by the wind and by 40% by buoyancy fluxes. The main conversion routine associated with vertical flow shear (baroclinic) is about 6 times larger than the conversion due to horizontal flow shear (barotropic). The time-varying flow EKE is nearly three times more energetic than the time-mean flow MKE.
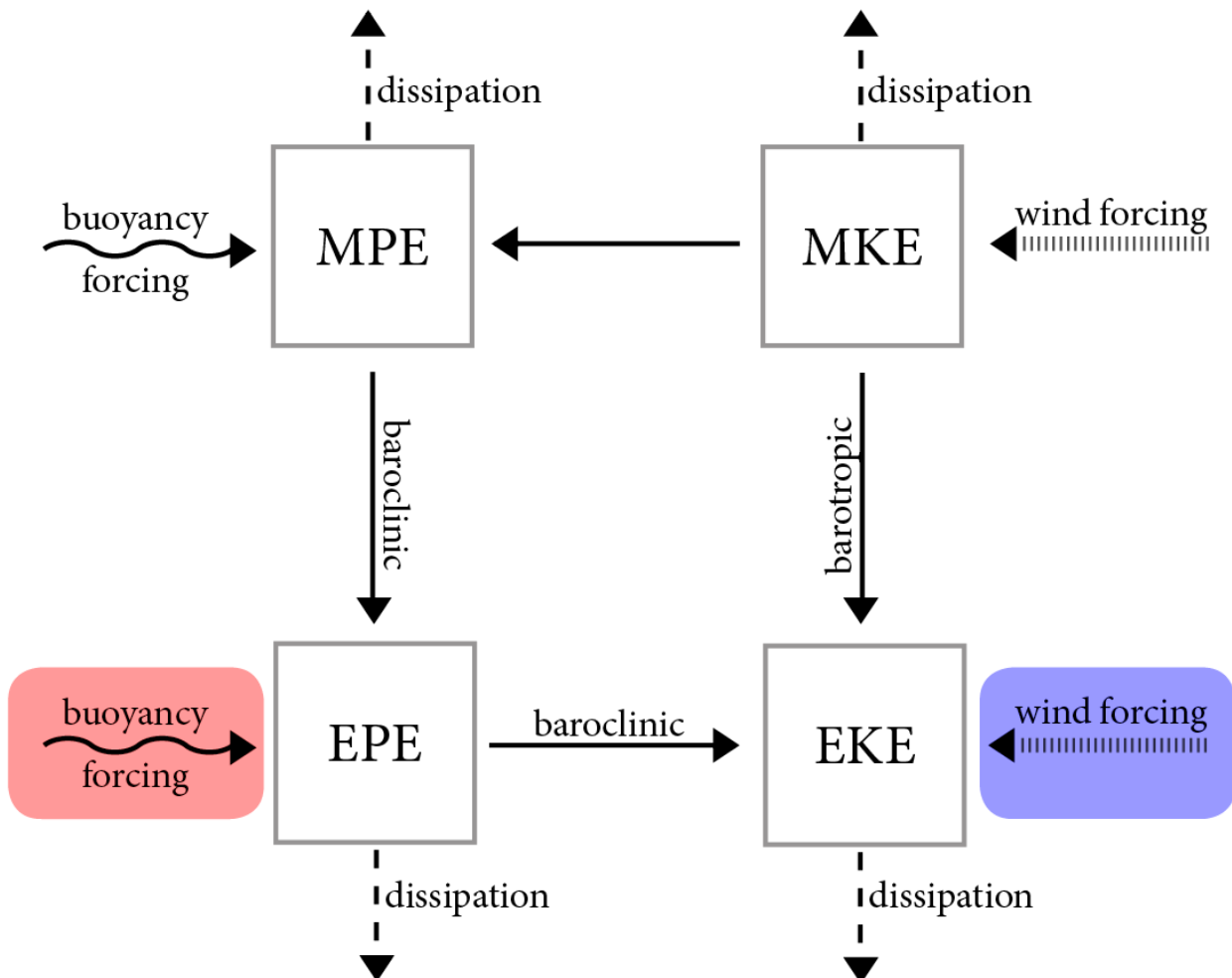
Figure 4.1: Schematic oceanic Lorenz Energy cycle (LEC). Energy reservoirs Mean Potential Energy (MPE), Mean Kinetic Energy (MKE), Eddy Potential Energy (EPE), and Eddy Kinetic Energy (EKE). The conversion between energy reservoirs holds only on a global mean. In this study the mesoscale mechanical (blue box) and thermal damping (red box) are suppressed.

The reservoirs of energy discussed in this study are the EPE and EKE. The EPE is defined by:

$$EPE = \rho_0 \frac{b'^2}{2N_r^2}, \tag{4.2}$$

where b' is the spatial buoyancy anomaly, N_r the buoyancy frequency associated with a predefined background potential density profile rho_r that is chosen to be the area average of the time-mean potential density (referenced to the sea surface) in the analysis domain. The EKE is defined by the velocity fluctuations around the mean $u' = u - \bar{u}$, where $\bar{\cdot}$ denotes the time-mean:

$$EKE = 1/2\sqrt{u'^2 + v'^2} \tag{4.3}$$

In the LEC the mesoscale mechanical and thermal damping mechanisms are considered to be part of the mesoscale forcing and are highlighted by coloured boxes in Fig. 4.1. The exact forcing fluxes are shown below. The main driver of thermal air-sea fluxes is the atmosphere, but the SST also contributes to the sensible heat flux (SH), the evaporation (E) and therefore latent heat flux (LH), and the outgoing long-wave radiation (LW). The turbulent air-sea fluxes, SH, E and LH are commonly estimated using bulk formulations of the form:

$$
\begin{aligned}
SH &= \rho_a c_p C_\theta |\vec{U} - \vec{u}|(T_A - SST) & \text{(4.4a)} \\
E &= \rho_a |\vec{U} - \vec{u}| C_e (q - q_{sat}) & \text{(4.4b)} \\
LH &= \Gamma_V LH, & \text{(4.4c)}
\end{aligned}
$$

with ρ_a air density, C_θ and C_e transfer coefficients of heat and for evaporation, respectively, U wind speed at 10 meter, u surface current velocity, SST Sea Surface Temperature, T_A 10 meter atmospheric temperature, Γ_V latent heat of vaporization, q humidity at 10 meter, and q_{sat} saturation humidity (note that the saturation humidity at the ocean surface is a function of the SST). The outgoing long-wave radiation is solely a function of sea surface temperature (SST) in Kelvin:

$$LW = -\sigma SST^4, \tag{4.5}$$

where $\sigma = 5.67 \cdot 10^{-8}$ W m^{-2} K^{-4} is the Stefan-Boltzmann constant. A negative flux is directed from the ocean into the atmosphere and associated with heat loss.

The density of sea water depends on temperature and salinity. At the sea surface heat and moisture fluxes modify temperature and salinity which results in a change of buoyancy of the surface waters. The net surface heat flux Q_{net}, the rate of evaporation (E) and precipitation (P) determine the surface buoyancy flux (B_0):

$$B_0 = -g\alpha Q_{net}/(\rho c_p) + g\beta(E - P)S_0, \tag{4.6}$$

where g is gravity, ρ ocean density, c_p specific heat capacity, $\alpha = -\rho^{-1}\partial\rho/\partial T$ is the effective thermal expansion coefficient, $\beta = -\rho^{-1}\partial\rho/\partial S$ is the effective haline contraction coefficient, and S_0 surface salinity. Surface cooling or evaporation results in a positive buoyancy flux and makes the surface waters less buoyant. When less buoyant (heavier) waters lie above more buoyant (lighter) waters, the water column is convectively unstable and overturning can occur. In this process waters below the mixed layer can get entrained and the mixed layer deepens. Convective overturning is a crucial process to form subsurface water masses. Conversely, when heat fluxes warm the surface waters or excess precipitation result in a negative buoyancy flux, the surface water become more buoyant. The stably stratified waters then effectively limit turbulent mixing with waters below the thermocline. In terms of buoyancy a heat flux of 20 W/m^{-2} is approximately equivalent to a 5 mm day^{-1} freshwater flux (Cronin and Sprintall, 2001). Note that the wind also contributes to buoyancy changes in the mixed layer by entrainment.

4.2 Models and Methods

4.2.1 Model and experimental set-up

The mesoscale mechanical and thermal damping is not a feedback mechanism between atmosphere and ocean, but rather an inherent feature of the air-sea fluxes. The damping acts on mesoscale features of the ocean due to their imprints in surface velocity and SST. This is why in this study an ocean-only model is used. Another benefit is that feedbacks with the atmosphere are eliminated and all simulations can be forced with the same atmospheric fields. The ocean-only experiments are based on NEMO (version 3.4) in an ORCA025 configuration. This configuration uses a tripolar grid at a nominal resolution of $1/4°$, and 46 vertical levels with a resolution of 6m near the surface and 250m at depth. Surface-forcing fields build on the Coordinated Ocean-Ice Reference Experiments (CORE, Large and Yeager, 2009; Griffies et al., 2009) and have a spatial resolution of 1.875°. Turbulent air-sea fluxes are calculated using the bulk formulae by Large and Yeager (2004).

The ocean-only experiments it is intended to demonstrate the effects of the mesoscale mechanical and thermal damping. Therefore a control experiment (CTRL), an experiment where the mechanical damping is turned off (M_off), an experiment where the thermal damping is turned off (T_off) and an experiment where both damping mechanisms have been turned off (MT_off). Find experiment details in Tab. 4.1. The experiments were started from a 30-yr spinup (1980-2009) from a relative wind simulation and then carried out through 1989-2004. The switching off has been achieved using a spatial low-pass filter on the SST and the surface currents before the air-sea fluxes are calculated. A 2nd order Shapiro filter with 300 iterations has been used. In an unfiltered SST snapshot large scale north-south gradients as well as mesoscale features are

Experiment	Mechanical damping off	Thermal damping off
CTRL	NO	NO
M_off	YES	NO
T_off	NO	YES
MT_off	YES	YES

Table 4.1: List of experiments. All experiments are identical to the control experiment (CTRL) except, that either mechanical damping is suppressed (M_off) or that thermal damping is suppressed (T_off) or both (MT_off). In order to suppress mesoscale thermal an mechanical fluxes the surface currents and/or the SST was low-pass filtered using a 2nd order Shapiro filter with 300 iterations.
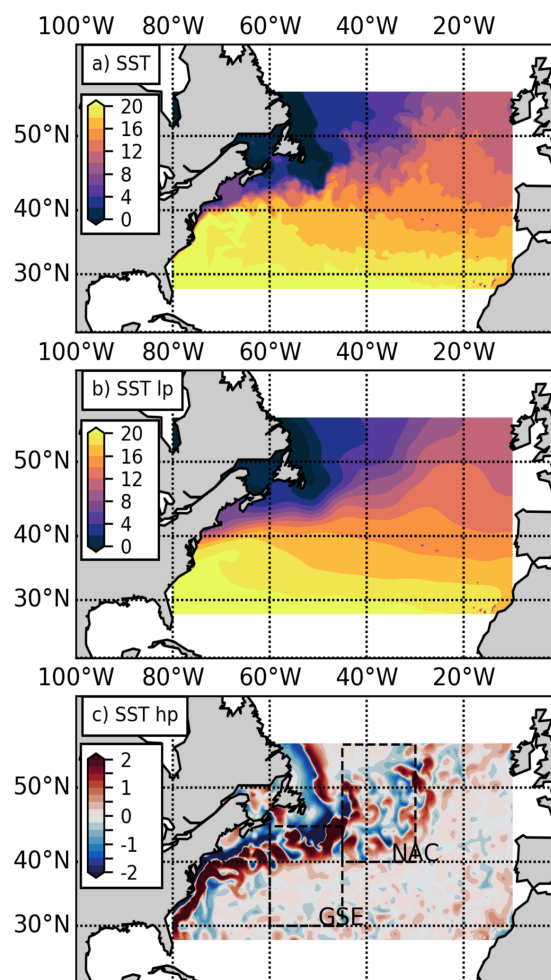
Figure 4.2: Snapshot of SST [$°C$] in the North Atlantic. (a) SST 5 day mean, (b) low-pass and (c) high-pass filtered with a 2nd order Shapiro filter with 300 iterations. Boxes denote regions Gulf Stream Extension (GSE) and North Atlantic Current (NAC) that are used in Fig 4.3.

recognizable (Fig. 4.2a). When the low-pass filter is applied the zonal SST structure on top of the large scale signal from North Atlantic Current is preserved. The high-pass signal clearly shows the mesoscale SST structure associated with the Gulf Stream and North Atlantic Current. The

low-pass filter removes variability on all spatial scales and can be visualized by a wavenumber spectrum for the Gulf Stream Extension and North Atlantic Current (Fig. 4.3). At large spatial scales the spectral density of the low-pass filtered SST is about an order magnitude lower than for unfiltered SST and at wavelengths smaller than 300km most of the variability is removed. This means that the filter used here is not entirely focused on the mesoscale, but also removes some variability on larger scales. With an low-order Shapiro filter used with a large number of iterations it seems inevitable to focus entirely on the mesoscale. Higher order filter turned out to be not feasible with the technical setup used to run the simulations, i.e. to build averages across CPU borders.
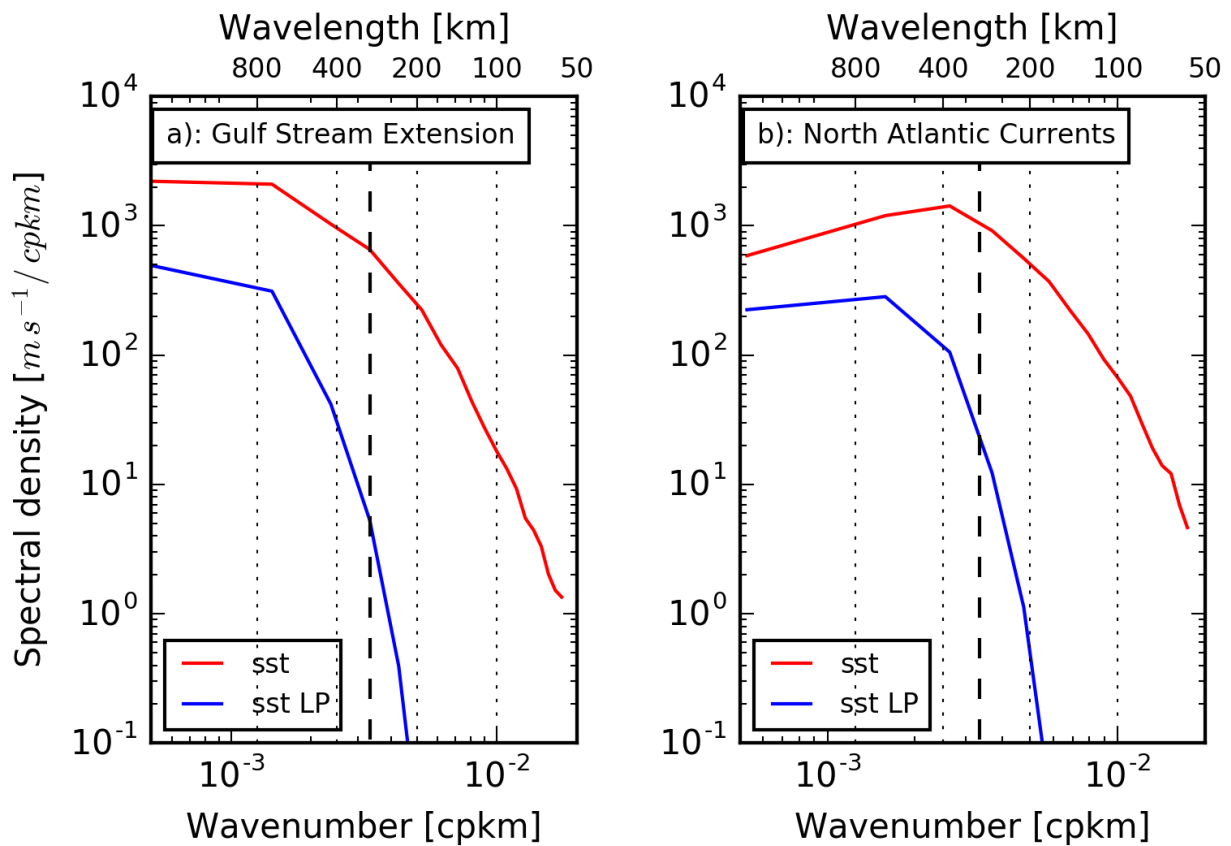
Figure 4.3: Isotropic wavenumber spectra of SST (red) and low-pass filtered SST (blue) for (a) Gulf Stream Extension and (b) North Atlantic Current. Positions are shown as boxes in Fig. 4.2.

4.2.2 Eddy detection, tracking and composites

Detection and tracking of mesoscale eddies was accomplished using 5-daily fields of sea surface height (ssh) with the tracking algorithm of Chelton et al. (2011) and modified for NEMO output by Oliver et al. (2015). Criteria for the eddy detection are (i) ssh exceeds a threshold (here: 1cm), (ii) the eddy area needs to be larger than a circle with radius $0.4°$ (geographical degrees), (iii) a local minimum or maximum for the ssh is found for cyclonic or anticyclonic eddies, respectively, and (iv) the dimensions of the detection region needs to be smaller than 400km (only valid equator-ward of $25°$N and S). Eddy detection was done for every 5-day time-step. The eddy tracks are based on the detected eddy positions. An eddy of an successive time step belongs to the same track if it falls within a specified ellipsoid centred at the eddy. The north-south dimension of the ellipsoid is 150km and the east-west dimension is given by the length of the first baroclinc Rossby wave (Chelton et al., 1998). Further details are given in Chelton et al. (2011).

4.3 Results

4.3.1 Reduction of Thermal and Mechanical Damping

In this section a measure for thermal and mechanical damping is introduced and it is shown how this damping is effectively reduced in the experiments M_off, T_off and MT_off. Once it is shown, that the damping is reduced the consequences can be investigated. In the ocean small scale fronts and mesoscale features are abundant. Under certain conditions the air-sea fluxes can be linked to the properties of the surface ocean. At the oceanic mesoscale (here defined as spatial scales about 200km or smaller) the ocean surface properties have a major influence on the air-sea fluxes.

In this section we demonstrate how the mesoscale ocean currents and SST are related with the curl of the wind stress and the THF anomaly, respectively. In the following these relationships will be used as measures of the thermal and mechanical damping. As a typical example of the oceanic mesoscale and the associated imprints on the surface ocean consider an anticylonic eddy shed by the Agulhas current into the Atlantic Ocean (Fig. 4.4a). These eddies are associated with relatively strong surface currents and a sea level anomalies (SLA). In this exemplary anticylonic eddy the curl of the surface velocity ($curl(\vec{u}) = \partial v/\partial x - \partial u/\partial y$) is positive and is associated with an anomaly in the curl of the wind stress (Fig. 4.4b). From Eq. 2.1 it is obvious that a surface current results in a wind stress of opposing sign. The same is true for a curl of a surface current. As the wind stress acts as a forcing for the surface currents the opposing sign in the curl of the wind stress can been seen as a damping of the curl in the surface current. Typically these mesoscale current features are also associated with mesoscale SST anomalies (Fig. 4.4c). For the same anticyconlic eddy we find positive SST anomalies to the north-west and negative
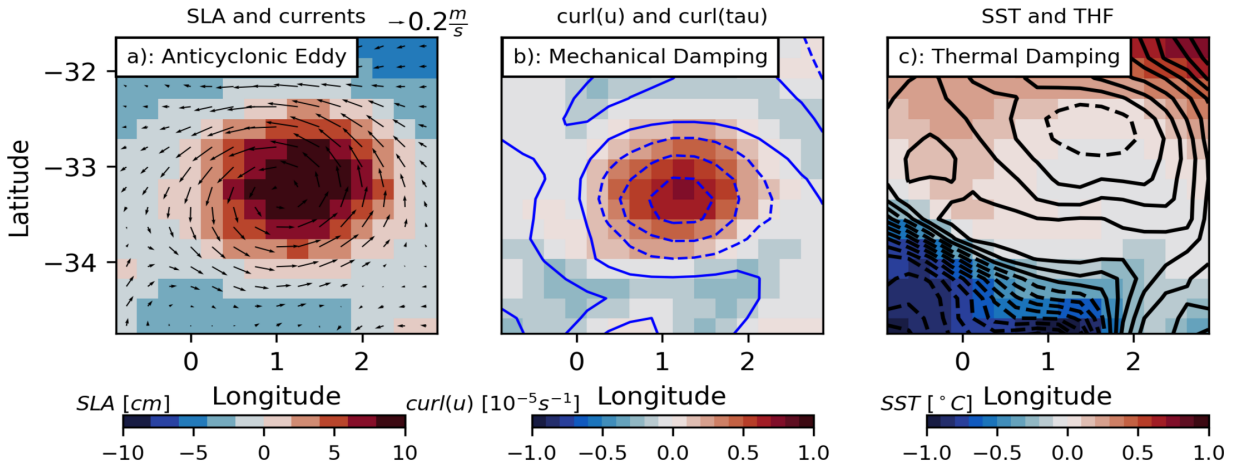
Figure 4.4: Eddy characteristics and damping mechanisms. An anticyclonic eddy (Agulhas Ring) in the Atlantic Ocean and it's (a) sea level anomaly (SLA; color) and surface currents (arrows), (b) curl of the surface current, curl(u) anomaly (color) and anomaly of curl of the wind stress (τ; CI: $0.2 \cdot 10^{-7} Nm^{-3}$), and (c) SST (color) and turbulent heat flux anomaly (THF: sensible + latent heat; CI: 2 Wm^{-2}). A surface current anomaly results in a wind stress anomaly with opposing sign which then reduces the surface current or EKE (mechanical damping). A negative SST anomaly results in reduced or negative THF which is effectively a warming and reduces the spatial SST anomalies or EPE (thermal damping). Anomalies are calculated with respect to the spatial mean of the areas.

SST anomalies to the south-west. This SST distribution also shapes the THF (Eq. 4.4) and the outgoing longwave radiation (Eq. 4.5) and results in negative THF where SST anomalies are negative and positive THF where SST anomalies are positive. As a consequence the stronger thermal heat fluxes over warmer SST will ultimately lead to a reduction of the SST anomalies and therefore also a reduction of EPE. The example illustrates how the surface properties can be linked to the air-sea fluxes. Generally an anomaly of the curl of the ocean current can be associated with an anomaly of the curl of the wind stress with reversed sign. SST anomalies can be linked to THF anomalies. These two relationships can thus be regarded as manifestations of the mechanical and thermal damping, respectively. In the following by, using these relationships, it will be demonstrated that the mechanical and thermal damping can be reduced.

In order to suppress the mesoscale air-sea fluxes and the associated damping of surface currents in the experiments T_off (thermal off), M_off (mechanical off) and MT_off (mechanical and thermal off) the SST and surface currents have been low-pass filtered before calculating the air-sea fluxes (see Tab. 4.1). The imprint of mesoscale air-sea fluxes as exemplary shown for an anticyclonic eddy (Fig. 4.4) can be quantified following Ma et al. (2016) and chapter 3 for thermal and mechanical coupling, respectively. Over the Gulf Stream a strong positive relation between mesoscale SST and mesoscale THF can be found: When the SST is not low-pass filtered in CTRL and M_off the coupling coefficient is $s_{th} \approx 44$ Wm^{-2}K^{-1} (Fig. 4.5). This implies a THF increase of about 44 Wm^{-2} (into the atmosphere) per 1 K SST increase. This is also close to the 40–56 Wm^{-2}K^{-1} Ma et al. (2016) find for the Kuroshio Extension region. The coupling strength

found here and in Ma et al. (2016) is relatively close to what is excepted from the THF bulk formulations (Eq. 4.4): The coupling strength of the flux changes for a 10 ms^{-1} background wind (and no ocean current) is for sensible heat flux 8 (15) Wm^{-2}K^{-1} for stable (unstable) conditions, and for the latent heat flux 33.5 Wm^{-2}K^{-1}. This coupling is effectively suppressed if the SST is low-pass filtered for the air-sea flux calculation (T_off and MT_off) with values of $s_{th} \approx 15.8$ Wm^{-2}K^{-1}. This means that damping of SST anomalies is reduced and thus SST anomalies can persist for a longer period of time.

The strength of the mechanical coupling can be measured by the slope of the linear regression between the curl of the ocean current and the curl of the stress, s_{st}. Additionally to the curl a high-pass filter with cutoff-length of 150km was used to suppress the main signal in the wind stress that is due to the wind. Recall the example of the anticylonic eddy (Fig. 4.4b) that demonstrated that the relationship between the curl of the ocean currents and the curl of the wind stress is negative. In the experiments where the surface currents are not low-pass filtered (CTRL and T_off), we find that negative relationship expressed by a coupling coefficient $s_{st} \approx -3.0 \cdot 10^{-2}$ N s m^{-3} (Fig. 4.6). Renault et al. (2017a) demonstrated that s_{st} has a negative linear relationship to the background wind, i.e. the coupling is stronger (more negative) for stronger background winds. When we low-pass filter the surface currents for the air-sea flux calculation the coupling seems to be fully suppressed (Fig. 4.6b,d) which leads to coupling coefficients $s_{st} \approx 0 \cdot 10^{-2}$ N s m^{-3}. The strengths of the coupling coefficients s_{th} and s_{st} demonstrate that the thermal damping is reduced in T_off and MT_off and the mechanical damping is reduced in M_off and MT_off. Similar conclusions can be drawn for other energetic regions of the oceans (not shown).
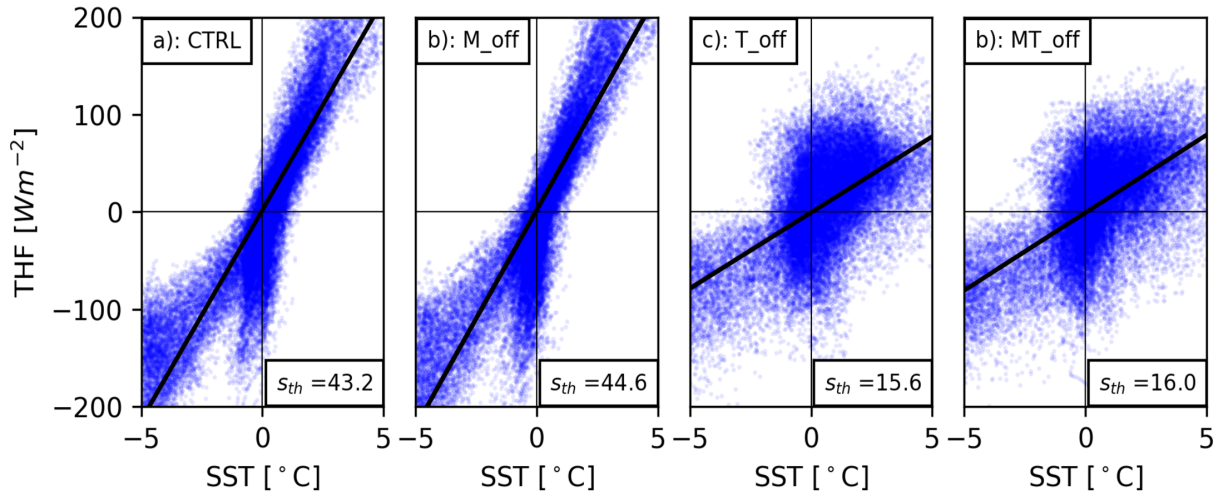
Figure 4.5: Mesoscale thermal damping: THF and SST relationship with coupling coefficient s_{th}. Scatterplot and linear regression (lines) and slope of the linear regression, s_{th}, between high-pass filtered (500km boxcar filter) 5d-daily mean SST and THF for (a) CTRL, (b) M_off, (c) T_off, and (d) MT_off for the winter months (ONDJFM) from 2000-2004 over the Gulf Stream (36-41°N, 67-72°W). The coupling is stronger in winter than in summer. For CTRL and M_off the coupling coefficient is large ($s_{th} \approx 44$) between SST and THF demonstrating the active role of the SST in driving the THF. When the mesoscale SST anomalies are filtered out (T_off and MT_off) the coupling coefficients is reduced ($s_{th} \approx 16$), which is equivalent to a reduction in the mesoscale thermal damping.
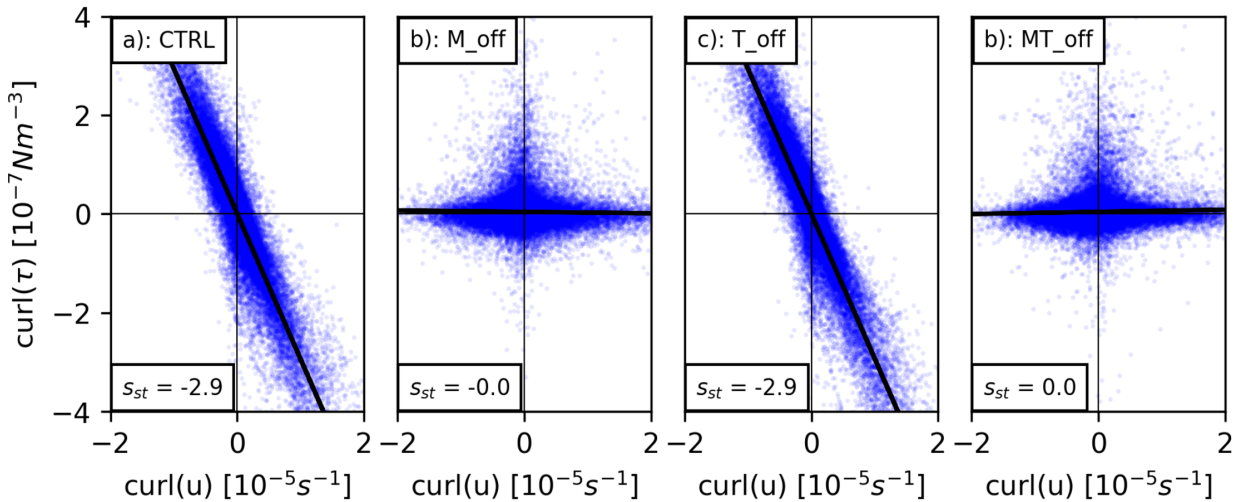
Figure 4.6: Ocean-surface current and wind stress relationship and coupling coefficient s_{st} [10^{-2} N s m^{-3}] defined by the slope of the linear regression for (a) CTRL, (b) M_off, (c) T_off, and (d) MT_off for the winter months (ONDJFM) from 2000-2004 monthly means over the Gulf Stream (35-45°N,62-72°W). Linear regressions are depicted by solid lines and the slope (s_{st}) are printed within the plots. A spatial high-pass filter (150km boxcar filter) and the curl of the surface currents and wind stress was calculated.

4.3.2 Global MKE and EKE changes

In the last section it was shown that in M_off and MT_off the mechanical and in T_off and MT_off the thermal damping was suppressed. This has consequences for the surface kinetics. The suppression of mesoscale thermal and mechanical damping mechanisms leads to a general increase

in kinetic energy. In the ORCA025 configuration the global spatial pattern of MKE and EKE is relatively well resolved (Fig. 4.7; note that MKE and EKE are scaled by $\sqrt{2MKE}$ and $\sqrt{2EKE}$ to have more practical units of cm s^{-1}), although values are lower than observational estimates from satellite altimetetry and models with higher horizontal resolution (e.g. Barnier et al., 2006; Hurlburt and Hogan, 2000; Abel, 2013). Even in the long-term mean the EKE exceeds 50-60 cm s^{-1} in the Western Boundary Current (WBC) regions and their extensions, the equatorial current bands, and the Antarctic Circumpolar Current (ACC) (Fig. 4.7e-h). When the mesoscale mechanical damping is suppressed (M_off) the EKE generally increases exceeding 40 cm s^{-1} locally in the Agulhas region, but also increases by 10-30 cm s^{-1} in other energetic regions like the tropics and WBC regions. Sometimes in particular in the ACC, swaths of increasing EKE is also associated with a decrease in adjacent swaths, which might be explained by a shifted front. When mesoscale thermal damping is suppressed (T_off) the changes are considerably smaller with respect to M_off, but can exceed 30 cm s^{-1} in energetic regions. Dipole patterns are more abundant in this case, which might be due to shifts in fronts and/or pathways of eddies. When both the mesoscale thermal and mechanical damping are suppressed (MT_off) the changes in EKE resemble the changes found due to the suppression of mechanical damping alone (M_off), but are somewhat stronger, showing that the thermal and mechanical damping effects add up (see e.g., the Gulf Stream Extension).

Likewise as for the EKE the MKE maxima of the world oceans are concentrated in the WBC, equatorial current bands, the ACC and a few other (Fig. 4.7a-d). When suppressing the mesoscale mechanical damping (M_off), a strong increase in MKE is found in the energetic regions. Additionally to that dipole patterns can be found in the Gulf Stream, Kuroshio, Agulhas and ACC regions, reaching up $\pm$ 40 cm s^{-1}, associated with shifts of the mean currents. Likewise, but less intense changes are found when the mesoscale thermal damping is suppressed (T_off). Comparison of the changes in MKE and EKE show that the mechanical damping is more effective than the thermal. A more quantitative view will be given later. The combined effects of the suppressed mesoscale thermal and mechanical damping (MT_off) can superimpose like in the ACC where the MT_off effect exceeds the effect of M_off alone.
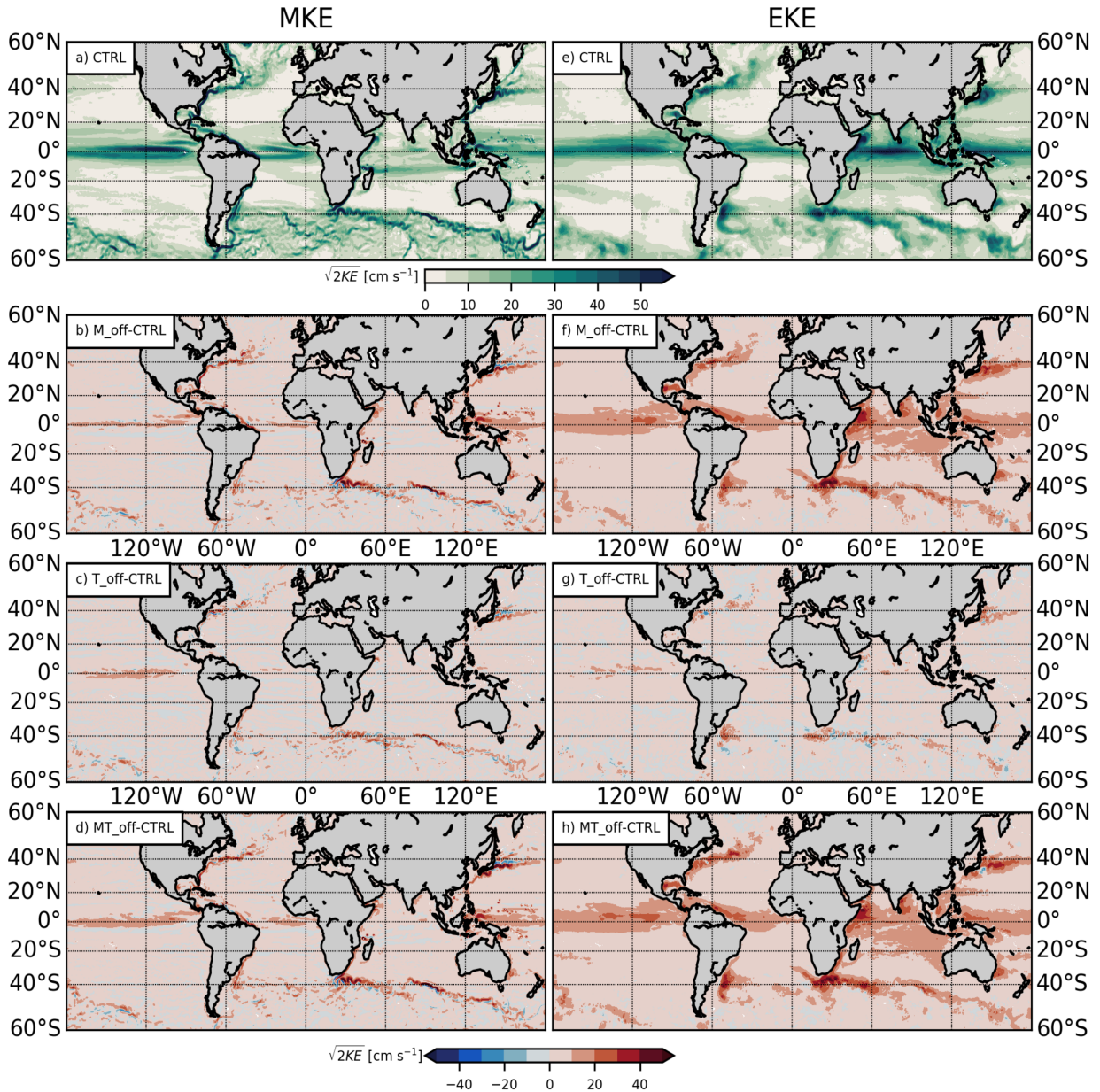
Figure 4.7: Global distribution of surface (a-d) $\sqrt{2MKE}$ and (e-h) $\sqrt{2EKE}$ [cm s^{-1}] averaged from 1990-2004. Time-mean (a,e) CTRL and differences (b,f) M_off minus CTRL, (c,g) T_off minus CTRL, and (d,h) MT_off minus CTRL.

4.3.3 Gulf Stream and Kuroshio response

In the wind-driven ocean circulation theory, the subtropical gyres are driven by the large-scale wind stress that accelerates the ocean. The western intensification through planetary waves that transport the energy gained through the winds westward leads to strong western boundary currents (WBC) like the Kuroshio and the Gulf Stream. Additionally to that it is demonstrated that important aspects of the WBC are also determined by the mesoscale air-sea fluxes, following Ma et al. (2016), and furthermore the investigations are extended to the mechanical damping. The Gulf Stream and the Kuroshio extensions and their associated eddy variability are the focus of

this section.

For the Gulf Stream and its extension suppression of the thermal and mechanical damping leads to considerable changes in the currents strength and path (Fig. 4.8). When the mechanical damping is turned off (M_off) the Gulf Stream appears to be stronger and the separation from the coast to be more southward. When the thermal damping is turned off (T_off) we find the inverted image: The Gulf Stream appears to be weaker and the separation is more northward. In MT_off the mechanical effect dominates and we find a similar but weakened signal with respect to M_off. Further downstream at $60°W$ the core of the mean current is stronger, more confined and shifted southward in M_off than in CTRL (Fig. 4.9e,g). Also in M_off at about $38°N$ a mean westward velocity is present, which might be associated with a recirculation or shedding of eddies. For T_off only a minor reduction of the mean jet is found. For MT_off we find an mean current of similar strength with respect to M_off, however there is now southward shift and therefore the difference to CTRL appears to be rather small.

The Kuroshio regime responds with changes of similar amplitude (Fig. 4.9). For M_off the separation from the coast is also more southward and the mean jet is stronger and shifted southward between $145°E$-$160°E$. These changes are similar to the responses found in the Gulf Stream. For T_off the changes are more obvious than in the Gulf Stream: The separation is more southward and also the mean jet is shifted southward. In MT_off the suppression of the mechanical and thermal damping lead to an very early separation of the Gulf Stream from the coast and even stronger effects than in M_off (Fig. 4.9d). Further downstream the mean jet intensifies and shifts southward by about $2°$.
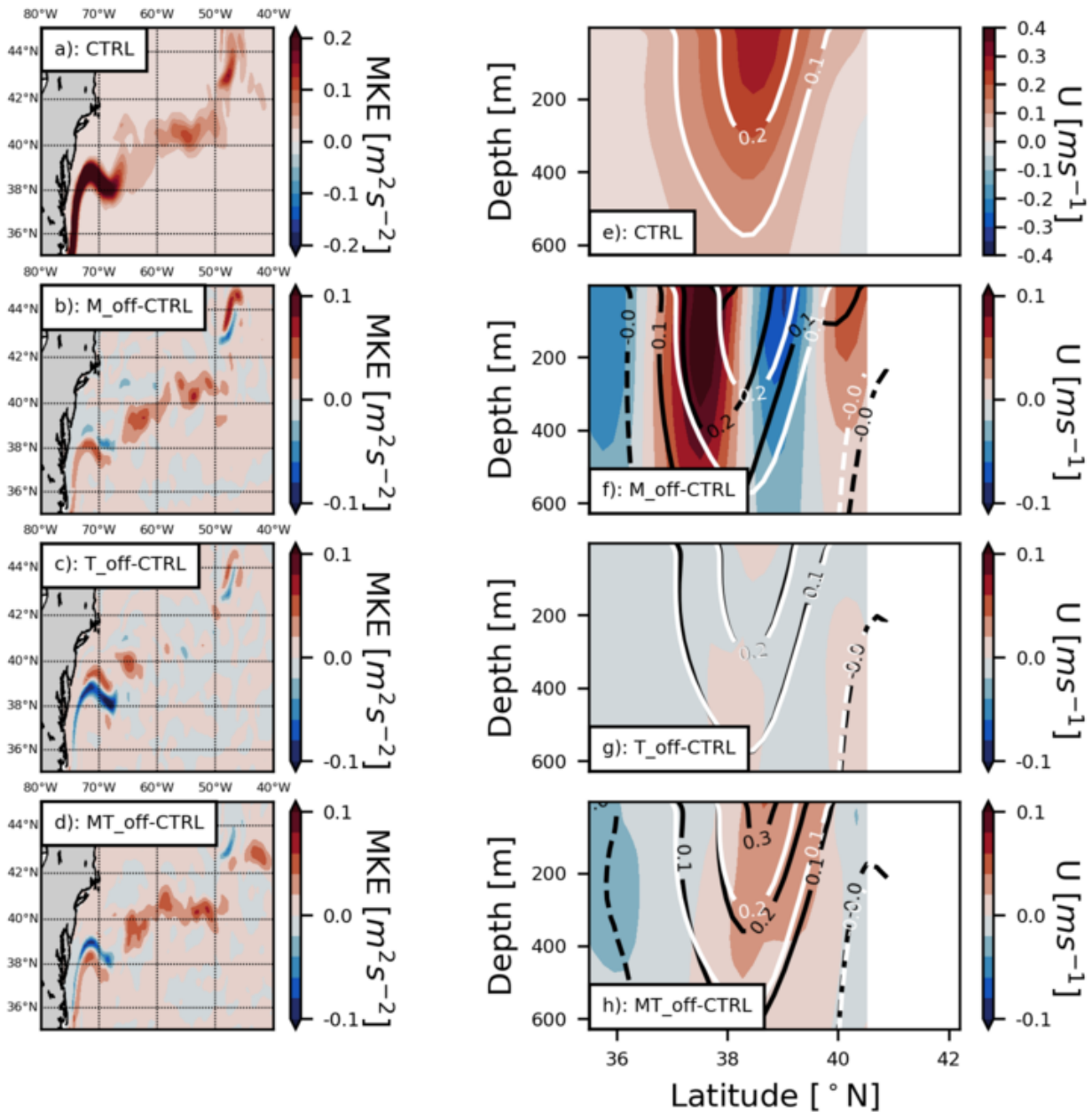
Figure 4.8: Gulf Stream and Extension response to mesoscale thermal and mechanical feedback. Vertically averaged (top 100m) mean kinetic energy for (a) CTRL, (b) M_off minus CTRL, (c) T_off minus CTRL, (d) MT_off minus CTRL. Vertical sections of zonal velocity U zonally averaged from (58°W-62°W) for (e) CTRL, (f) M_off minus CTRL, (g) T_off minus CTRL, (h) MT_off minus CTRL based on 1990-2004 averages. The contour lines denote the zonal velocities for (f) M_off, (g) T_off, (h) MT_off (black) and CTRL (white).

The kinetic energy spectra give a more quantitative view on the distinct changes described above. Fig. 4.10 shows the ratio between the KE spectra of M_off, T_off and MT_off with respect to CTRL for Kuroshio Extenstion, Gulf Stream Extension and Agulhas region. A ratio of 1.0 denotes no change and 1.5 denotes 50% increase. Generally there is an increase in KE if either the mechanical and/or the thermal damping is suppressed. If mechanical damping is suppressed (M_off) we find an increase in KE of up to 60% in the Kuroshio Extension and up
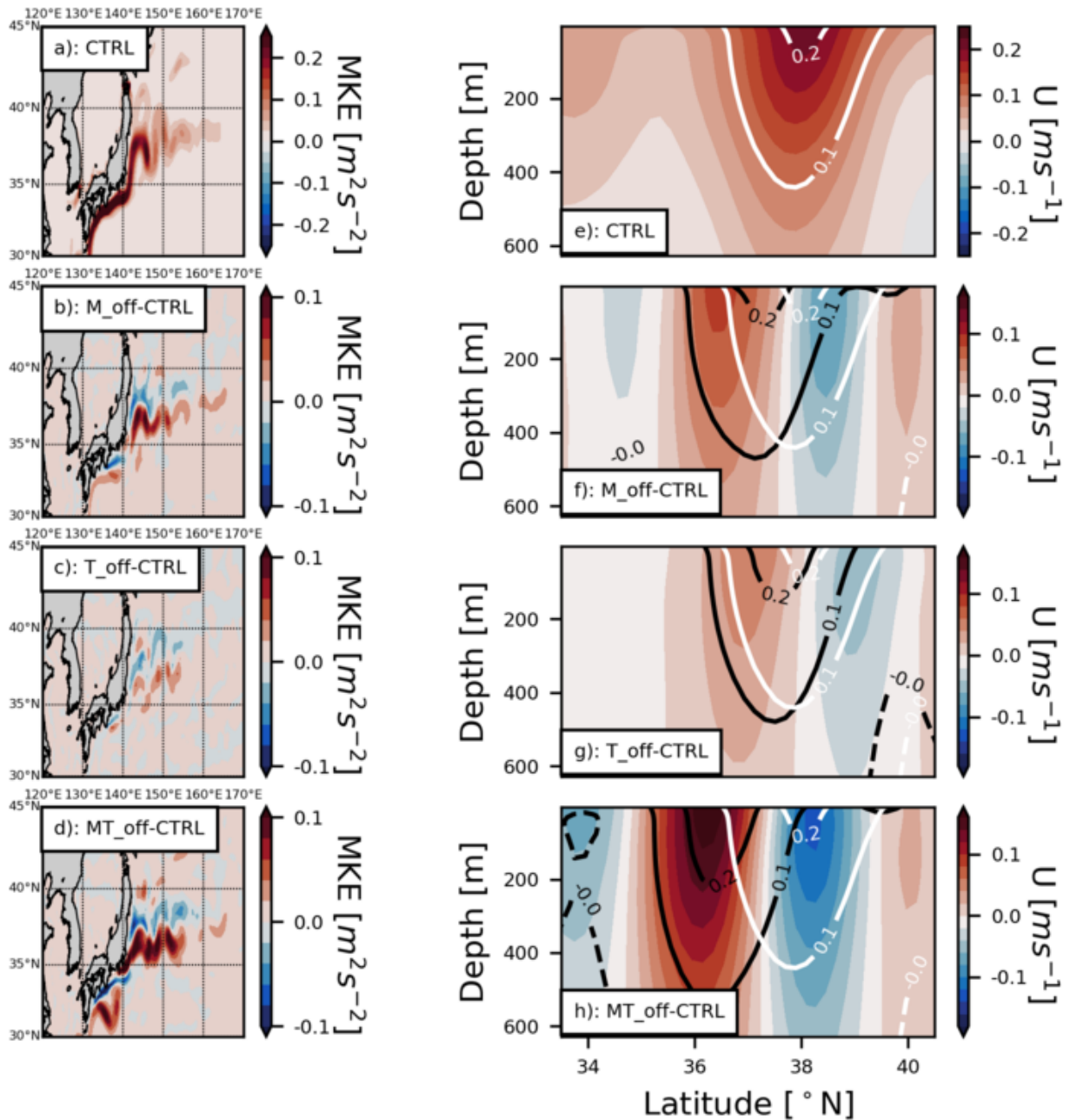
Figure 4.9: as Fig. 4.8, but for Kuroshio region and zonal velocities are averaged from 145°E-160°E.

to 50% in the Gulf Stream Extension for wavelengths less than 200km (Fig. 4.10a,d). For the similar spatial scales we find an increase of up to 30% in the Agulhas region. At larger spatial scales of about 500km for the Kuroshio Extension and the Agulhas increases of 1.6 and 1.5 in KE are found, respectively. The suppression of the thermal damping (T_off) results in considerably smaller changes of about 20%, 15% and 5% for the Kuroshio Extension, Gulf Stream Extension and Agulhas regime, respectively, for scales up to 200km. There are also changes for scales larger than 500km, most prominent in the Kuroshio Extension and Gulf Stream Extension. When both the mesoscale mechanical and thermal damping are suppressed (MT_off), the effects of the individual experiments M_off and T_off both seem to contribute to an enhanced increase (Fig.

4.10c,f,i). In the Kuroshio Extension on scales larger than 500km the increase in KE exceeds 150% and on smaller scales changes up to 100% are found.

In the following section we address the question if coherent eddies are prone to changes in the thermal and mechanical damping. This will be done for the cyclonic and anticylonic eddies shed from the Agulhas regime. There long-lived coherent eddies are regularly found and it is beneficial for this study that after being shed from the Agulhas current they are not in contact with the mean current.
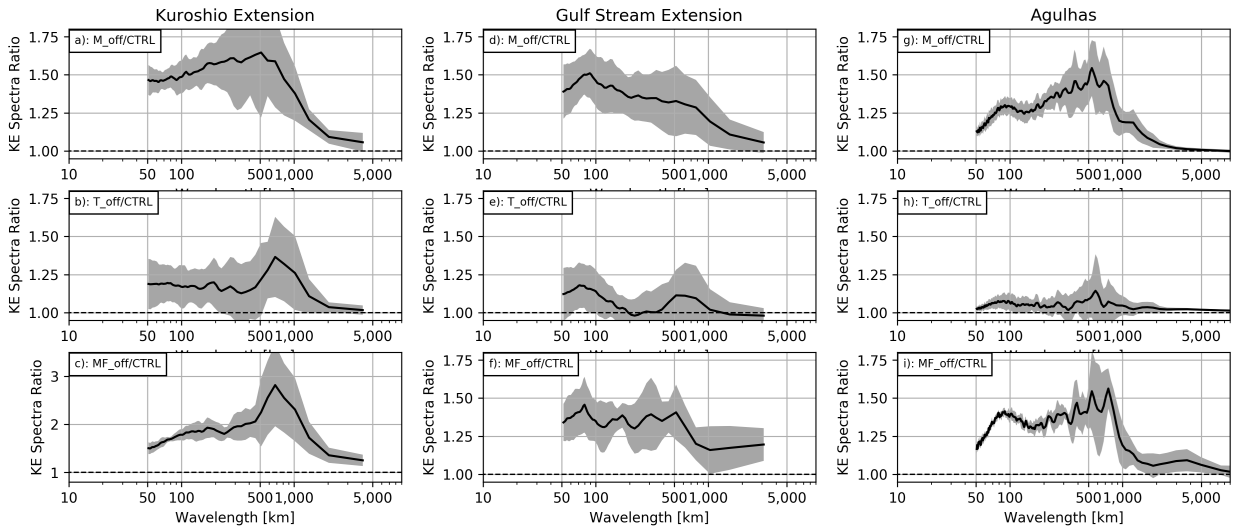
Figure 4.10: Ratio of kinetic energy spectra between (a,d,g) M_off/CTRL, (b,e,h) T_off/CTRL, (c,f,i) MT_off/CTRL for the (left) Kuroshio Extension, (middle) Gulf Stream Extension, and (right) Agulhas, depicting the percentage increase of kinetic energy compared to CTRL by the suppression of mechanical and thermal damping. The shading indicates the standard deviation of KE ratio for individual years from 1990-2004. Ratio of unity is indicated by horizontal dashed line. The Kuroshio region extends from 30°-42°N,145°-165°E, the Gulf Stream region from 35°-42°N,70°-55°W and the Agulhas region from 52°-15°S,0°-75°E. The spectra are 2d wavenumber spectra, are averaged in time and then averaged in x in y direction. Routines kindly provided by Zhao Jing (Ma et al., 2016).

4.3.4 Agulhas Eddies

After looking at the general energetics of the surface ocean the focus of this section is the influence of mechanical and thermal damping on coherent mesoscale vortices or eddies. Mesoscale eddies are characterized by surface elevation/depression, surface temperature anomalies and intense surface currents. The surface temperature anomalies tend to be reflected in THF anomalies while intense surface currents strongly alter wind stress.

In particular in the Agulhas regime strong differences in EKE are found between the experiments (Fig. 4.11). While the thermal damping seems to play a minor role (T_off), the suppression of the mechanical damping results in particular strong difference in EKE of up to 40 cm s^{-1} in the Agulhas retroflection region and over 20 cm s^{-1} associated with eddies shed into the Atlantic. This 'tongue' of high EKE difference M_off minus CTRL is of particular interest as such a pronounced tongue is not in agreement with observations based on SSH (e.g., Renault et al., 2017b). One important detail of the Agulhas regime is the inherent anticyclonic vorticity at the Agulhas retroflection (e.g, Richardson, 2007). When the retroflection gets unstable Agulhas rings (anticyclonic eddies) are shed into the Atlantic. As the EKE within the whole Agulhas regime is more energetic in M_off than in CTRL it is more likely, that the Agulhas retroflection gets more unstable and more and/or stronger Agulhas rings are produced.

We used an eddy tracking algorithm to further investigate this question (see Methods section). As a main reason of the enhanced EKE tongue anticyclonic eddies are identified (Fig. 4.12). Starting from the retroflection there is clear connection of SSH signals from these eddies and the increase in EKE. Cyclonic eddies do not seem to contribute to the increase in EKE. In general the background conditions in the Agulhas regime are in favour for anticyclonic eddies as the background wind curl is also anticyclonic and the wind work over anticyclonic eddies is more positive than for cyclonic eddies (Xu et al., 2016). The mechanical damping is also acting on the vortices and works against the surface motion. Unlike other studies (Frenger et al., 2013; Chelton et al., 2011; Gaube et al., 2015) we are interested in the eddies of longer and shorter lifetimes. Once the eddies are produced and baroclinic instabilities can not fuel the eddy with further energy the second part of the life-cycle is reached and the amplitude declines. Therefore we look at the SSH amplitude of the eddies sorted by age (with 5-day resolution) and sense of rotation (Fig. 4.13). We find that in M_off in general anticyclonic eddies are associated with higher SSH amplitudes and are more abundant (see legend in Fig. 4.13a). Also in the Agulhas regime cyclonic eddies are also more abundant and account for larger SSH amplitudes, but as Fig. 4.12 demonstrates they are not responsible for the EKE 'tongue'.

On a climate scale it is also important how much water is transported from the Indian ocean to the Atlantic (Beal et al., 2011; Biastoch et al., 2015), i.e. the so called Agulhas leakage. Ag-
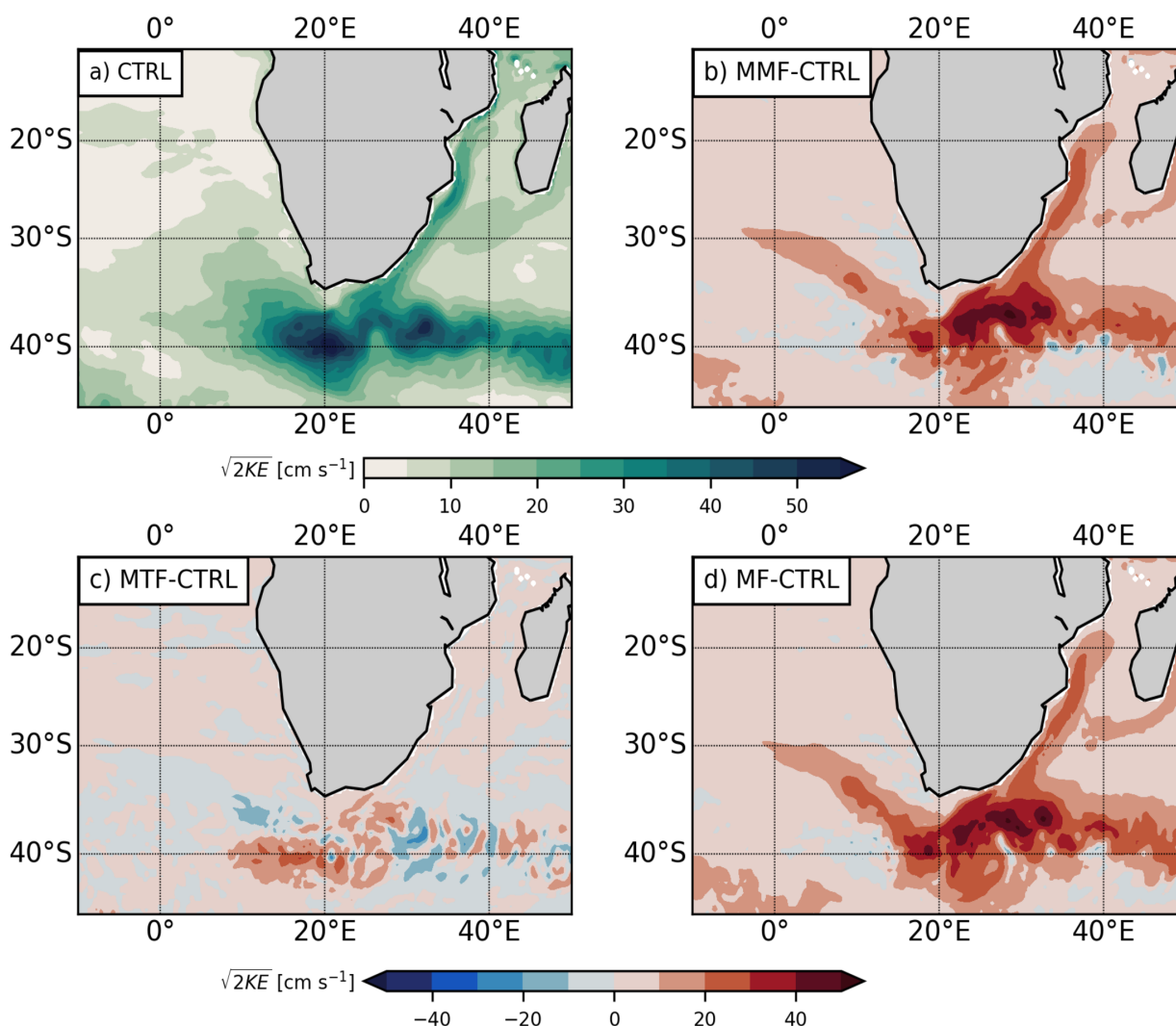
Figure 4.11: Distribution of surface $\sqrt{2EKE}$ [cm s^{-1}] averaged from 1990-2004 in the Agulhas region. Mean for (a) CTRL and differences for (b) M_off minus CTRL, (c) T_off minus CTRL, and (d) MT_off minus CTRL.

ulhas leakage consists mainly of large anticyclonic Agulhas rings (e.g. Gordon, 1986; Goni et al., 1997) in addition to smaller cyclonic eddies (Boebel et al., 2003; Hall and Lutjeharms, 2011), and filaments (Lutjeharms and Cooper, 1996; Treguier et al., 2003). An increase in kinetic energy along the Agulhas ring path (Fig. 4.12) does not necessarily mean an increase in volumetric Agulhas leakage (Le Bars et al., 2012; Loveday et al., 2014). In observations (Dencausse et al., 2010) Agulhas rings do not show such a pronounced path like we found in the M_off experiment. Renault et al. (2017b) showed that in their model set-up, where also a EKE 'tongue' developed, the Agulhas leakage decreased by about 20% when the mechanical damping is turned off (which is similar to the M_off experiment in our study). This finding is supported by simulations where the mechanical damping was also switched off, but with a submesoscale permitting model with 1/20° resolution (F. Schwarzkopf, 2017, personal communication).

To summarize, it was confirmed that in the absence of mechanical damping the entire Agulhas
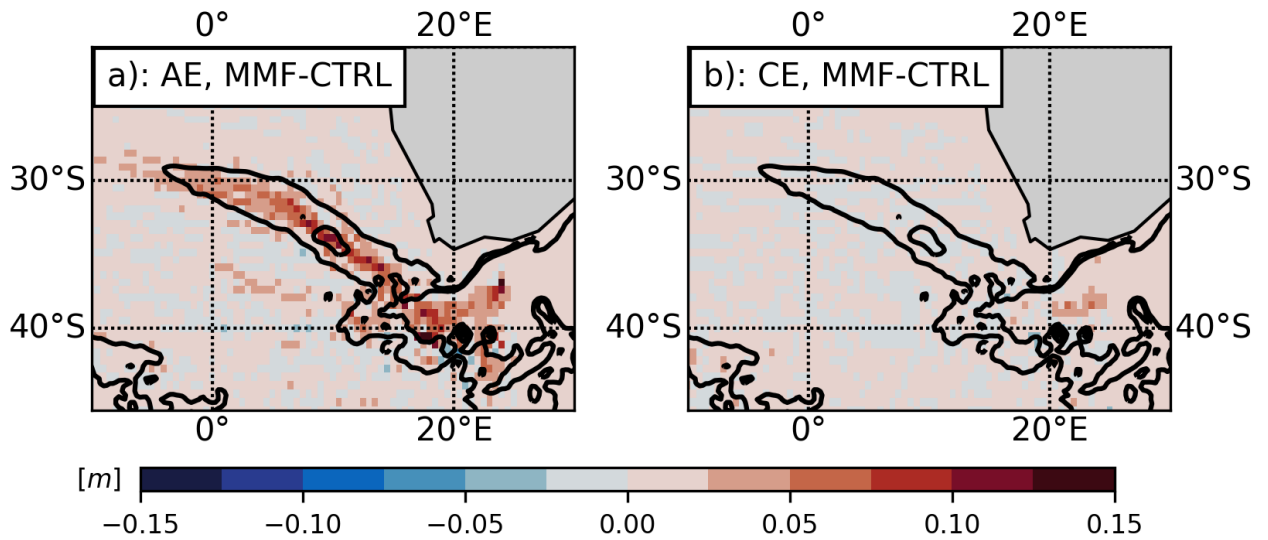
Figure 4.12: Eddy shedding from the Agulhas into the Atlantic. SSH amplitude (color) associated with (a) Anti-cyclonic eddies, AE, and (b) Cyclonic eddies, CE, difference M_off minus CTRL. The amplitude signal associated with AE corresponds well to the difference in EKE found M_off minus CTRL (black contours; CI=10 cm s^{-1}).
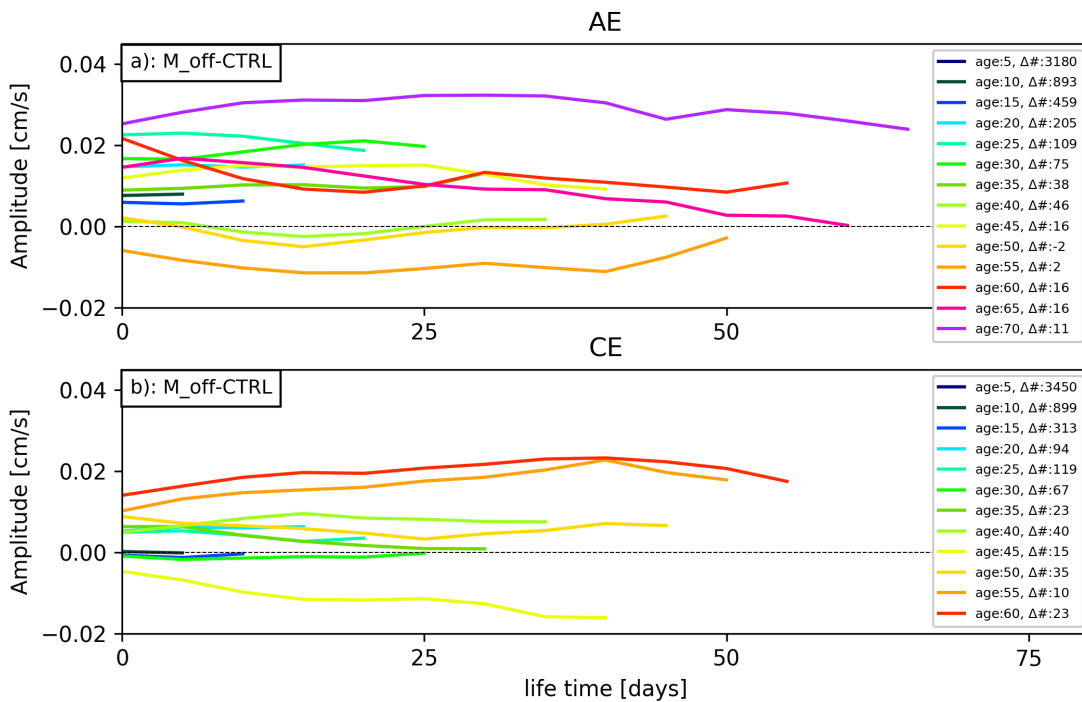
Figure 4.13: Difference in the amplitude M_off minus CTRL associated with (a) Anticyclonic eddies, AE, and (b) Cyclonic eddies, CE, in the Agulhas region (45°-20°S,10°W-30°E). The differences are sorted by eddy lifetime from 5 to 70 days. In the legend the difference in the count ($\Delta\#$) M_off minus CTRL is shown. AE and CE are more abundant in M_off than in CTRL, but the associated amplitude signal is more pronounced for AE.

system energizes. It was demonstrated that one consequence is an unrealistically stable path of anticyclonic eddies shed from the Agulhas retroflection into the the Atlantic.

4.4 Summary & Conclusions

Air-sea fluxes are shaped by ocean surface properties like ocean currents and SST. The air-sea fluxes act to reduce ocean surface currents and gradients in SST and therefore can be seen as a damping for ocean surface currents. These damping mechanisms can be separated into thermal and mechanical contributions, i.e. air-sea fluxes shaped by SST and ocean currents, respectively. For the first time the mechanical and thermal damping are investigated individually and compared to each other using an global eddy-permitting ($1/4°$) ocean-only model. The mechanical and thermal damping mechanisms have been turned off by spatially low-pass filtering the ocean surface currents and SST at the mesoscale before the air-sea fluxes are calculated. As a result strong increases in kinetic energy can be observed. These are particularly prominent in the western boundary current regions.

The mechanical damping accounts for about about 50% kinetic energy increase in the Agulhas region, 30% increase in the Gulf Stream region and 30% in the Agulhas region, where the latter two are in agreement with former studies (Renault et al., 2016b, 2017b). These are not only found at the mesoscale, but also at larger scales up to 1,000 km and are associated with changes in important components of the western boundary currents, like the detachment, pathway and stability of the mean currents. The individual western boundary currents show different reactions to a suppression of the mechanical damping. For example, in the Agulhas system an unrealistically stable path of anticyclonic eddies into the South Atlantic evolves.

The thermal damping effects on the kinetic energy are considerably smaller. For example, in the Kuroshio Extension at small scales the kinetic energy increases by about 20% which is at the lower edge of the findings from Ma et al. (2016). For the Gulf Stream Extension the kinetic energy increases by about 10-15% which is also slightly lower than the Ma et al. (2016) estimate. At larger scales (>500km) their increases are considerably smaller eventually getting negative, while in this study an increase over 25% and 10% are found for the Kuroshio and Gulf Stream Extensions, respectively. When both the mechanical and thermal damping are switched off at the same time, the effects can add up, like in the Gulf Stream where an increase of up to 150% is found at scales between 500 and 1,000km.

These results demonstrate that the thermal and mechanical damping are important components of the western boundary current systems already at eddy-permitting resolution of $1/4°$. It needs to be noted that in this study the damping mechanisms have been deliberately switched off to investigate their impacts. In the next chapter the effects of the damping mechanisms are again discussed from another perspective. It will be shown, that the damping mechanisms are modified if differences in the atmospheric and oceanic grid resolutions in coupled atmosphere-ocean models exist.

5 A note on systematic biases in the ocean due to the air-sea flux calculation in coupled models.

This chapter seeks to raise the awareness for an overlooked problem in the air-sea flux calculation in coupled atmosphere-ocean models. In these models the air-sea fluxes are often calculated on the coarser atmospheric grid. This means that small scale features in the ocean are averaged out and do not modify the air-sea fluxes. But this part of the air-sea fluxes plays an important part for the dynamics of the surface oceans and can lead to strong biases in the air-sea fluxes. As a result the surface kinetic energy increases. Only little changes are found for the mean distribution of temperature.

Contents

5.1 Introduction

The exchange fluxes between atmosphere and ocean play an eminent role in driving ocean dynamics and setting atmospheric conditions. The atmosphere responds to strong gradients in sea surface temperature (SST) as they can be found at ocean fronts and in mesoscale eddies (Chelton et al., 2004; Xie, 2004; Small et al., 2008; Frenger et al., 2013). In coupled global atmosphere-ocean general circulation models (AOGCMs) the fluxes of heat and momentum are typically parameterised by bulk formulae (e.g., Large and Pond, 1981) depending on the difference between ocean and atmospheric properties at the boundary. For instance sensible and latent heat fluxes act to reduce the temperature differences, which typically is expressed as a damping of atmospheric fluctuations toward the SST. However, a realistic response by the atmosphere to mesoscale ocean features can only be achieved with very high spatial resolution in both atmosphere and ocean model components (e.g., Bryan et al., 2010).

In their seminal study, Ma et al. (2016) demonstrated that the same holds for the ocean: air-sea flux variability at the oceanic mesoscale is a key driver of ocean dynamics. They show how kinetic energy in Western Boundary Currents (WBC), such as the Kuroshio and Gulf Stream, decreases when air-sea flux variability is artificially suppressed by decreasing the resolution of the atmospheric fluxes from ∼25 km to 1000 km using a spatial low-pass filter. Ma et al. (2016) point out that due to this filtering effect (in the following called *atmospheric coarse graining*), mesoscale ocean dynamics are not well represented in state-of-the-art AOGCMs. In addition to the thermal damping considered by Ma et al. (2016) there is also a mechanical damping to consider which is associated with the incorporation of ocean surface currents in the wind stress calculation. The mechanical damping reduces the wind work in the presence of ocean currents and therefore kinetic energy (Dewar and Flierl, 1987; Duhaut and Straub, 2006; Zhai and Greatbatch, 2007; Eden and Greatbatch, 2009) and could also be affected by atmospheric coarse graining. In this regard it may be noted that many AOGCMs of the current Climate Model Intercomparison Project phase 6 (CMIP6) implicitly include atmospheric coarse graining by employing atmosphere and ocean model grids differing by factors of 2 to 10 (see Tab. 5.1).

The role of the thermal and mechanical air-sea fluxes for the ocean dynamics is illustrated using a mesoscale eddy. For instance, a warm-core eddy in the North Atlantic has a positive temperature anomaly and anticyclonic surface currents. The turbulent heat loss over this eddy is enhanced compared to the ambient waters due to the enhanced air-sea temperature contrast (Fig. 5.1 left). This reduces the horizontal buoyancy gradient, and thus weakens the available potential energy and the geostrophic surface currents associated with the eddy. In contrast, when the air-sea flux calculation grid does not have sufficient resolution to adequately resolve the surface anomalies this thermal damping is diminished (Fig. 5.1 right). Then buoyancy anomalies remain larger and stronger surface currents are maintained.

Thermal damping for a mesoscale eddy

a) Turbulent heat fluxes

### b) Damping effect

Wind ➡   Ocean current ➡
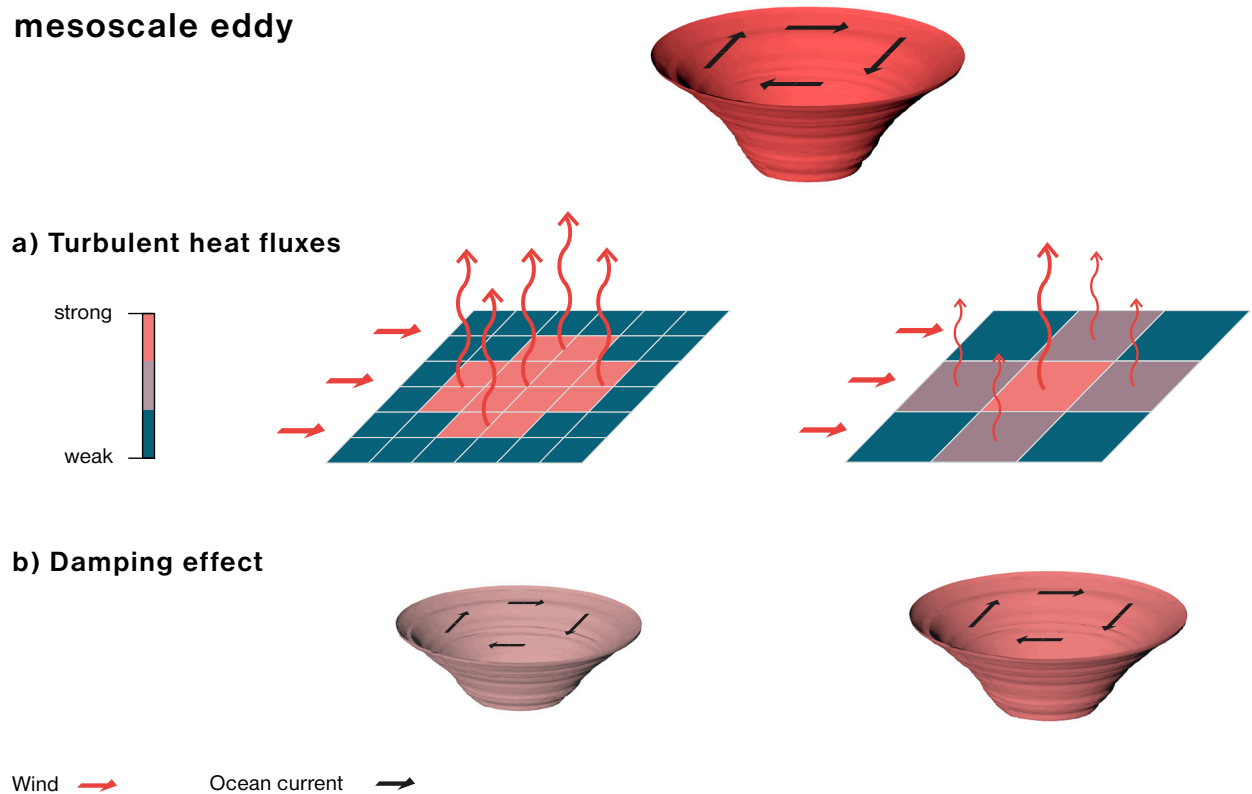
Figure 5.1: Schematic of thermal damping over an eddy. The turbulent heat fluxes (a) have a (b) damping effect on the eddy. With an adequate resolution of the air-sea exchange grid (left) the warm-core eddy loses more heat than surrounding waters, leading to a reduction of the warm anomaly associated with the eddy. As a consequence the intensity of the surface currents is diminished. This thermal damping is reduced when the air-sea exchange grid has a relatively coarse resolution (right). This leads to persistent warm anomalies and enhanced surface currents. The argumentation works analogously for cold-core eddies.

The implications of the atmospheric coarse graining for the wind work can be seen by considering the air-sea momentum flux formulation. In atmosphere-ocean models the wind stress is usually parameterized using a bulk formulation that considers the relative motion between atmosphere ($\mathbf{U}_a$) and ocean ($\mathbf{u}_o$), $\tau_{rel} = \rho_a C_d |\mathbf{U}_a - \mathbf{u}_o|(\mathbf{U}_a - \mathbf{u}_o)$. The work of this "relative wind" stress on the ocean currents is given by, $W_{rel} = \tau_{rel} \cdot \mathbf{u}_o$. The contribution of the ocean currents to the wind work (W_{diff}) can be estimated by the difference in work between relative and "absolute wind" stress, $W_{diff} = W_{rel} - W_{abs}$, where the absolute wind work is calculated using the absolute wind stress, $\tau_{abs} = \rho_a C_d |\mathbf{U}_a|(\mathbf{U}_a)$. The contribution of the ocean currents is always negative and stronger when the winds are aligned with the ocean currents $W_{diff} \approx -\rho_a C_d |\mathbf{U}_a|(|\mathbf{u}_o|^2 + (\mathbf{u}_o \cdot \mathbf{i})^2)$, where $\mathbf{i}$ is a unit vector pointing in the same direction as $\mathbf{U}_a$ (Duhaut and Straub, 2006). Both terms on the right hand side are negative-definite. In headwind conditions W_{diff} is most negative, followed by conditions where the wind and the ocean currents are aligned, and a relatively small effect when the wind is orthogonal to the ocean currents. This is illustrated for an eddy exposed to uniform westerly winds (Fig. 5.2 left). The contribution of the ocean currents to the wind

stress (Fig. 5.2a) is negative if the surface current is directed with the wind and positive when it is against the wind. However, the contribution to the wind work, W_{diff}, is then estimated on the ocean grid and is always negative as pointed out above. This mechanical damping then results in reduced currents and a shrinking of the eddy core. In contrast, when the wind stress is calculated on a coarser, typically the atmospheric grid, the contribution of the ocean currents to the wind stress is diminished as the averaged ocean currents are smaller (Fig. 5.2 right). As a result the contribution of the ocean currents to the wind work is more positive, i.e. the damping ist reduced. Moreover, the eddy with coarse graining forcing maintains stronger surface currents.

Mechanical damping for a mesoscale eddy

a) Current-induced wind stress

b) Current-induced wind work (W$_{diff}$)

c) Damping effect
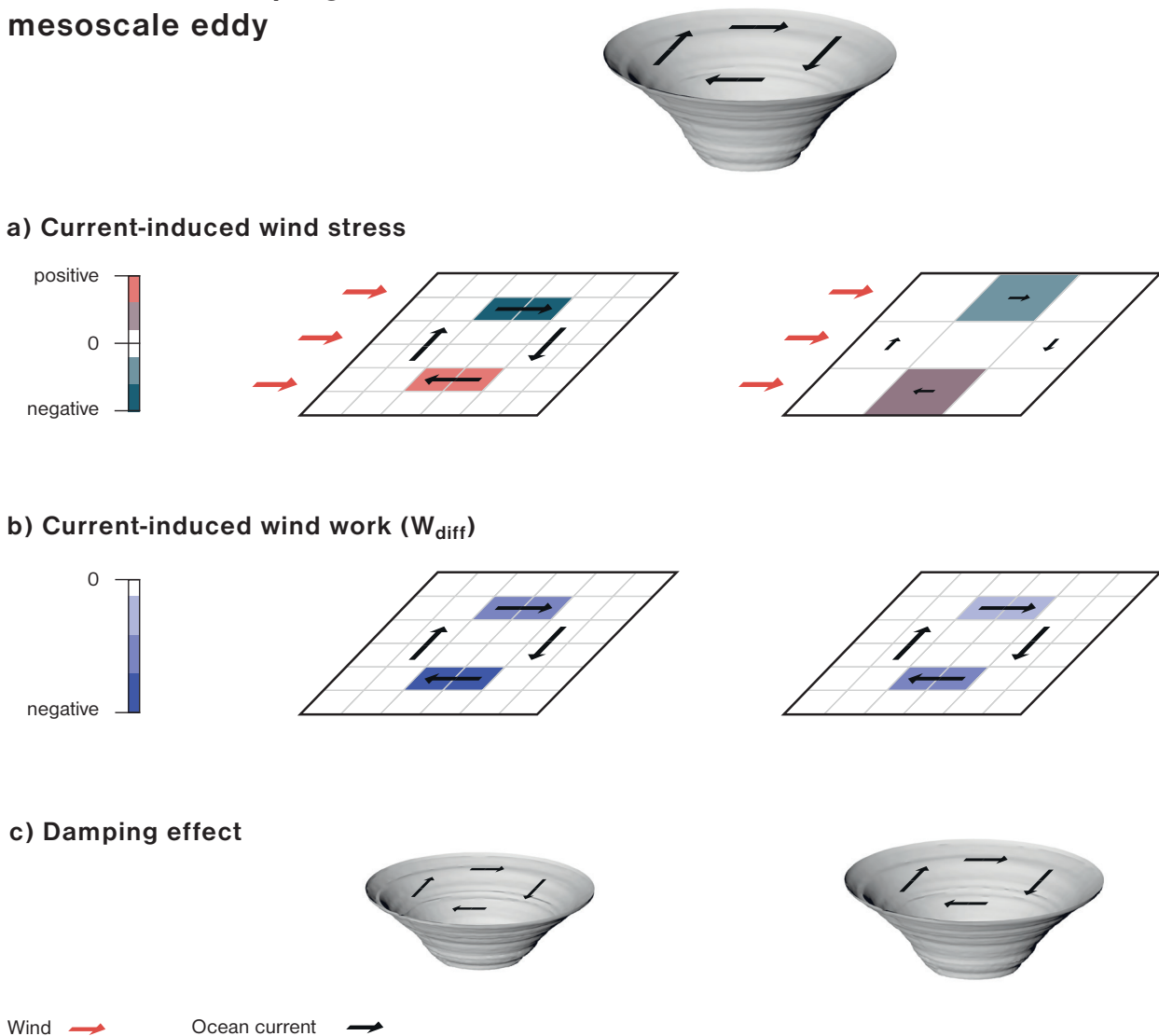
Figure 5.2: Schematic of mechanical damping over an eddy. With an adequate resolution of the air-sea exchange grid (left) the surface currents associated with the eddy modify the wind stress in such a way, that the surface current related wind work is always negative, i.e. damps the surface currents. The mechanical damping is reduced when the air-sea exchange grid has a relatively coarse resolution (right). Then the negative wind work is reduced and stronger surface currents are maintained. The argumentation works analogously for a reversed sense of rotation.

In order to estimate the magnitude of these regional errors and to assess possible systematic impacts on large-scale ocean dynamics and heat content, we use an ocean-only model which enables us to separate the effect of the atmospheric coarse graining from other atmosphere-ocean feedbacks. The approach ensures that the atmospheric forcing conditions are the same in all experiments and not affected by other variations of the coupled system. More information on the flux calculation and the model experiments is provided in Section 2. Results shown in Section 3 focus on the changes in kinetic energy and surface heat fluxes and the impact on ocean temperature distribution and heat transport are discussed. We summarise our conclusions in Section 4.

	Atmosphere	Ocean	Ratio A/O	Air-sea flux calculation grid	Wind stress
BCC-CSM	100	50	2	Ocean	Absolute
AWI-CM-1-0-HR	100	25	4	Atmosphere	Absolute
AWI-CM-1-0-MR	100	25	4	Atmosphere	Absolute
AWI-CM-1-0-LR	250	50	5	Atmosphere	Absolute
CanESM5	500	100	5	Atmosphere	Absolute
CNRM-CM6_HR	100	25	4	Atmosphere	Relative
CNRM-CM6_LR	250	100	2.5	Atmosphere	Relative
GFDL-CM4	100	25	4	Exchange	Relative
GFDL-ESM4	200	100	2	Exchange	Relative
EMAC-2-53	500	250	2	Atmosphere	Relative
MPI-ESM1.2-HR	100	50	2	Atmosphere	Relative
MPI-ESM1.2-LR	200	100	2	Atmosphere	Relative
ICON-ESM	200	50	4	Atmosphere	Relative
HadGEM3-GC31-HH	50	10	5	Atmosphere	Relative
HadGEM3-GC31-HM	50	25	2	Atmosphere	Relative
HadGEM3-GC31-LL	250	100	2.5	Atmosphere	Relative
HadGEM3-GC31-LM	250	25	10	Atmosphere	Relative
HadGEM3-GC31-MM	100	25	4	Atmosphere	Relative

Table 5.1: Exemplary list of present climate models that also contribute to CMIP6 (`http://rawgit.com/WCRP-CMIP/CMIP6_CVs/master/src/CMIP6_source_id.html`, accessed 26.1.2018). The resolutions for atmosphere and ocean are nominal resolutions in km. The ratio A/O quantifies the divergence of atmosphere to ocean resolution. The grids for the air-sea flux calculation differ between the model configuration, but in most cases the atmospheric grid is used. There are also different choices of considering the ocean surface currents in the wind stress calculation (relative winds) or not (absolute winds). All models that have a ratio A/O larger than 1 and calculate the A-O flux on the atmospheric grid may suffer from the coarse graining effect.

5.2 Models and experimental setup

Our experiments are based on the ocean model NEMO (version 3.4) in a global ORCA025 configuration. This configuration uses a tripolar grid at a nominal resolution of longitudinal $1/4°$, and 46 vertical levels with a resolution of 6m near the surface and 250m at depth. Surface-forcing fields build on the Coordinated Ocean-Ice Reference Experiments (CORE, Large and Yeager, 2009; Griffies et al., 2009) and have a spatial resolution of $1.875°$. Turbulent air-sea fluxes are calculated using the bulk formulae given by Large and Yeager (2004) with relative winds. The experiments were started from a 30-yr spinup (1980-2009) and then carried out from 1958 through 2007. A control experiment (CTRL) and coarse graining experiment (CG) were performed. In CG the SST and ocean surface currents were smoothed from $1/4°$ to $1°$, i.e. by averaging over 4x4 ORCA025-grid boxes, before the air-sea fluxes were calculated. The analysis uses the last 10 years of each experiment.

5.3 Effects of Atmospheric Coarse Graining

We will first look at the direct result of coarse grained SST and surface currents in the local air-sea fluxes and for the ocean surface currents, and then examine their repercussions on larger-scale anomalies of hydrographic ocean properties.

When spatial gradients of SST and/or ocean surface currents exist, the coarse graining of these properties results in errors in the air-sea fluxes. An vivid example of the effect of atmospheric coarse graining is shown in Fig. 5.3 for a section of the Gulf Stream in the North Atlantic. Here, a coarsening ratio of 4 is applied, i.e., a smoothing of the SST field from $1/4°$ ($\sim$25km) to $1°$ ($\sim$110km). This smoothing is an order of magnitude smaller than the one considered by Ma et al. (2016) and resembles typical CMIP6 configurations (cf. Tab. 5.1). Even this relatively small ratio is sufficient to significantly smooth the SST gradient across the Gulf Stream of $10°C$ over a few 100 km. For example, the white box marks an area where SSTs of $8°C$ to $18°C$ are simulated by the ocean model but the atmosphere model would be provided with an average temperature of $13°C$. This results in a characteristic dipole pattern, with local heat flux errors of up to $+270$ W/m^2 and -340 W/m^2 (Fig. 5.3). Similar changes can be found in the wind work (not shown).

According to previous studies discussed in the introduction the coarse graining can be expected to act as a spatial low-pass filter, and thus to diminish both the thermal and mechanical damping of surface currents. The mesoscale thermal damping, i.e. dissipation of eddy potential energy, manifests itself in conspicuous dipole patterns with positive and negative SST anomalies as shown in Fig. 5.3. In the case of mechanical damping a surface current always reduces the wind work
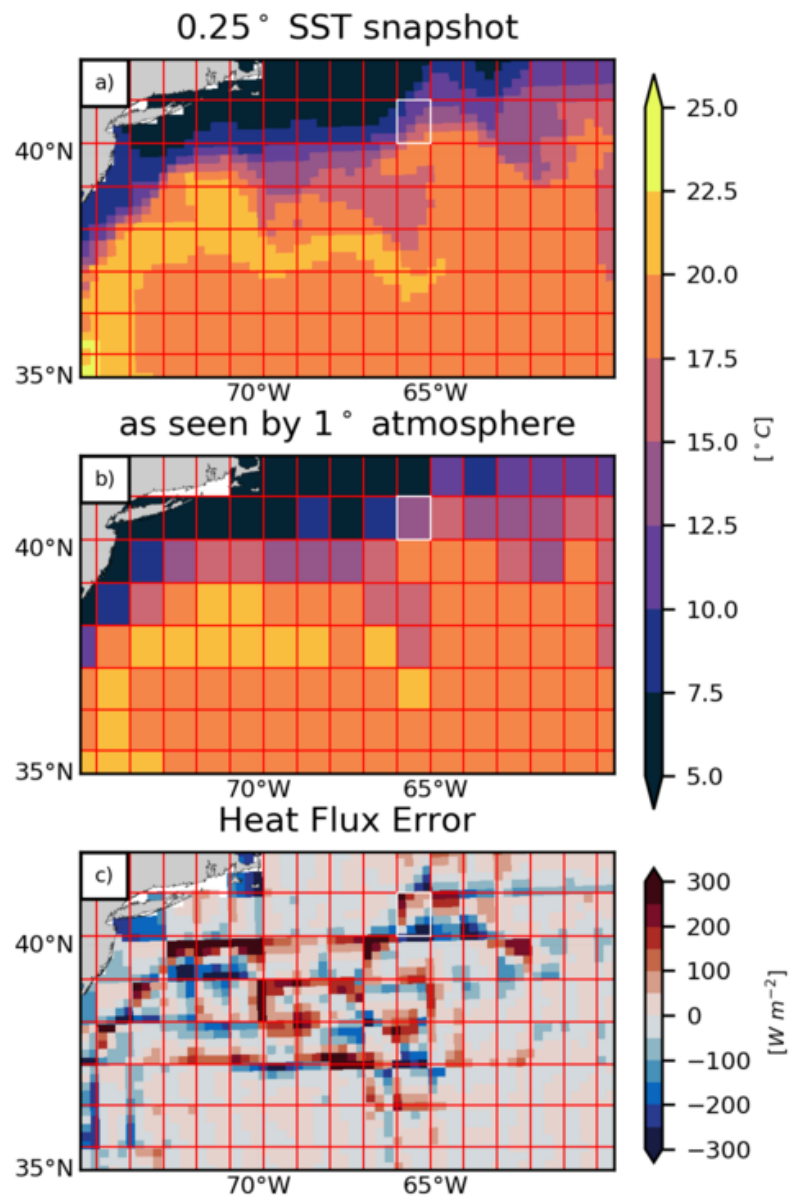
Figure 5.3: Snapshot of SST [°C] in the Gulf Stream Extension region (a) in ORCA025 (1/4°) ocean model and (b) as it would be seen after coarse graining on a 1°-grid. (c) The heat flux error (sensible, latent heat fluxes and longwave radiation) $[Wm^{-2}]$ when calculating the fluxes on the 1°-grid instead on the ORCA025 grid. At sharp SST fronts the coarse graining effect is largest, e.g. in the white box, values between 18 and 8°C are found, but the atmosphere sees about 13°C. This results in heat flux errors of $+270\,Wm^{-2}$ and $-340\,Wm^{-2}$. The heat fluxes shown in this figure are estimated offline using Large et al. (1994) simplified bulk formulations. Red boxes define the coarse atmospheric grid.

(see introduction). In our experiments we observe a global increase in wind work by $+2.0\%$ (60°S-60°N), which is regionally more pronounced such as in the North Atlantic (30°-55°N, 20°-80°W) where the wind work increase is $+3.5\%$ (not shown).

While it is expected that a lack of thermal and mechanical damping leads to stronger surface currents (Seo et al., 2016; Ma et al., 2016; Renault et al., 2016b, 2017b) the magnitude of these

differences caused by a moderate coarsening from $1/4°$ to $1°$ is intriguing. Inspection of global maps for the top 100m (Fig. 5.4) shows that the effect is most pronounced along energetic surface currents such as western boundary currents and their extensions, the equatorial current bands, and the Antarctic Circumpolar Current (ACC). In these regions the bias of the time-mean kinetic energy (here shown as $\sqrt{2KE} = \sqrt{u^2 + v^2}$ [cm s^{-1}]) is well above 30 cm s^{-1} and can locally reach 80 cm s^{-1}. In some cases the changes along the currents appear associated with narrow swaths of decreasing kinetic energy of similar magnitude, hinting at shifts in ocean fronts, such as the Gulf Stream. The changes in eddy kinetic energy are almost always positive, but about one order of magnitude smaller than the changes in mean kinetic energy (not shown). The most pronounced increases in the mean kinetic energy can be found in all WBC, the boundary currents in the North Atlantic and the equatorial regions. Also pronounced decreases in kinetic energy have been noticed in the tropical Indian Ocean, the northern tropical Pacific and Atlantic and close to the WBC. Strong regional increases are found in Gulf Stream Extension, Kuroshio Extension and the Southern Ocean by $+11\%$, $+13\%$ and $+8\%$, respectively. On a global mean the increase is 6%.
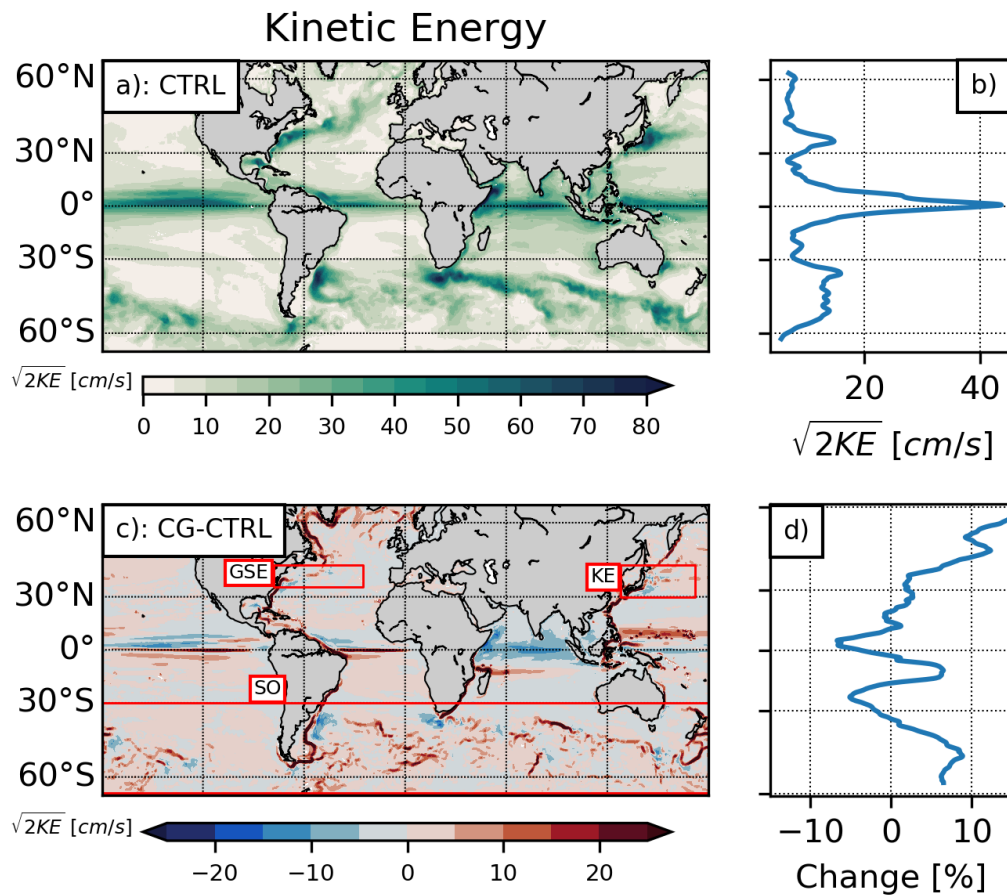
Figure 5.4: Mean kinetic energy for (a) CTRL, (b) CTRL zonally averaged, (c) CG minus CTRL, and (d) zonally averaged difference with respect to CTRL for visual clarity meridionally averaged with a running mean over $10°$. All averages are for the entire simulation and the top 100m.

The effect of the coarse graining on heat fluxes is examined in Fig. 5.5. Averaged over the entire simulation, the coarse graining effect results in differences in the net heat flux exceeding ±20W/m^2, with local maxima and minima of up to $+90$ or -55 W/m^2 over the Gulf Stream, the Kuroshio and the Agulhas currents, as well as the Southern Ocean. Differences on the order of 20 Wm^{-2} are also found in the tropics and subtropics over large areas. For example, in the tropical northeast Pacific the fluxes increase by more than 20 Wm^{-2} while in the tropical southeast Pacific the fluxes decrease by 5 Wm^{-2}. Similar dipole pattern can be found in the subtropical regions but with weaker amplitude. In the WBC more intense but also more localized dipole patterns have been found. On a zonal mean these add up to an enhanced heat loss in the northern hemisphere tropics and the Southern Ocean and an enhanced gain in the southern hemisphere tropics and north of 45°N on the order of $\pm$ 0.25 Wm^{-2} (Fig. 5.5d). On a global mean over the entire integration the change in net heat flux is small $\Delta Q_{net} = 0.02$ Wm^{-2}.
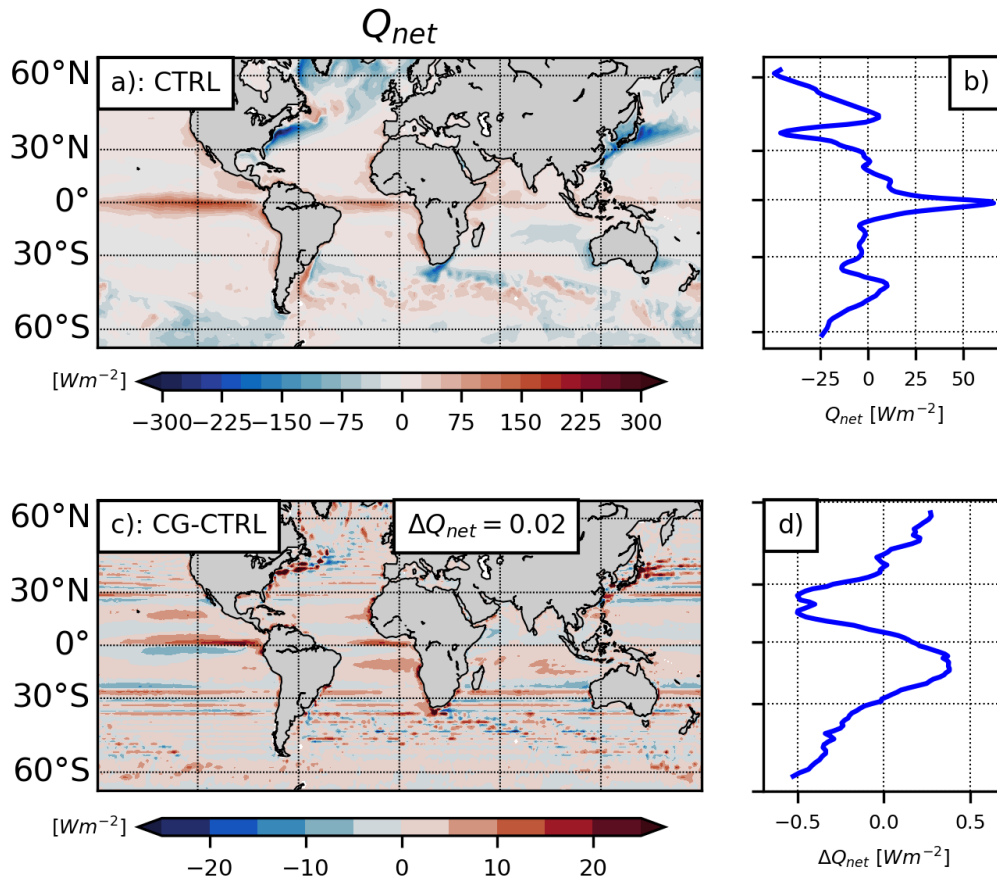
Figure 5.5: Mean net heat flux (Q_{net}) averaged on a 1° grid (a) CTRL, (b) CTRL zonally averaged, and (c) the bias due to the coarse graining, CG minus CTRL, in (d) zonally averaged with a running mean over 20°. The averaging has been done for visual clarity.

The distributions of temperature and salinity are important quantities of the ocean. Usually these distributions are altered by internal variability but also model deficiencies can result in large scale and global drifts of temperature and salinity. Here we address the question whether the

coarse graining effect can contribute to temperature and salinity drifts. The changes in surface heat fluxes and surface kinetic energy reported above have the potential to change deep and intermediate water mass formation and horizontal and vertical heat and salt transport.

Following Treguier et al. (2017) we performed a classic eddy-mean decomposition for the meridional heat transport (the means were estimated for year-long time periods). We find changes in the meridional heat transport in all ocean basins in particular where surface currents differ. However, the changes in either mean or eddy meridional heat transport due to the coarse graining effect are small (always $< \pm 0.03$ PW) compared to the internal variability of the simulations. Also there is no persistence found in the sign of the transport change.

Locally the changes in SST due to the coarse graining effect can be quite large, such as in the WBC regions where these exceed a few °C. However, these are mostly characterized by dipole patterns and on a regional mean these changes are always found to be negligible. Temperature drifts for all ocean basins are sometimes persistent, but are not found to exceed 0.05°C even after 50 years of model integration. These changes are very small compared to temperature drifts found in coupled (Delworth et al., 2012; Griffies et al., 2015; Müller et al., 2018) and forced (Griffies et al., 2009) model simulations where the temperature drifts are found to exceed 0.5°C after 50 years.

5.4 Summary & Conclusions

The ocean model experiments suggest that the local air-sea flux errors in atmosphere-ocean general circulation models (AOGCMs) caused by the calculation of air-sea fluxes on a coarser atmospheric grid rather than the finer oceanic grid can lead to substantial increases in kinetic energy but seem to have an negligible effect on temperature drifts. We investigated this effect in an ocean-only model with $1/4°$ resolution by comparing the air-sea fluxes seen by the $1/4°$-grid with the fluxes obtained by coarsening SST and surface currents on $1°$-grid. This coarsening ratio of 4 is representative for CMIP6 AOGCMs.

We find that this atmospheric coarse graining reduces the amplitude of the thermal air-sea fluxes and wind stress. This is particularly important when sharp fronts exist, like in the western boundary current systems. Globally the kinetic energy increases by 6% and can regionally be changed by 13%. The effects seen here are consistent with the results of Renault et al. (2016b) and Ma et al. (2016) for regional WBC studies. Their results also showed substantial changes in the WBC regime including detachment of the mean jet from the coast and its stability, but have not been investigated here. Long-term integrated effects on water mass properties have found

to be small. The coarse graining effect does not significantly contribute to temperature drifts in any ocean basin — at least for the configuration used here.

While the specific magnitude of these errors is likely model dependent, their presence in general represents a significant uncertainty in AOGCM simulations with greatly diverging grid resolutions. In particular in model inter-comparison studies the coarse graining might be responsible for a non-negligible part of the differences among models having diverging grid resolution ratios or differ in the choice of the air-sea calculation grid. For example the GFDL-CM4 and the HADGEM3-GC31-MM have similar resolutions in atmosphere and ocean, but the former calculates the air-sea fluxes on an exchange grid, while the latter on the atmospheric grid. Even if it is not the topic of this study, Tab. 5.1 also shows differences in the choice of relative or absolute winds in the momentum flux calculation. These differences are certainly also responsible for model-model differences.

Another important ramification of the atmospheric coarse graining concerns the air-sea flux of gases like CO_2 and O_2, where the variability is associated with localised upwelling events and water formation processes at sharp fronts. Preliminary results from a global atmosphere-ocean model demonstrate that the coarse graining effect modifies the global CO_2 uptake by $\pm 4\%$ (pers. comm., Dana Ehlert). Also changes in the ocean circulation have been shown to modify the global CO_2 uptake (Winton et al., 2013).

Apart from using similar atmospheric and oceanic grid resolutions (which is computational extremely demanding), the coarse graining effect could be avoided by either computing the air-sea fluxes on the finer model grid, which is typically the oceanic grid, or on an exchange grid that is formed from the union of grid cell boundaries of both grids (e.g., the exchange grid of GFDL's flexible model system; Delworth et al., 2006). With increasing resolution in the oceanic component of AOGCMs it becomes increasingly important to take the surface currents and SST into account at the oceanic resolution as they play an important role for the eddy air-sea fluxes.

6 Global ocean-sea ice hindcast with an atmospheric mixed layer model

The work presented in all previous chapters leaned on either ocean-only or coupled simulations with complex atmospheric models. Here, an intermediate approach is taken, by coupling an ocean-only model to a simple Atmospheric Mixed Layer (AML) model. The coupling to an interactive AML allows for temperature and humidity adjustment to SST anomalies — an important mechanism that is missing in traditional ocean-sea ice models. It will be shown that this approach can lead to more realistic turbulent heat fluxes and a reduction of large-scale flux biases, without sacrificing the subtle global heat and freshwater balances. A specific focus of the analysis is directed to the question of possible improvements in the representation of the temperature advection feedback associated with the AMOC, a critical feature of the Atlantic circulation not captured in ocean models with prescribed atmospheric conditions.

## Contents

6.1 Introduction

At the air-sea interface turbulent process transfer heat and momentum between ocean and atmosphere. The turbulent heat flux acts to reduce the gradient of temperature between ocean and atmosphere. As the ocean is generally warmer than the near-surface atmosphere and it's heat capacity is much larger, the SSTs exert a strong control on atmospheric temperature and humidity. The sensible and latent heat fluxes drive the oceanic heat loss and can be estimated by mean properties of the near-surface atmosphere and ocean with the commonly used bulk formulations (e.g., Large and Pond, 1981).

A simulation of ocean dynamics with *ocean-only models* commonly involves an atmospheric forcing with prescribed atmospheric conditions. While prescribed winds allow for direct comparison of the ocean model results with observations, the prescription of atmospheric temperature and humidity does not allow for any adjustment to SST anomalies. The practice basically assumes an atmosphere of infinite heat capacity and is in a sense close to a specification of SST (Cayan, 1992). A rough estimation (neglecting horizontal and vertical mixing and advection) shows that the prescription of atmospheric conditions corresponds to an effective restoring time scale for the top 40 m of the ocean of about 30 days (see appendix A). As a result, large biases in the turbulent heat fluxes can occur.

Biases in the turbulent heat fluxes can get exceptionally strong when the current structure of the ocean model deviates from the observed pattern. One prominent example is the Gulf Stream and its extension in the North Atlantic for which ocean models, especially in the case of coarse resolution, commonly fail to realistically capture both the separation from the coast at Cape Hatteras and the re-attachment to the continental slope off Newfoundland. Consequently the North Atlantic Current (NAC) is too zonal without a "Northwest Corner" off Newfoundland (Griffies et al., 2009). This can also be seen in the difference in the mean sea surface height (SSH) between observations and an 0.5°-model (Fig. 6.1a,b). As a consequence of the biases in the current structure large biases in the properties of the surface waters occur (Fig. 6.1c,d). In the North Atlantic Bight the SSTs are too warm by over 6°C and in the central North Atlantic waters are over -6°C too cold. Similarly strong biases occur in the SSS. In a model with prescribed atmospheric temperature such SST biases lead to strong errors in the air-sea temperature gradient. In the case of the Newfoundland Basin the vertical temperature gradient even becomes reversed as the prescribed atmospheric conditions are based on observed SSTs. As a consequence the turbulent air-sea fluxes in this area continuously warm the ocean — a condition that is physical not possible.

A possible way to overcome this coupling issue is the use of a simplified atmospheric model such as an atmospheric mixed layer (AML) model. Seager et al. (1995) suggested a thermodynamically active, but dynamically passive, equilibrium AML model which was used to successfully
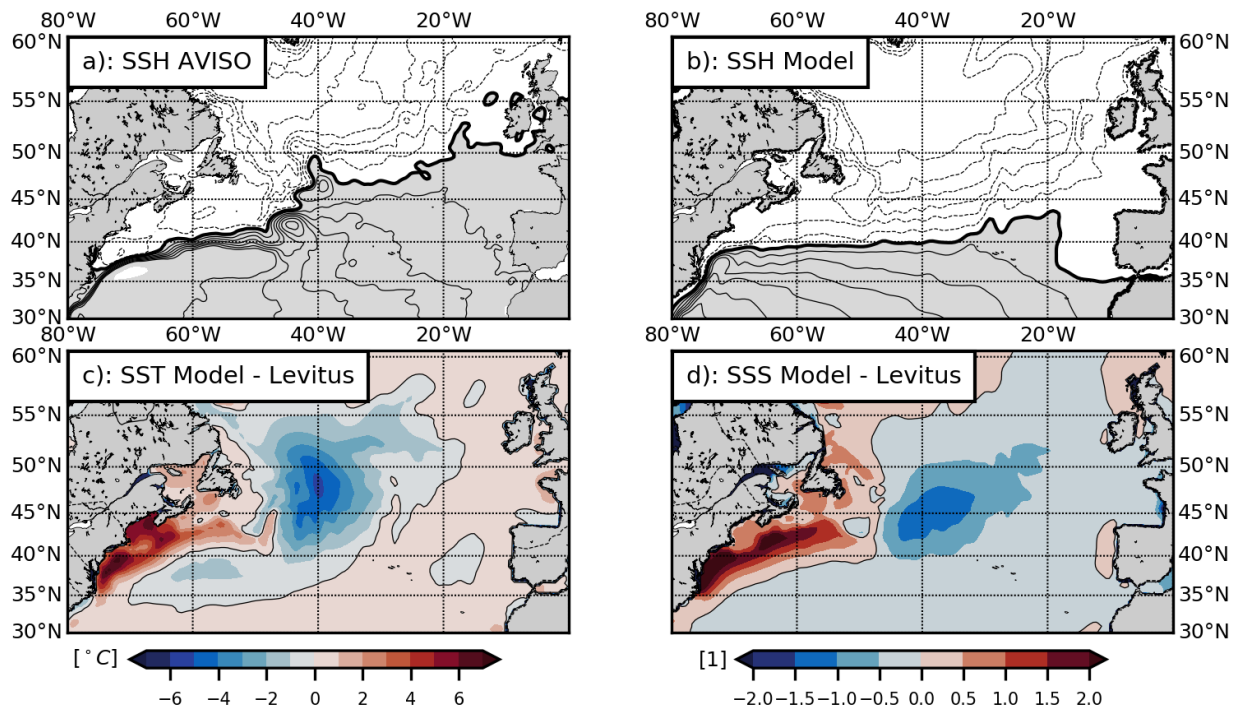
Figure 6.1: North Atlantic model bias. Mean Sea Surface Height (SSH) for (a) AVISO and (b) ocean model (0.5° resolution) with contour interval 10 cm s^{-1}. (c) SST bias and (d) SSS bias with respect to the Levitus et al. (1998) climatology.

provide the air-sea heat forcing in numerous studies, e.g. to investigate the response of NAO-like wind forcing (Visbeck et al., 1998), tropical cyclone wind forcing in the tropical Pacific (Ronghua, 2013), in biogeochemical models of the tropical Pacific (Christian et al., 2002) and Indian Ocean (Wiggert et al., 2006), and is quite recently used to construct a hybrid coupled model with stochastic atmospheric winds in the entire Pacific (Zhang, 2015). Deremble et al. (2013) modernized the idea of Seager et al. (1995) and build an AML model (termed 'CheapAML') that works with bulk formulations, has a more accurate freshwater flux and does not to assume an AML in equilibrium. Parallel computing and no need for a coupler keep the computing overhead as small as a few percent. CheapAML has successfully used to improve the atmospheric forcing in regional model studies of Gulf Stream (Schoonover et al., 2016, 2017), the tropics (Holmes et al., 2018), at the ice-edge or over ice (Horvat et al., 2016) and recently, in a global simplified coupled data assimilation system (Storto et al., 2018).

A particularly important feature of the global climate system is the Atlantic Meridional Overturning Circulation (AMOC) for which the advection of temperature and salinity represents an important feature. The temperature advection feedback acts to stabilize the AMOC as the warm waters lead to a reduction of convection and AMOC strength. A prescription of the atmospheric state suppresses the stabilizing effect on the AMOC as temperature anomalies are damped (Rahmstorf and Willebrand, 1995; Griffies et al., 2009). This leaves the long-term AMOC behaviour

sensitive to the details of the surface heat flux forcing (Moore and Reason, 1993; Power and Kleeman, 1994; Cai and Godfrey, 1995; Seager et al., 1995) and the freshwater forcing (Bryan, 1986; Paiva and Chassignet, 2001; Behrens et al., 2013). Even small freshwater perturbations can lead to strong oscillatory AMOC behaviour and long-term drifts. The typical remedy is to restore the model sea surface salinity (SSS) to climatological conditions and thereby stabilizing the AMOC. A large model inter comparison study demonstrated strong behaviour on the strength of the SSS restoring. Without or weak SSS restoring the AMOC collapsed or resulted in strong inter-decadal oscillations (Griffies et al., 2009). SSS restoring is common practice among ocean-only models and has led to quite realistic AMOC simulations concerning strength and stability. Such restoring on the other hand does suppress natural variability within model simulations and is itself an artificial flux that lacks physical validation. Another possibility that was tested successfully relatively coarse resolution models is the reintroduction of the temperature advection feedback (Rahmstorf and Willebrand, 1995; Lohmann et al., 1996).

This study aims at extending the use of CheapAML to a global ocean-sea ice model simulation on multi-decadal timescales. The prime objective is to investigate the fidelity of this setup in the context of ocean hindcasts. It is tested how strong the global heat and freshwater balances are changed and how this effects the ocean simulation. A particular focus is on the long-term behaviour of the AMOC. With respect to the AMOC it is tested if the temperature advection feedback can be reintroduced in a state-of-the-art ocean model.

In section 2 the ocean model NEMO and the AML model are introduced. In section 3 an global assessment of the hindcast is given. In section 4 the longterm behaviour of the AMOC and the response of the subpolar gyre to AMOC changes are investigated.

6.2 Models and simulations

6.2.1 Ocean Model: NEMO

The ocean model used for this study is based on Nucleus for European Modelling of the Ocean (NEMO version 3.4; Madec, 2011) in the ORCA05 ($0.5°$ nominal horizontal resolution) configuration on a tripolar grid with grid spacing of about 30km in the subpolar North Atlantic. The vertical is resolved in 46 z-levels with 6m at the surface and increasing to about 230 below 2000m. The model is hydrostatic and vertical mixing is parametrized by turbulent kinetic energy (TKE) scheme (Blanke, 1993). Lateral subgrid-scale mixing is parametrized by harmonic diffusivities ($600m^2s^{-1}$) and biharmonic viscosity ($12 \cdot 10^{11}m^4s^{-1}$). Eddies are not explicitly resolved and therefore the GM parametrization (Gent and Mcwilliams, 1990) was employed. The ocean model is coupled to the dynamic-thermodynamic sea-ice model LIM2 (Fichefet and Maqueda, 1997).

Salinity restoring is only applied in the absence of sea ice.

6.2.2 Atmospheric Model: CheapAML

In ocean models the air-sea fluxes can be separated into momentum, heat and freshwater forcing. The focus of this study are the turbulent heat fluxes, i.e. the sensible and latent heat flux. The AML is the component below the free atmosphere and is here considered to be a subcloud layer, i.e. condensation happens above the AML and therefore the latent heat flux does not contribute to the temperature budget. The depth of the AML is typically of O(300-2000m) over open water. In CheapAML (see Fig. 6.2) the wind velocity is prescribed whereas the temperature and humidity are free to develop.
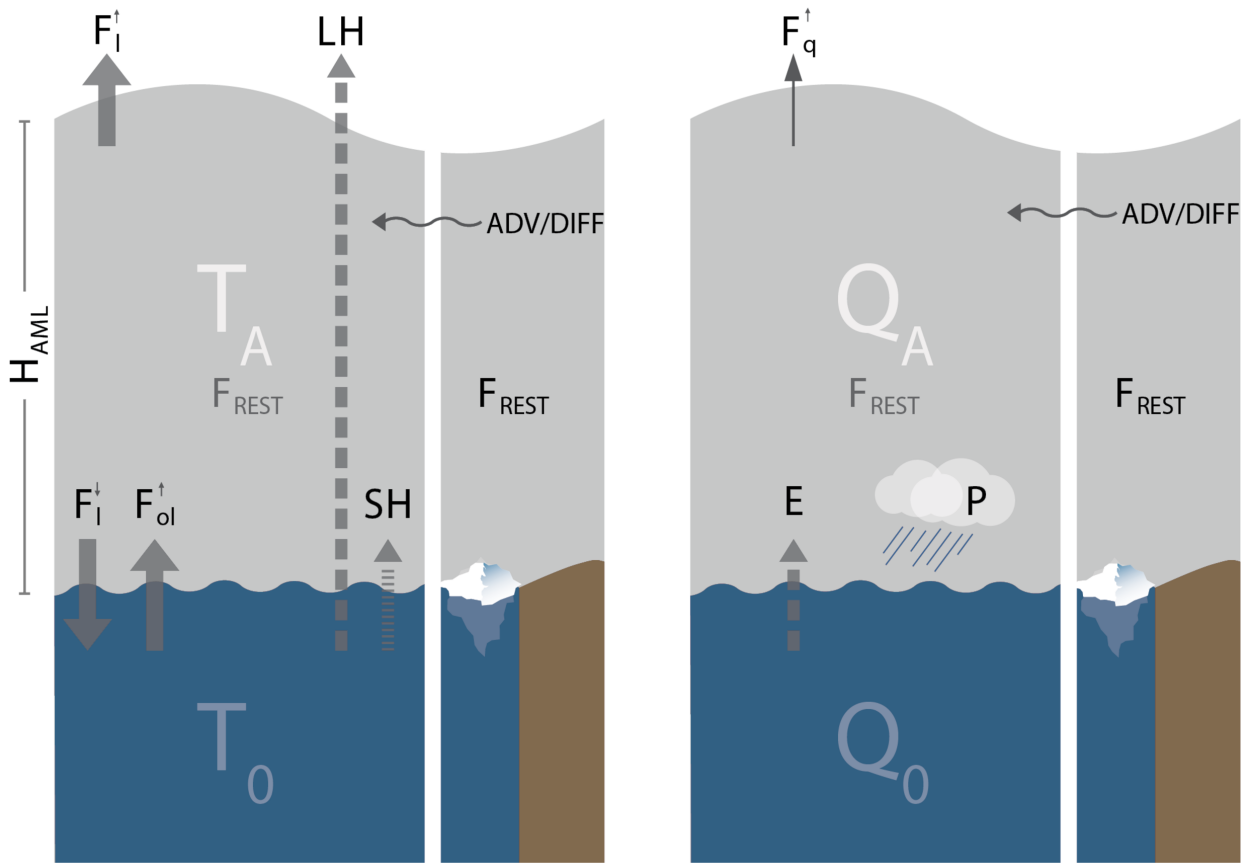
Figure 6.2: CheapAML Fluxes. Horizontal transports are realised by advection and diffusion (ADV/DIFF). **Temperature**: Upward ($F_l^\uparrow$) and downward ($F_l^\downarrow$) longwave flux, outgoing longwave radiation from ocean ($F_{ol}^\uparrow$), sensible (SH) and latent (LH) heat flux, and global mean restoring (F_{REST}). **Humidity**: Evaporation (E), $F_q^\uparrow$ humidity entrainment, precipitation (P) and global mean restoring (F_{REST}). **Land/ice**: Pointwise restoring to climatological values (F_{REST}). Updated version of CheapAML (Deremble et al., 2013).

The temperature T is governed by the following equation:

$$\frac{\partial T}{\partial t} = -u \cdot \nabla T + \nabla \cdot (K_T \nabla T) + \frac{SH + F_{ol}^\uparrow - F_l^\downarrow - F_l^\uparrow}{\rho_a c_p H} \tag{6.1}$$

$$SH = \rho_a c_p C_{dh} |u| (SST - T) \tag{6.2}$$

$$F_{ol}^{\uparrow} = \epsilon \sigma SST^4 \tag{6.3}$$

$$F_l^{\downarrow} = \frac{1}{2} \epsilon \sigma T^4 \tag{6.4}$$

$$F_l^{\uparrow} = \frac{1}{2} \epsilon \sigma T(z_l)^4, \tag{6.5}$$

where SH is sensible heat flux, $F_{ol}^{\uparrow}$ upward longwave radiation emitted by the ocean, $F_l^{\downarrow}$ downward atmospheric longwave radiation, $F_l^{\uparrow}$ upward atmospheric longwave radiation, ϵ emissivity, σ Stefan-Boltzmann constant, c_p specific heat capacity and ρ_a air density. For the radiative fluxes one needs in principle more layers, but it is here parametrized via optical depth and $T(z_l) = T - \Gamma(\gamma \cdot H)$, with the adiabatic lapse rate of $\Gamma = 0.0098 [K/m]$. Note that the latent heat flux does not affect the heat budget as it is defined that condensation happens above the AML. The latent heat flux is defined by the evaporation (Eq. 6.7) times the latent heat of vaporization ($\Gamma_V = 2.5 \cdot 10^6$ J kg^{-1}). The height H of the AML is typically set by strong vertical shear of the winds and could therefore approximately be inferred by a simple Richardson number criterion (Troen and Mahrt, 1986). This, however, would require knowledge of the vertical profile of winds, temperature and humidity. Therefore in CheapAML the boundary layer height H needs to be prescribed. For this study a constant value of 800m is used.

The humidity (Q_a) budget for CheapAML is given by:

$$\frac{\partial q}{\partial t} = -u \cdot \nabla q + \nabla \cdot (K_q \nabla q) + \frac{E - F_q^{\uparrow} - \lambda P}{\rho_a H} \tag{6.6}$$

$$E = C_{de} |u| (q_s^{SST} - Q_a) \tag{6.7}$$

$$F_q^{\uparrow} = \mu \rho_a C_{de} |u| Q_a \tag{6.8}$$

$$P = \rho_a H \tau^{-1} (Q_a - 0.7 q_s^{SST}) \frac{w}{w_0}, \tag{6.9}$$

where evaporation E is calculated with a bulk formula, $F_q^{\uparrow}$ the entrainment at the top of the boundary layer with exchange coefficient μ and large scale precipitation time scale $\tau^{-1} =$ 3.6h. Precipitation occurs when a certain humidity threshold is passed and vertical wind w exceeds reference vertical wind w_0. Note that the surface humidity is a function of SST.

Over land and fully covered sea-ice regions the vertical fluxes are not defined in CheapAML. But at the coastlines winds redistribute temperature and humidity. Thus in order to close the heat and freshwater budget restoring to prescribed conditions is necessary over land and sea-ice. Additionally over the ocean a global mean restoring was implemented with a time scale of 2 hours. For unresolved processes a diffusion of the strength $K_T = K_q = 5 \cdot 10^4$ is added. The parameters

for humidity entrainment ($\mu = 0.24$) and for radiation height ($\gamma = 0.25$) where chosen to have a minimal drift for both temperature and humidity with respect to the global values given by Large and Yeager (2009). For more details see appendix B. The contribution of rain to the AML budget was set to $\lambda = 0.1$.

6.2.3 Forcing strategy & experiments

The effect of replacing the prescribed atmospheric temperature T_A and humidity Q_A simulated by CheapAML was examined in a set of hindcast experiments with ORCA05. The experiments we reinitialized by December values of the Levitus et al. (1998) climatology. Forcing follows the CORE2 procedure (Large and Yeager, 2009; Griffies et al., 2009) with 6 hourly data for shortwave, longwave radiation, precipitation, temperature, humidity. River runoff was provided with monthly resolution. The turbulent fluxes (sensible , latent heat and evaporation) were estimated via bulk formulations (Large and Yeager, 2004). A 30-year (1978-2007) spinup was followed by 50-year (1958-2007) experiments. Surface freshwater fluxes are applied as volume fluxes.

Two pairs of experiments with prescribed vs. CheapAML temperature and humidity were performed: one with a standard choice of the SSS restoring configuration used in present global ocean models (a piston velocity of 193.5 mm day^{-1}, corresponding to a relaxation time for a 50m-surface layer of 258 days), and a second one without restoring in order to test the sensitivity of the model performance on a global scale and in particular for the representation of the AMOC (Tab. 6.1). Please note that in the AML experiments only the sensible and latent heat flux differ from the other experiments.

Experiment	Salinity restoring [mm day^{-1}]	Atmospheric temperature & humidity
P_{STRONG}	193.5	Prescribed
P_{NO}	0	Prescribed
AML_{STRONG}	193.5	AML
AML_{NO}	0	AML

Table 6.1: List of experiments. Two parameters are varied: the piston velocity [mm day^{-1}] and temperature and humidity are either prescribed (P) or calculated with CheapAML (AML). In the cases of AML only sensible and latent heat flux are calculated with the new temperatures and humidities while evaporation is calculated with prescribed values.

The strength of SSS restoring is given as a piston velocity:

$$F_{rest} = V_{piston} \frac{SSS_{model} - SSS_{ref}}{SSS_{model}} \tag{6.10}$$

The damping time-scale (T_{rest}) for given layer thickness (h) is given by

$$T_{rest} = \frac{h}{V_{piston}}. \tag{6.11}$$

6.3 Hindcast assessment

In a global context prescribed atmospheric temperatures and humidities provide constraints to an ocean model. Therefore in the following it is investigated how a global model behaves when these constraints are released. Deremble et al. (2013) already assessed the performance of CheapAML in a regional ocean experiment for a few months and in a global experiment with prescribed SST. In this study the focus of the assessment is on the long-term changes in the ocean that arise from the turbulent heat fluxes provided by CheapAML.

6.3.1 Atmospheric temperature and humidity

In CheapAML temperature and humidity within the AML are governed by a subtle balance between incoming and outgoing fluxes. They are to leading order a function of SST, but can locally be altered by advection, in particular at the coast where typically cold continental air masses are advected in winter. First it will be examined how the atmospheric temperature in CheapAML changes with respect to the prescribed temperature from the CORE forcing. The atmospheric temperature and humidity adjust fast to the SST in the ocean model. Regionally the changes to the prescribed conditions can exceed $\pm$ 4°C or $\pm$ 3 g kg^{-1} (Fig. 6.3). Strong cooling is found in the tropical East Pacific and North Atlantic as well as the summer hemisphere. Warming can be found in the tropical Indic, the subtropical Atlantic and Pacific with particularly strong warming over WBC. The changes are modulated by the seasonal cycle with the summer hemisphere being warmer. In the tropics where the seasonal cycle is not as pronounced than in higher latitudes the SST changes are quite persistent (not shown). Also the global mean change shows a seasonal cycle reflecting the with the northern hemisphere being up to -0.06°C cooler in winter and +0.04°C warmer in summer. The global mean change averaged over the first 10 years small with about -0.002 °C. The pattern are very similar for humidity changes.
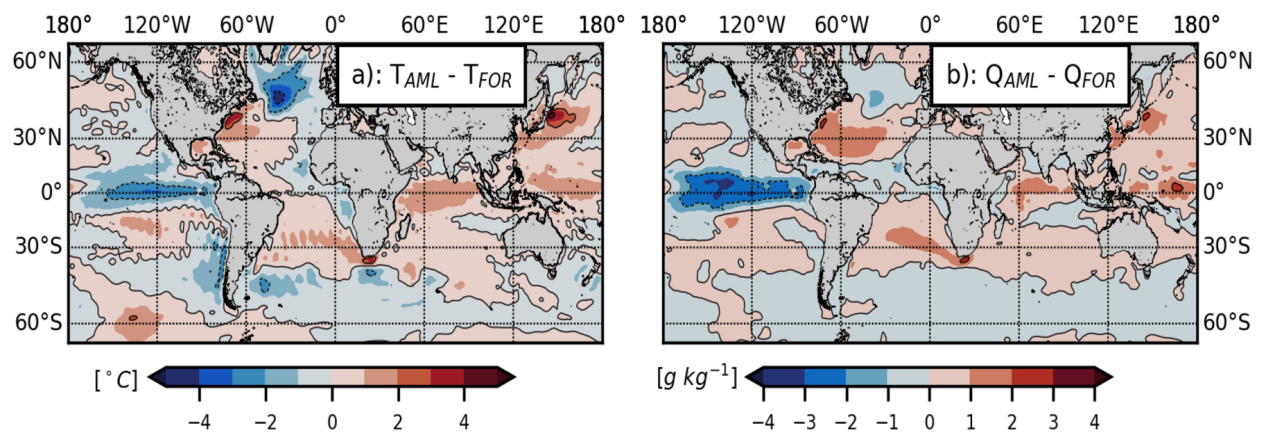
Figure 6.3: Difference between the (a) atmospheric temperature T [°C] and (b) atmospheric humidity [g kg^{-1}] calculated in the AML model and the prescribed forcing averaged over the first 10 years. Contour interval is 2.

The answer to the question, why the atmospheric temperature and humidity regionally change by such large amounts is simple: They adapt to the underlying SST. In most regions the surface ocean gains energy by solar radiation which is then released to the atmosphere as sensible heat or moisture and ultimately lost by longwave radiation to space. This is reflected by an oceanic temperature that is typically (here shown for reanalysis products, Dee et al., 2011; Yu et al., 2008) warmer than the atmosphere by about 1°C and even up to 4°C over the Gulf Stream, Kuroshio or Agulhas retroflection (Fig. 6.4a,b). Colder oceanic than atmospheric temperatures are found in the northeastern Pacific, the eastern tropical Pacific, the tropical Atlantic and in particular the Southern Ocean where upwelling of cold waters or advection of warm air masses lead to these exceptions. Taking the reanalysis products as a reference, in a standard ocean-only configuration some regions appear too cold in the North Atlantic, North Pacific, the tropical east Pacific and the Southern Ocean where the difference between SST and atmospheric temperature can exceed -4 °C (Fig. 6.4c). On the other hand there are some parts in the tropics and subtropics where the difference between SST and atmospheric temperature is too positive by about 1°C. When the ocean-only model is coupled to the AML-model the difference between SST and atmospheric temperature gets closer to differences found in the reanalysis products (Fig. 6.4d). The largest improvements are found in the northeastern Pacific, the Southern Ocean, the subtropics, tropics and in particular in the North Atlantic. Some regions appear to have a too positive difference between SST and atmospheric temperature like the eastern subtropical and tropical Pacific and Atlantic.

A few more words on the adaptation of the atmospheric temperature and humidity to the underlying SST: the heat capacity of air is so small with respect to the heat capacity of water that the sensible and latent heat flux result in relatively fast adjustment of the too warm and moist air. This brings the system back to a state where the sensible and latent heat flux are directed from the ocean to the atmosphere, i.e. a heat loss for the ocean. Exceptions are only possible in regions with upwelling of cold water masses or advection of warm air masses. Details of the local and global AML heat and freshwater budget are given in appendix C.

The change in the temperature difference between atmosphere and ocean has consequences for the sensible heat flux. Concurrent changes in humidity modify the latent heat flux. But first look at P_{NO} where large areas of negative sensible heat flux in the North Atlantic, tropical east Pacific and Malvinas confluence zone are found that reflect the negative SST - T_A seen earlier (Fig. 6.5a). Note that negative sensible heat flux can occur, but over such large areas it is physically not possible. Elsewhere it is not obvious if the turbulent heat fluxes are unrealistically strong or weak. The differences in the heat flux of P_{NO} with respect to AML_{NO} does reflect that there might have been such unrealistic situations. As for the changes in temperature differences large changes in the turbulent heat fluxes are found (Fig. 6.5c,d). For the sensible heat flux the negative fluxes seen before in the North Atlantic, tropical east Pacific and Malvinas confluence zone increase
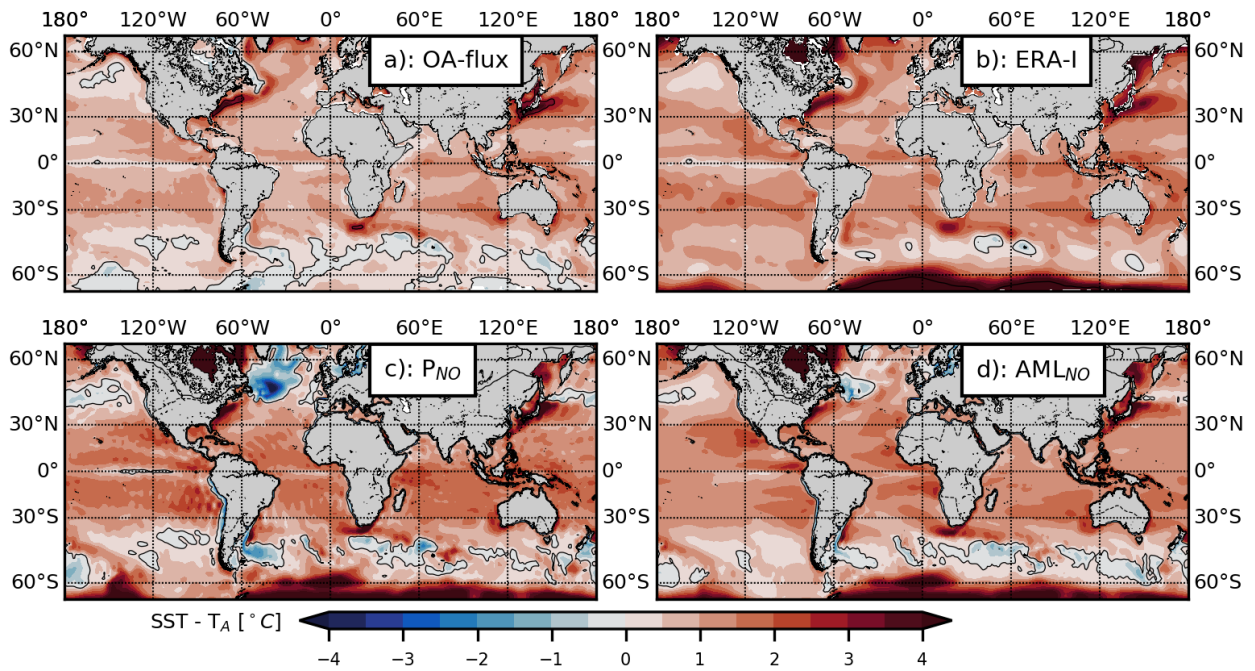
Figure 6.4: SST minus T_A for reanalysis models (a) OA-flux, (b) ERA-Interim and for the ocean-only simulations (c) P_{NO} and (d) AML_{NO}. Black contours highlight the zero line. The reanalysis models serve as a reference as they reflect the natural difference between SST and T_A — that is, the ocean is warmer. Overall, AML_{NO} reproduces the pattern of the reanalysis models better than P_{NO}.

by more than 20 Wm^{-2}. Also south of the Agulhas retroflection and the southeastern Pacific the sensible heat flux increases by more than 10 Wm^{-2}. Over the Agulhas, the Gulf Stream and Kuroshio the sensible heat flux gets smaller by more than 20 Wm^{-2}. Quite similar patterns are found for the changes in the latent heat flux with a similar or sometimes larger magnitude. For example, in the tropical Pacific the latent heat fluxes increases by over 50 Wm^{-2} over a large area.

6.3.2 Ocean heat and freshwater budget

In order to minimize artificial model drift the heat and freshwater budgets need to be balanced. Observational estimates suggest that global heat budget is nearly closed with only about $+1.3$ Wm^{-2} imbalance (Trenberth et al., 2009). The global energy balance is an important quantity of our climate conditions. The same is true for ocean-only models where it is in particular difficult to close heat and freshwater budgets. In Tab. 6.2 the individual fluxes of the heat budget are listed and compared to a variety of estimates based on climate models (Wild et al., 2015), observations (Trenberth et al., 2009) and for the CORE forcing (Large and Yeager, 2009). At global scale the experiments P_{STRONG} and AML_{NO} show only marginal differences, but when compared to recent estimates based on CMIP5 models (Wild et al., 2015) solar radiation is of about 4.5 Wm^{-2} smaller, thermal radiation 2 Wm^{-2} smaller, latent heat flux 6 Wm^{-2} larger and sensible heat flux 2 Wm^{-2} larger (note that the differences are similar to the difference found
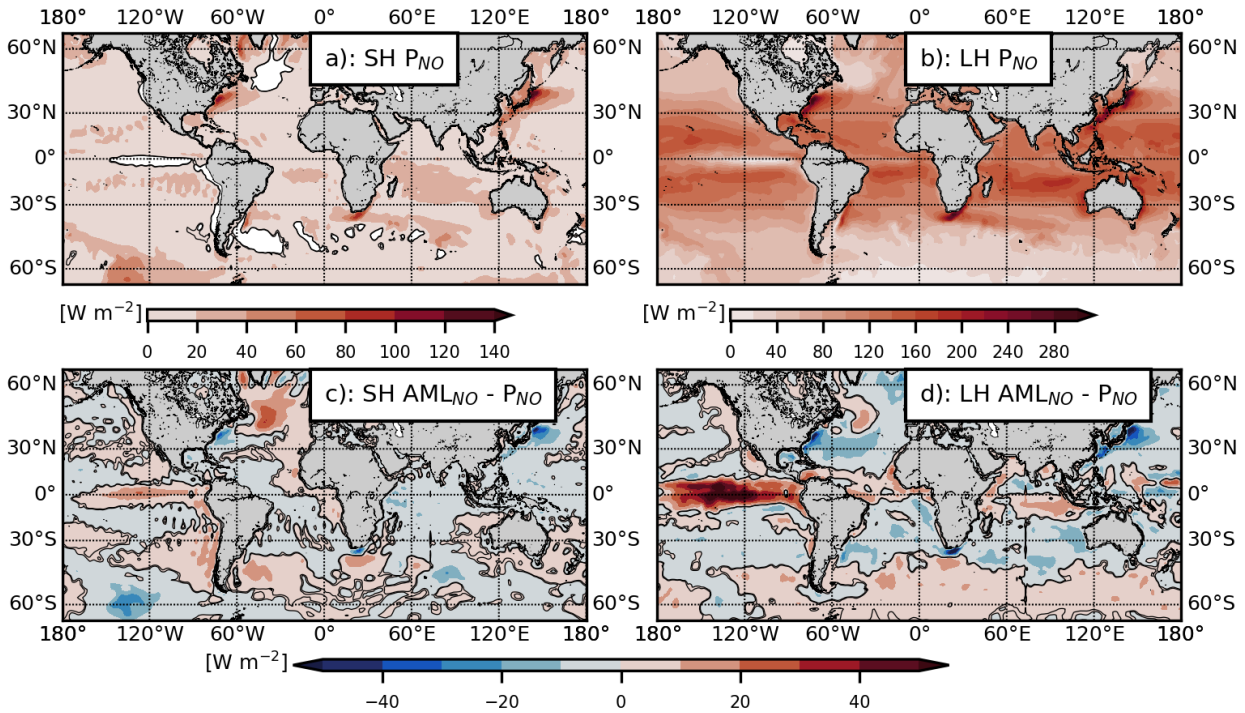
Figure 6.5: Mean sensible (SH) and latent (LH) heat fluxes [Wm^{-2}] for the experiment P$_{NO}$ (a,b) and differences to the experiment AML$_{NO}$ for the first ten years of the integration.

in CMIP5 models; Wild et al. (2015)). The global imbalances are +1.4 and +1.7 Wm^{-2} for P$_{STRONG}$ and AML$_{STRONG}$, respectively. The forcing dataset used for the experiments in this study involves an global imbalance of 2 Wm^{-2} in conjunction with observed climatological SST for the period 1984-2006 (Large and Yeager, 2009). Based on the small global temperature and humidity differences between the AML experiment and the forcing dataset it was expected that also the global imbalance is rather small.

Component	P$_{STRONG}$	AML$_{STRONG}$	Wild et al. (2015)	Trenberth et al. (2009)	Large and Yeager (2009)
Solar	165.6	165.6	170	167.8	165
Thermal	-55.4	-55.5	-53	-57.4	-53
Latent heat	-94.1	-93.9	-100	-97.1	-96
Sensible heat	-14.0	-13.8	-16	-12	-14
Imbalance	1.4	1.7	1	1.3	2

Table 6.2: Heat budget [Wm^{-2}] over the ocean from 2000-2005 for the experiments P$_{STRONG}$ and AML$_{STRONG}$, compared to Wild et al. (2015) and Trenberth et al. (2009) estimates. Note that the Large and Yeager (2009) estimate covers the period 1984-2006. Positive (negative) quantities warm (cool) the ocean. The imbalance is calculated by summing the individual components.

Please note that the heat budget estimation misses a heat flux that is associated with the mass flux (freshwater) across the ocean-atmosphere boundary. It basically takes into account that the freshwater also has a temperature and therefore any freshwater flux results in a heat

flux. Following Griffies et al. (2014) the flux can be estimated:

$$Q_{advect}^{heat} \sim Q_m c_p^0 T_{SST},$$ (6.12)

where c_p^0 is the ocean heat capacity, Q_m mass transport across the surface and T_{SST} sea surface in situ temperature. For the experiments used in this study this advective flux is small $O(+0.2$ Wm$^{-2})$ estimated offline based on monthly values.

The freshwater budget in an ocean-only model generally consists of four components: evaporation, precipitation, river runoff and SSS damping, i.e. a restoring flux of sea surface salinity towards observed climatological values. By far the largest components are evaporation and precipitation and nearly balance each other on a global mean with about -3.36 and 3.29 mm day^{-1}, respectively. The river runoff is contributing with about 0.31 mm day^{-1}. In the experiment P$_{STRONG}$ the SSS damping is 0.06 mm day^{-1} which leads to a global mean freshwater flux of -0.04 mm day^{-1}. In the AML experiments the freshwater fluxes are not modified directly, but the change in sensible and latent heat flux modify the SST which in turn modifies the evaporation. As a consequence the global mean in AML$_{STRONG}$ changed to -0.06 mm day^{-1}. Locally, the SSS damping results in large SSS gain in the North Atlantic — an important feature for the stabilization of the AMOC (Behrens et al., 2013). In P$_{NO}$ and AML$_{NO}$ the SSS damping is turned off, and the global mean freshwater flux is -0.11 mm day^{-1}.

Even if the global change in the freshwater budget is small regionally it can lead to quite significant freshwater gains or losses. For example, in the subtropics excess evaporation leads to large SSS values (Fig. 6.6). An increase in SST in the subtropical North Atlantic results in an increase in the total freshwater flux by about 1 mm day^{-1} in AML$_{NO}$. Also over the Gulf Stream and the Kuroshio and their extensions large increases in the surface freshwater flux are found. Particular for the North Atlantic such strong changes are interesting, as such SSS signals may get transported into the deepwater formation regions. On the other hand there is also a region with strong freshwater gain in the northeastern Atlantic due to relatively cold SSTs.
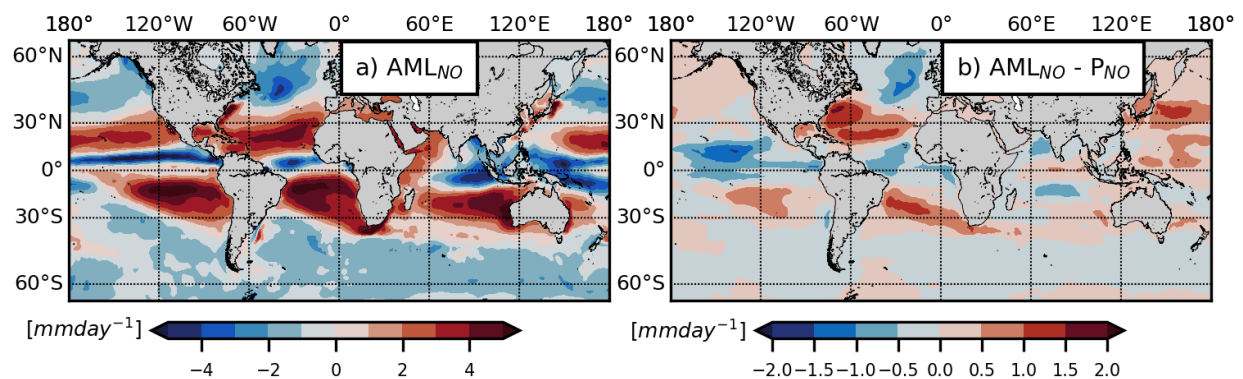
Figure 6.6: Surface freshwater flux [mm day^{-1}C] for the years 1995-2004 for (a) AML$_{NO}$ and (b) AML$_{NO}$ - P$_{NO}$.

6.3.3 Ocean temperature and salinity

It is instructive to examine the temperature and salinity deviations from observations Levitus et al. (1998) as an integrative view of the surface forcing. Some of the SST biases found here are common among ocean models with similar resolution (Griffies et al., 2009). The largest biases are found in regions with strong SST gradients such as the WBC, the ACC and upwelling regions (Fig. 6.7). For the North Atlantic and North Pacific biases in the current structures such as a too late separation from the coast lead to strong warm biases at the continents. In the North Atlantic a spuriously southward NAC and a missing "Northwest Corner" near Newfoundland lead to a prominent cold bias there. At the west coasts of the African and American continents warm biases are found, that are probably due to misrepresentation of the coastal upwelling or errors in coastal winds. The simulation AML_{STRONG} shows a similar pattern as P_{STRONG}, but the amplitude of the SST biases are larger. A possible explanation for this is that the biases arise from deficiencies in the ocean model and not in the atmospheric forcing in particular the turbulent heat fluxes. Then, in AML_{STRONG}, when the atmospheric temperature and humidity are free to evolve the turbulent heat fluxes do not restore the SST and biases become more prominent.
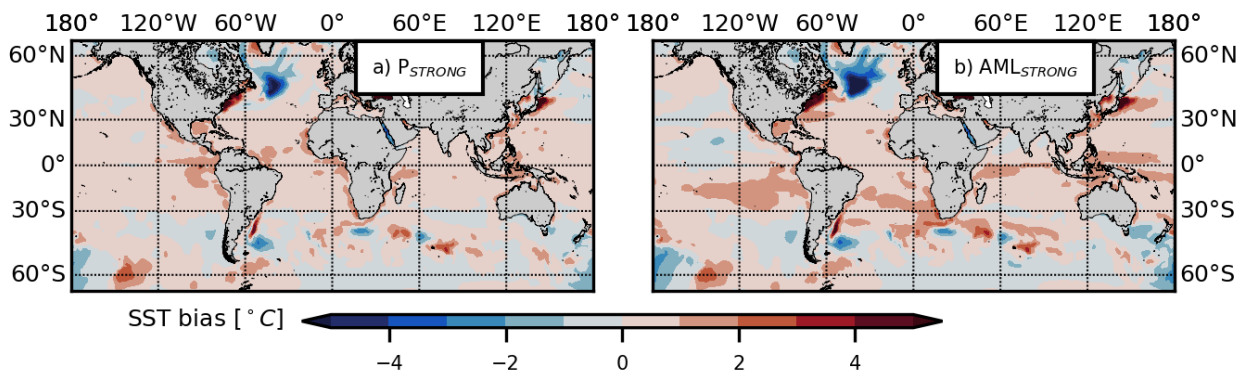
Figure 6.7: SST bias [°C] for the years 1995-2004 relative to the Levitus et al. (1998) climatology for (a) P_{STRONG} and (b) AML_{STRONG}.

The latitude-depth distribution of the global temperature and salinity is a useful benchmark illustrating the drift in ocean models. It provides some insight into the representation of the wind-driven and thermohaline circulation and the properties of water masses. Even if the hindcast period of 50 years is too short for the mid-depth and deep ocean to equilibrate the emerging deviations from the observed temperature and salinity distribution can give a first indication of the model behaviour. Given the short integration period most biases are found in the top 2000m (Fig. 6.8). At the high latitudes even below 1000m there is a modest warming that is probably associated with a relatively weak overturning and deep water production. Above about 500m a warming is found and below 500m the waters got cooler. The warming around 40°N is associated with the warming in the Gulf Stream and Kuroshio regions discussed above. In contrast in the tropics where only little changes were found at the surface there is a strong subsurface warming.

The warm bias found at about 40°S is due to warming in the Malvinas confluence and Agulhas regions, but also smaller warming patched at the same latitude. The salinity biases show similar patterns but there are some exceptions. For example the low salinity tongue associated with intermediate waters (Fig. 6.8e,f) in the southern ocean shows a cooling below 500m but the freshening happens closer to the surface. Another symptomatic feature for the weak overturning is the freshening north of 60°N. Overall the picture resembles the surface biases signal: where P_{STRONG} has biases that are probably associated with the ocean model itself the amplitude is larger for AML_{STRONG} because the constraints of prescribed temperature and humidity are released.
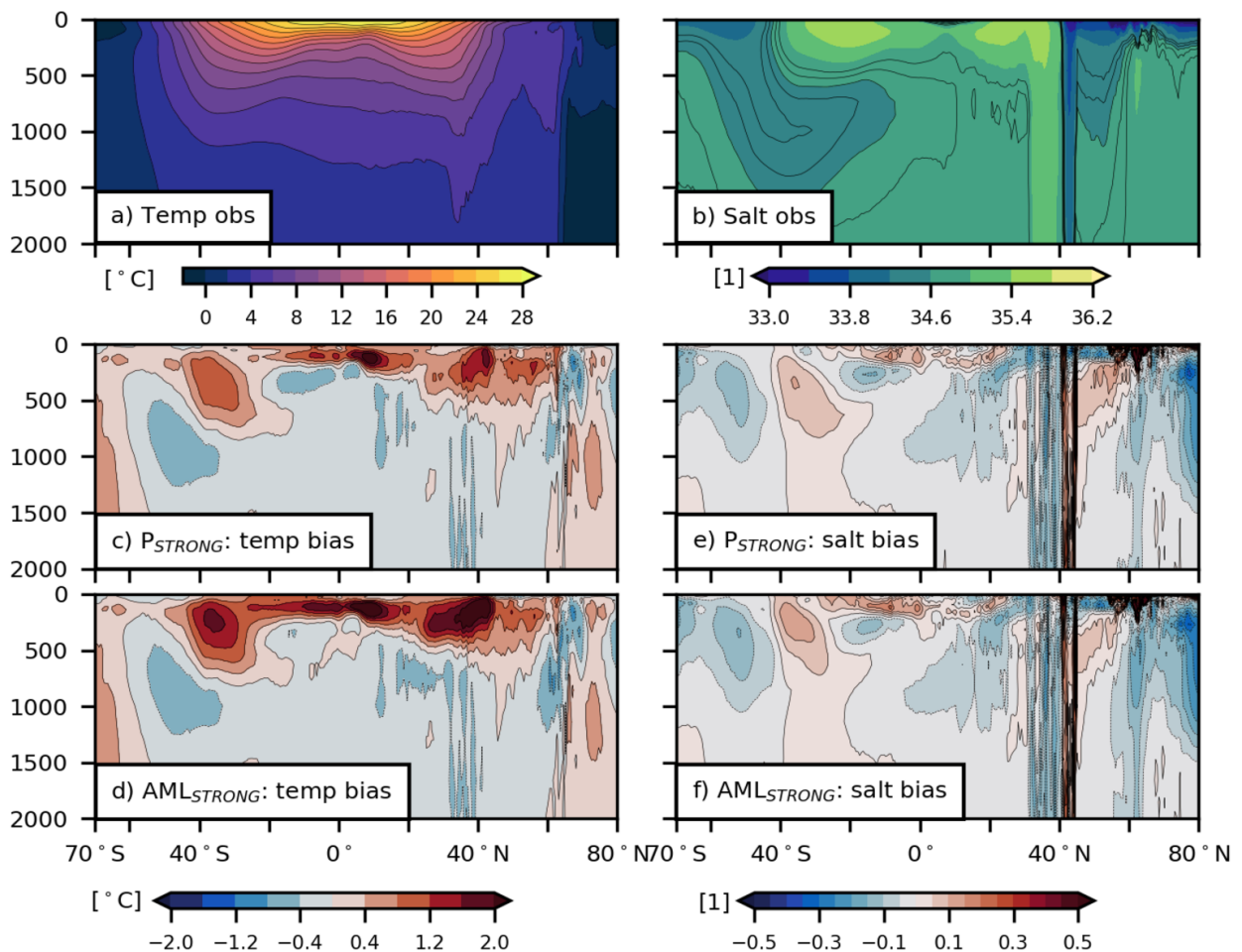
Figure 6.8: Zonal mean (a) temperature [°C] and (b) salinity [1] from Levitus et al. (1998) and biases for temperature for (c) P_{STRONG} and (d) AML_{STRONG}, as well as for salinity (e) P_{STRONG} and (f) AML_{STRONG} for the years 1995-2004 relative to the Levitus et al. (1998) climatology.

Time series of globally averaged temperature and salinity are a basic diagnostic for ocean models. As there are no interior sources or sinks of temperature and salinity both are affected by surface fluxes and exchange with sea ice. The reason for drifts in temperature and salinity in an ocean model are that the freshwater and temperature cycle are not completely closed in the model – as there are no land and atmosphere components – but also that the forcing data set

was build on a SST that does not match the model's SST (Fig. 6.9). Over the 50-year hindcast period the drifts are below $0.1°C$ which is relatively small compared to drifts found in other ocean models (Griffies et al., 2009). For salinity the drifts are likewise small and below 0.01. Overall this analysis shows that the drifts of temperature and salinity in the AML experiments are relatively small which is an important condition for hindcast simulations.
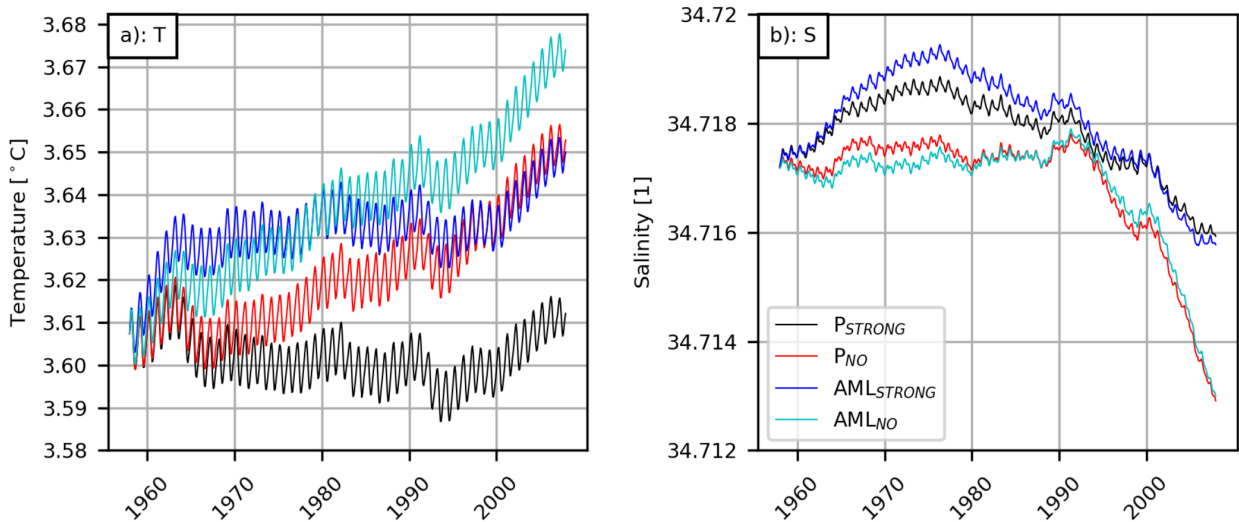
Figure 6.9: Times series of global mean (a) temperature and (b) salinity.

6.3.4 Transports through key locations

Transports through key locations are a good indication how well the model simulations perform in reproducing the exchange between ocean basins. The transports are based on the barotropic stream function for the last five years of the integration (Table 6.3). The transport through the Drake Passage is an indicator for the Antarctic Circumpolar Current and the estimates are very close to the 134 Sv (1 Sv = 10^6 m^3 s^{-1}) reported by Cunningham et al. (2003). The strength seems to be insensitive to the formulation of salinity restoring and prescription of turbulent heat fluxes. Transport through the Indonesian Archipelago is well represented (-15 Sv; Sprintall et al., 2009) and only small differences are found between the simulations. Transports across the Iceland-Scotland Ridge (7.6 Sv) are found to be in good agreement with observations for the period of 1999-2001 (Østerhus et al., 2005). The transport into the Arctic through the Bering Strait is observed to be 1.0 Sv (Woodgate et al., 2012). The Bering Strait transport in the experiments without salinity restoring is weaker by 0.1-0.2 Sv and in the experiments with salinity restoring larger by 0.1; all experiments have a 0.5 Sv standard deviation. The largest differences occur in the strength of the AMOC. This is expected as the AMOC is reportedly sensitive to heat and freshwater forcing which is varied between the simulations. Without salinity restoring the AMOC strength in the experiments with a prescribed forcing drops by 2.7 Sv and by 2.4 in the experiments that are coupled to the AML model. Overall, the transports through key locations experience no strong changes with the exception of the Iceland-Scotland transport and the AMOC which is discussed in the next section.

	DP	ITF	BS	IS	$AMOC_{26.5N}$
Obs	134 ± 11.2	-15 (-18.7,-10.7)	1.0	7.6	18.8 ± 3.4
P_{STRONG}	118.9 ± 4.7	-14.2 ± 2.9	1.1 ± 0.5	5.6 ± 1.8	12.2 ± 2.5
P_{NO}	118.6 ± 4.7	-14.0 ± 2.8	0.8 ± 0.5	6.9 ± 1.9	9.5 ± 2.5
AML_{STRONG}	119.4 ± 4.8	-14.1 ± 2.9	1.1 ± 0.5	5.6 ± 1.8	12.1 ± 2.6
AML_{NO}	118.7 ± 4.7	-14.0 ± 2.8	0.9 ± 0.5	7.0 ± 1.9	9.7 ± 2.6

Table 6.3: Aspects of climatic relevant transports [Sv] for Drake Passage (DP), Indonesian Archipelago (ITF), Bering Strait (BS) and Iceland-Scotland Ridge (IS) averages and standard deviation based on monthly values for 2002-2007. AMOC estimates are averaged from April 2004 to December 2007.

6.4 AMOC drift and temperature advection

The main question of this section concerns the temperature advection associated with the AMOC. It is common practice to use bulk formulations in conjunction with prescribed atmospheric temperature and humidity to estimate the turbulent heat fluxes. However, this practice assumes an atmospheric model with infinite heat capacity. Therefore Griffies et al. (2009) argue that since ocean temperature anomalies are restored to atmospheric conditions, the temperature advection feedback is diminished, rendering the AMOC overly sensitive to salinity biases (Rahmstorf and Willebrand, 1995; Lohmann et al., 1996). In the following the hypothesis is tested if a modification of the turbulent heat fluxes by an AML model can alter the temperature advection feedback when coupled to an ocean-sea ice model.

First the influence of salinity restoring and turbulent heat fluxes by the AML model are investigated. The AMOC strength at 26°N (Fig 6.10a) is relatively stable in the simulations with SSS restoring (P_{STRONG} and AML_{STRONG}) and declines by about 2 Sv in the simulations without SSS restoring (P_{NO} and AML_{NO}). For the P-cases this behaviour is anticipated and has been extensively studied before (e.g., Griffies et al., 2009; Behrens et al., 2013). The simulations with the AML model show a slightly stronger AMOC. The interannual variability is very similar in all simulations, suggestive of a dominant influence of the wind forcing.
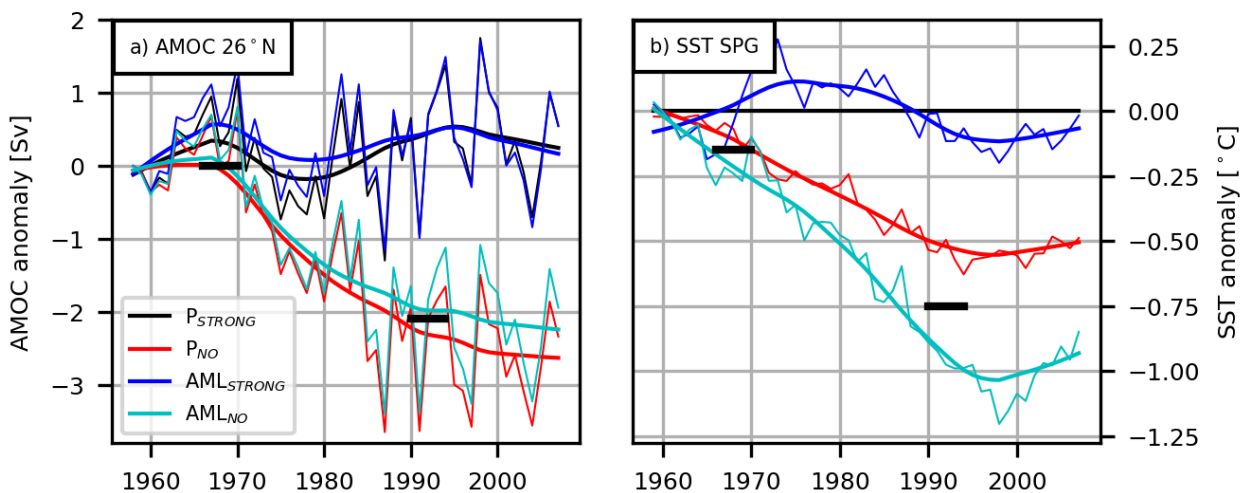
Figure 6.10: (a) AMOC anomaly at 26°N relative to the first time. (b) SST averaged over the SPG (see red box in Fig. 6.11) relative to P_{STRONG}. Bold lines indicate 20-year lowess filtered time series. Black bars indicate the periods used for Fig. 6.11.

As a consequence of the AMOC decline the SSTs in the North Atlantic between 40° and 70°N get colder. This is illustrated in Fig. 6.11 for the period 1966-1970 relative to 1990-1994 for the simulations AML_{NO} and P_{NO}. Note that over the same period a warming in the Gulf Stream region and a cooling in the subpolar gyre in P_{STRONG} is found despite a stable AMOC. A possible

explanation is the shift from a negative state of the North Atlantic Oscillation (NAO) to a positive state, which results in a overturning response that can explain such a warming/cooling pattern (Bellucci and Richards, 2006). To remove the NAO driven signal the SST change from the P_{STRONG} experiment is removed in P_{NO} and AML_{NO}. The cooling pattern in P_{NO} and AML_{NO} can be separated in three parts: One, in the eastern part of the basin (east of 35°W) a strong cooling exceeding -2°C (AML_{NO}) along the main advection path of the NAC is found, which is smaller in P_{NO}. The enhanced cooling in AML_{NO} is a direct result of the reduction in the turbulent heat fluxes by over 30 Wm^{-2} as the atmospheric temperature and humidity adapted to the reduced transport of warm waters along the NAC. Two, a cooling in the Labrador Sea, which is in conjunction with a warming of intermediate waters. The reason for this is a reduced salt transport into the Labrador Sea because the SSS restoring is turned off. This causes a weakening of the convection. And this ultimately results in the surface cooling and warming of intermediate waters due to ongoing strong heat losses in the winter month, but a weakened convection that does not reach the intermediate waters (not shown). Third, a cooling in the North Atlantic Bight. On a regional mean (red box in Fig. 6.11) the cooling is -0.74°C in AML_{NO} and -0.47°C in P_{NO}.
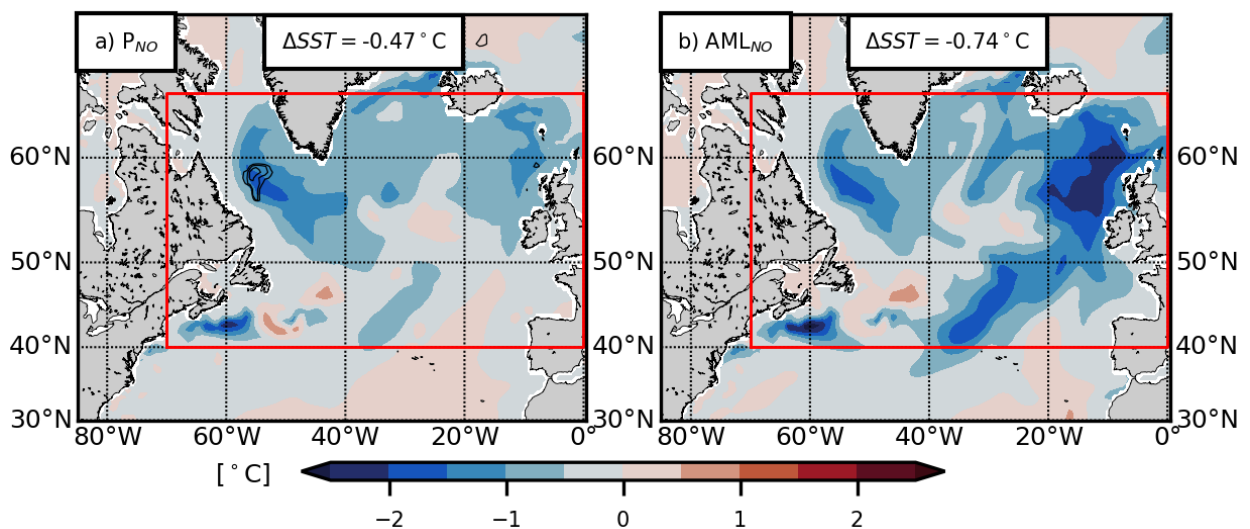
Figure 6.11: Advective cooling due to a decline of the AMOC. SST differences for November to May (1990-1994 minus 1966-1970) in (a) P_{NO} and (b) AML_{NO} relative to P_{STRONG}. The area mean ΔSST is averaged over the red box. Black lines indicate maximum march mixed layer depth (CI: 700,800,900m).

As a measure of the strength of the temperature advection feedback the temperature changes in the subpolar gyre are regressed on the AMOC changes, following (Caesar et al., 2018). For the 1990-1994 minus 1966-1970 period the strength of the temperature advection feedback is 0.18 K Sv^{-1} for P_{NO} and 0.33 K Sv^{-1} for AML_{NO}: the response in AML configuration is nearly twice as large as in a standard ocean-only configuration (Caesar et al., 2018, estimated 0.26 K Sv^{-1} for a CMIP5 ensemble). By the end of the integration the AMOC is about 0.3 Sv stronger in AML_{NO} than in P_{NO}. Even after 30 years of a weakened AMOC the largest cooling happened not in the

Labrador Sea and in the GIN seas (not shown) but rather in the northeastern Atlantic. Thus even if the temperature advection feedback is at work the impact on the convection regions seems to be small. It appears, however, that – at least in the configuration used here – this 'reintroduction of the temperature advection feedback' is not sufficiently strong to sustain a stable AMOC without SSS restoring.

6.5 Summary & Conclusions

The SST has a strong hold on near-surface atmospheric temperature and humidity — a feature that is missing in ocean-only models as the atmospheric conditions need to be prescribed. This bears a problem for the computation of the air-sea fluxes: the ocean model state deviates from the observed state and thus the SST and atmospheric temperature and humidity are not related. In this atmospheric adjustment is enabled by using a simple atmospheric boundary layer model (CheapAML; Deremble et al., 2013) for the computation of the turbulent air-sea fluxes. Atmospheric temperature and humidity adjust to the underlying SST and are advected by prescribed winds. The "Cheap" refers to the computational overhead which is only about 5%.

For the first time CheapAML was tested in a hindcast setup for a period of 50 years. The large-scale temperature and humidity adjustment happens in regions where the ocean state deviates from the observed state, such as western boundary current systems and in particular in the region of the "Northwest Corner" of the NAC. These adjustments bring the system into more realistic local and regional relation between the oceanic and atmospheric conditions and therefore allow for improved turbulent heat fluxes. For example, the time-mean heat flux changes are over $+50$ Wm^{-2} in the eastern tropical Pacific, $+30$ Wm^{-2} in the North Atlantic and -20 Wm^{-2} over the Western Boundary Currents. On a global scale the heat imbalance is altered by about $+0.3$ Wm^{-2}, still within the spread of other model studies and observational estimates (Wild et al., 2015; Trenberth et al., 2009). Changes in the global freshwater balance are also marginal. On the other hand, releasing the implicit temperature restoring caused by the prescription of atmospheric temperature and humidity leads to an amplification of regional temperature and salinity biases. Large scale and inter-ocean transports such as the Drake Passage, Bering Strait, Island-Scotland Ridge and the transport through the Indonesian Archipelago are only minimally changed.

Particular attention has been drawn on the AMOC. The hypothesis was tested that the AML model modifies the temperature advection feedback associated with the AMOC. When the atmosphere can adapt to another oceanic state, i.e. the ocean model is coupled to an AML model, the strength of the temperature advection feedback is 0.33 K Sv^{-1}, in contrast to the 0.18 Sv^{-1} for a forced simulation. However, the largest changes in SST occur in the northeastern Atlantic where no convection is occurring. The enhanced temperature advection feedback is not able to

significantly affect the AMOC during the course of these experiments. These findings appear in conflict with the findings of Rahmstorf and Willebrand (1995); Lohmann et al. (1996) who demonstrated that simple Energy Balance Models allow the SST to evolve freely and a temperature advection feedback for the AMOC can be established due to a reduced sensitivity of the AMOC to freshwater perturbations. The cause for this conflict is not clear but the circulation in the North Atlantic and the deep water formation are much more complex in state-of-the-art ocean models than in the idealized models with 3.75°x4° and 2°x2° resolution used by Rahmstorf and Willebrand (1995) and Lohmann et al. (1996), respectively. The long integration time used in Lohmann et al. (1996) might be another reason.

The coupling of CheapAML to an ocean-only model offers a partial solution for unrealistic turbulent heat fluxes resulting from the mismatch of prescribed atmospheric conditions and the model's SST. The configuration used in this study could benefit from improvements near the ice-edge and coasts and over small scale features. Upgrading CheapAML to work over land and sea-ice could potentially improve the model performance at the ice-edge and close to the coast where the advection of temperature and humidity plays an important role. Recently, Horvat et al. (2016) reported on an adaptation of CheapAML to extend the use to ice-covered regions. In the present study temperature and humidity had to be restored over sea-ice and land. Another issue is the interaction between ocean and atmosphere over small and mesoscale features. Numerous studies (e.g. Chelton et al., 2007; Small et al., 2008; Frenger et al., 2013; Byrne et al., 2016) reported on the impact of mesoscale features on the near-surface atmosphere and in particular winds. Such feedbacks are not covered by CheapAML because the winds are prescribed and convection is not possible in a one-layer model. While convection itself could probably not be implemented in CheapAML the mean effect of mesoscale features on the winds might get parameterized (Pezzi et al., 2004; Jin et al., 2009).

Appendix

Appendix A: Effective temperature restoring

In the coupled atmosphere-ocean system the turbulent heat fluxes act to reduce the temperature and humidity gradient between atmosphere and ocean. Effectively the atmospheric temperature adjusts to the SST. In an ocean-only model this adjustment is not possible and therefore the SST effectively adjusts to the atmospheric temperature and humidity. In the following it is roughly estimated how strong this effective restoring is. Following (Rahmstorf and Willebrand, 1995) it is assumed that the drag coefficient is constant $C_d = 1.4 \cdot 10^{-3}$, a moderate wind $U_{10} = 8\text{ms}^{-1}$ and standard values for relative humidity $h = 0.85$, $SST = 10°$ and atmospheric temperature $T_A = 9°$. Then the bulk formulations for sensible heat flux (Eq. 6.2) and evaporation (Eq. 6.7) times the latent heat of vaporization gives the latent heat flux. Then the coupling coefficients are 14 $\text{Wm}^{-2}\text{K}^{-1}$ for sensible heat flux and 52 $\text{Wm}^{-2}\text{K}^{-1}$ for latent heat flux. This is close to the Rahmstorf and Willebrand (1995) estimate of 50 $\text{Wm}^{-2}\text{K}^{-1}$.

With this it is possible to estimate a restoring time scale for the surface ocean. Given the coupling coefficient for the sensible and latent heat flux c_{SH} and c_{LH} the restoring time scale T_{REST} is:

$$T_{REST} = H \cdot \rho_w \cdot C_P / (c_{SH} + c_{LH}),$$

where $C_P \approx 1000.5$ J kg^{-1} K^{-1} is the specific heat capacity of water, $\rho_w = 1025$ kg m^{-3} mean density of water and H water depth. For a water depth of $H = 40\text{m}$ this would be a restoring time scale of 30 days.

Appendix B: AML parameter tuning

The current version of CheapAML offers two tuning parameters for upward longwave radiation (γ) and humidity entrainment (μ). Generally higher values of γ decrease the outgoing longwave radiation and therefore increase atmospheric temperature and humidity (Fig. B1). When the values of μ is increased global mean temperature and humidity decrease. (Fig. B1). As both μ and γ determine temperature and humidity the tuning demands to keep one parameter constant and tune the model to the other parameter. This process might be repeated to get the best possible set of parameters. In order to minimize the restoring fluxes $\gamma = 0.25$ and $\mu = 0.24$ are used for the simulations. These parameters probably change for other ocean models, configuration and other forcing datasets.
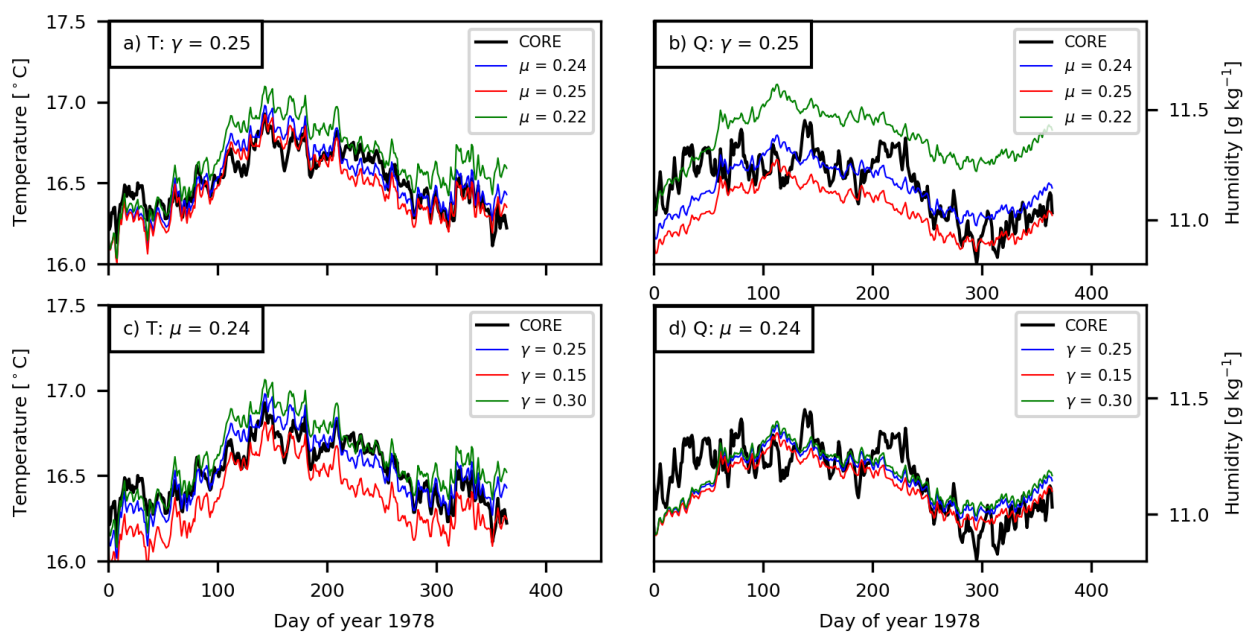
Figure B1: Parameter tuning (a,b) γ and (c,d) μ. Global mean (a,c) temperature [°C] and (b,d) humidity [g kg^{-1}] for prescribed atmospheric temperature and humidity (thick black) and different choices of γ and μ. Tuning parameters used for the experiments are $\gamma = 0.25$ and $\mu = 0.24$.

Appendix C: AML heat and freshwater fluxes

In order to understand the behaviour of the AML model all components are assessed on a global scale. In the following the model was coupled to the NEMO ocean model (experiment reference AML_{NO}). The first 10 years of the simulation have been investigated. Sign convention is such that positive flux is from the ocean into the atmosphere.

The heat budget is determined by the following fluxes: upward ($F_l^{\uparrow}$) and downward ($F_l^{\downarrow}$) longwave flux, outgoing longwave radiation from ocean ($F_{ol}^{\uparrow}$), sensible (SH) and latent (LH) heat flux, and global mean restoring (F_{REST}). The three longwave radiative fluxes can be combined into a net longwave radiation which is generally small with maxima over the western boundary current regions and minima over the Southern Ocean (Fig. C1a-c). The sensible heat flux is generally positive with only a few exceptions and does reach up to 100 Wm^{-2} over the Kuroshio region. Temperature advection plays an important role in particular over the WBC regions where cold air masses are advected to balance the sensible heat loss. Sensitivity experiments demonstrated that if the advection is turned off, sensible and latent heat fluxes are strongly underestimated over these regions (not shown; cf Seager et al. (1995)). The net heat flux is small (only up to $\pm$ 3 Wm^{-2}), but can vary from season to season. The global and time mean values are listed in Tab. C1.

The humidity budget of CheapAML is determined by evaporation (E), humidity entrainment ($F_q^{\uparrow}$), precipitation (P) and global mean restoring (F_{REST}) (Fig. C1d-g). The largest source of freshwater is evaporation in particular over the WBC and the subtropical gyres. Humidity entrainment acts to balance the gain of freshwater through evaporation with large negative values in the tropics and subtropics. Close to the continents advection of dry air can play an important role in particular over the WBC in order to balance the strong latent heat losses. The rain in the CheapAML budget is small with largest values in the tropics. Note that the rain distribution is quite noisy as it is determined by the vertical wind, which is estimated by the horizontal wind convergence. In total the freshwater forcing in CheapAML can reach up to 1 mm day^{-1} over the western boundary current regions or quite large where advection is strong. The global and time mean values are listed in Tab. C1.
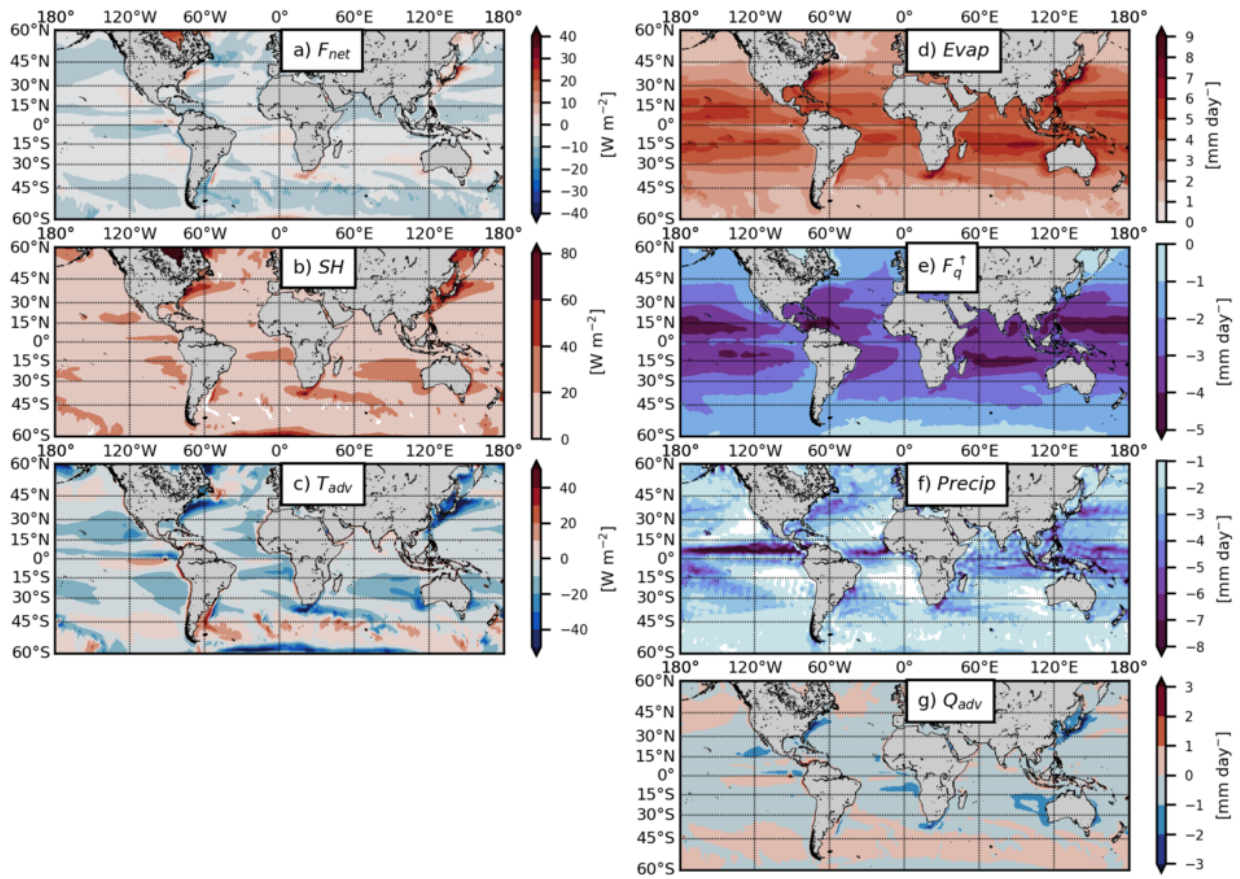
Figure C1: Time-mean components of the AML budget for the first ten years of the integration. The heat budget is given by (a) net long wave radiation, F_{net}, (b) sensible heat flux, SH and (c) temperature advection T_{adv}. The freshwater budget is given by (d) evaporation, Evap, (e) humidity entrainment, $F_q^\uparrow$, (f) precipitation, Precip and (g) humidity advection, Q_{adv}.

Heat				Freshwater		
F_{net}		-3.1	± 0.8	E	3.31	± 0.13
	$F_{ol}^\uparrow$	387.6	± 2.0	$F_q^\uparrow$	-2.57	± 0.10
	$F_l^\downarrow$	-198.0	± 0.9	P	-0.28	± 0.02
	$F_l^\uparrow$	-192.7	± 0.8	Q_{adv}	-0.27	± 0.05
SH		16.3	± 1.6	$Q_{damping}$	-0.10	± 0.08
T_{adv}		-7.9	± 1.2			
$T_{damping}$		-3.7	± 1.7			
Total		-1.6	± 0.9	Total	-0.07	± 0.05

Table C1: Global mean AML_{NO} heat $[\text{Wm}^{-2}]$ and freshwater $[\text{mm day}^{-1}]$ fluxes for the first ten years of the spinup. Uncertainty is given as standard deviation based on 5-daily values. Only ice free areas are considered.

7 Summary

In this thesis, aspects of the air-sea exchange in ocean and atmosphere-ocean models were investigated. Of particular interest was the most obvious but also most crucial assumption in ocean-only models: prescribed atmospheric conditions do not allow for feedbacks from the ocean to the atmosphere. In the preceding chapters partial solutions were discussed in order to allow for thermal and mechanical feedbacks with the atmosphere. Particular attention was paid to the damping effect of mechanical and thermal air-sea fluxes on the ocean currents. The relative strength of the damping was quantified and it was shown that the effect is underestimated in coupled climate models with diverging atmosphere and ocean model grid resolutions. In addition, the issue of potential ocean imprints on forcing data sets often used to force ocean-only models was discussed. These imprints might have adverse consequences on the mechanical coupling for the ocean simulation. The questions raised in the introduction are now answered in detail:

- **Q1: Is there an imprint of the ocean surface currents in common forcing datasets? (chapter 2)**

  Scatterometer derived winds represent the relative motion between the atmosphere and the ocean. In this study it is demonstrated that for QuikSCAT derived winds these ocean imprints lead to a negative bias in the wind work on small spatial temporal scales. In regions with strong currents like the Gulf Stream, Kuroshio, Agulhas, Malvinas and ACC these biases are found to be most pronounced. On a global mean these biases account for a reduction of the wind work on the order of 30-40 GW.

  Because of their near-global coverage and moderate temporal and spatial resolution QuikSCAT winds are often used as a reference. For example, for the reanalysis model ERA-Interim and the forcing dataset JRA-55-do the QuikSCAT winds are used to correct their winds. In ERA-Interim the QuikSCAT winds are directly assimilated during production whereas the correction process for JRA-55-do is done on the time-mean winds. This raises the question if the ocean imprints in QuikSCAT winds are passed on to the reanalysis models or forcing dataset. In this study no imprints on small spatial and temporal scales have been found in ERA-Interim and JRA-55-do.

- **Q2: Can the air-sea coupling in global ocean-only models be improved by a**

simple modification of the bulk formulation for the momentum flux (wind stress)? (chapter 3)

In the presence of ocean currents the wind power input is generally reduced. On small spatial scales this reduction can be expressed by the linear relationship between the curl of the surface stress and the surface currents. The slope of this linear relationship, s_{st} is a measure for the strength of this reduction. This strength is commonly overestimated in ocean-only models. For example, we find in the Gulf Stream Extension $s_{st} \approx -3.2$ for an ocean-only model and $s_{st} \approx -2.2$ in two coupled model simulations. This is equivalent to an overestimation of the mechanical damping of ocean surface currents.

Renault et al. (2016c) argued that in ocean-only models there is a missing feedback that 're-energizes' the winds and thus reduces mechanical damping. In the present study this feedback is further investigated. The strength of the feedback is given by the slope of the linear regression between the curl of the ocean surface currents and the curl of the winds on small spatial scales, s_w. The strength is found to be spatially and temporally heterogeneous, dependent on the near-surface stability and varies roughly between 0.2 and 0.5.

This brings us back to the question: Can mechanical air-sea coupling in ocean-only models be improved? In the present study the feedback to the atmosphere is implemented in an ocean-only model using a tweak proposed by Renault et al. (2016c). The tweak uses the coupling coefficient s_w to re-energize the atmospheric winds. Using a spatially and temporally variable s_w (obtained from two coupled simulations) the tweak is tested for the first time. It is demonstrated, that the mechanical air-sea coupling is improved using s_{st} as a measure. For example, in the Gulf Stream Extension region the damping strength is $s_{st} \approx -2.4$ for the ocean-only simulation with the tweak. This is an improvement of 0.8. This means that in such a simulation the mechanical damping should be much closer to the strength found in coupled simulations.

- **Q3: What is the relative importance of the thermal and mechanical damping for the ocean dynamics? (chapter 4)**

  Air-sea fluxes at the mesoscale act to dampen ocean currents and SST anomalies. These damping mechanisms can be separated into mechanical and thermal damping. Both damping mechanisms have been considered individually by former studies and it was demonstrated that these have a strong impact on the kinetic energy (Seo et al., 2016; Ma et al., 2016; Renault et al., 2016c,b, 2017b). In this study the damping mechanisms have been switched off using a spatial low-pass filter in an eddy-permitting ocean model. This results in strong changes in the ocean kinetic energy, in particular in the WBC regimes with local increases

up to 40 cm s^{-1} in the time-mean currents. Strong increases are found at the mesoscale, but also at larger spatial scales associated with shifts in the mean current field. Theses increases are unequally pronounced in the WBC regimes with the strongest changes in the Kuroshio Extension followed by the Gulf Stream Extension and the Agulhas regime (c.f. Fig. 4.10). Overall, the mechanical damping is stronger than the thermal damping — at least in the configuration used for this study. For example, in the Kuroshio Extension the kinetic energy increases by 50% at the mesoscale when the mechanical damping is switched off and only 25% when the thermal damping is switched off.

- **Q4: What are the consequences for the simulation of the ocean if the oceanic component is better resolved than the atmospheric component in atmosphere-ocean models? (chapter 5)**

  If the air-sea flux calculation is executed on a coarse atmospheric grid with respect to the oceanic grid the ocean temperature and currents need to be averaged onto the coarse atmospheric grid. This averaging procedure removes small scale temperature and current anomalies which reduces the mesoscale thermal and mechanical damping effects. This effect is called atmospheric coarse graining. In this study an ocean-only model was used to investigate the repercussions of the atmospheric coarse graining for the ocean in isolation. The coarse graining is achieved by averaging SST and surface currents in the $1/4°$-model to a $1°$-grid for the air-sea flux calculation. This coarse graining factor of 4 is representative for CMIP6-class model configurations. This study shows that the coarse graining results in an increase in kinetic energy. Regionally, in the WBC, the kinetic energy increases by up to 13% and globally by 6%. These changes are mainly found in the time-mean circulation. Another consequence of the coarse graining are changes in the net surface heat flux. For example, in the tropical east Pacific a large scale dipole pattern is found with an increase by more than 20 Wm^{-2} on the northern side and an decrease by 5 Wm^{-2} on the southern side. In the subtropical regions dipole patterns with weaker amplitudes are found. Also, the changes in the WBC are characterized by dipole patterns which are more localized, but with large amplitudes exceeding 30 Wm^{-2}. In the global mean the dipole patterns cancel each other out which results in a residual of 0.02 Wm^{-2} for the entire integration.

  Despite these quite strong changes in the surface heat fluxes and the surface currents, the effect on the temperature distribution is surprisingly small. In general, only small, non-significant changes have been found in the basin-scale temperature and in the meridional heat transports. Based on the results of this study, it can be concluded that the coarse graining effect has strong repercussions for the ocean surface currents locally and globally, but effects the net heat fluxes only locally. Impacts on the large scale temperature distribution are only minor.

- **Q5: Can a simple atmospheric mixed layer model (AML) reduce large-scale heat flux errors and re-introduce the temperature advection feedback in a state-of-the-art ocean-only model? (chapter 6)**

  In a series of 50-year long ocean-only hindcast simulations it was tested if the temperature and humidity can be estimated by an AML model instead of prescribing them. SST biases in the ocean model that result in heat flux biases in a convectional ocean-only model result in adjustments of the AML temperature and humidity. As a consequence the air-sea temperature difference patterns found in models coupled to atmospheric general circulation models are well reproduced in the AML setup. This results in strong changes in the surface heat fluxes, e.g. more than $+50$ Wm^{-2} in the eastern tropical Pacific, $+30$ Wm^{-2} in the North Atlantic and -20 Wm^{-2} over the Western Boundary Currents. Regional and global temperature and salinity drifts are enhanced, but still small compared to drifts from other ocean models (Griffies et al., 2009).

  The second part of the question concerns the longterm behaviour of the AMOC. For a declining AMOC phase the AML setup and the forced ocean-only configuration are compared. It is shown that in the AML setup the mean SST in the subpolar North Atlantic cools by about -0.74°C and therefore much stronger than the -0.47°C found in the forced ocean-only configuration. The strength of the temperature advection feedback is also increased with 0.33 K Sv^{-1} in the AML setup, in contrast to the 0.18 K Sv^{-1} for a forced simulation. However, even if the temperature advection feedback is strengthened, it is not sufficiently strong to retain the AMOC decline. A possible explanation is that the largest SST changes occur in the northeastern Atlantic and not in the convection regions. To conclude, even in the AML setup a sufficiently strong SSS restoring is needed to maintain a stable AMOC.

Bibliography

Abel, R., 2013: Subtropical and Subpolar Gyre Circulation of the North Atlantic in Ocean Models at Different Resolutions. Master thesis, University of Kiel, 93 pp.

Antonov, J., S. Levitus, B. T., M. Conkright, O'Brien T., and C. Stephens, 1998: World Ocean Atlas 1998 Vol. 1: Temperature of the Atlantic Ocean. *U.S. Government Printing Office, Washington, D.C.*

Barnier, B., and Coauthors, 2006: Impact of partial steps and momentum advection schemes in a global ocean circulation model at eddy-permitting resolution. *Ocean Dyn.*, **56 (5-6)**, 543–567, doi:10.1007/s10236-006-0082-1.

Beal, L. M., and Coauthors, 2011: On the role of the Agulhas system in ocean circulation and climate. *Nature*, **472 (7344)**, 429–436, doi:10.1038/nature09983.

Behrens, E., A. Biastoch, and C. W. Böning, 2013: Spurious AMOC trends in global ocean sea-ice models related to subarctic freshwater forcing. *Ocean Model.*, **69**, 39–49, doi:10.1016/j.ocemod.2013.05.004.

Bellucci, A., and K. J. Richards, 2006: Effects of NAO variability on the North Atlantic Ocean circulation. *Geophys. Res. Lett.*, **33 (2)**, L02 612, doi:10.1029/2005GL024890.

Bentamy, A., S. A. Grodsky, B. Chapron, and J. A. Carton, 2013: Compatibility of C- and Ku-band scatterometer winds: ERS-2 and QuikSCAT. *J. Mar. Sys.*, **117-118**, 72–80, doi:10.1016/j.jmarsys.2013.02.008.

Biastoch, A., J. V. Durgadoo, A. K. Morrison, E. van Sebille, W. Weijer, and S. M. Griffies, 2015: Atlantic multi-decadal oscillation covaries with Agulhas leakage. *Nature Communications*, **6**, 10 082, doi:10.1038/ncomms10082.

Blanke, B., 1993: Variability of the tropical Atlantic Ocean simulated by a general circulation model with two different mixed-layer physics. *J. Phys. Oceanogr.*

Boebel, O., T. Rossby, J. Lutjeharms, W. Zenk, and C. Barron, 2003: Path and variability of the Agulhas Return Current. *Deep Sea Res. Part II Top. Stud. Oceanogr.*, **50 (1)**, 35–56, doi:10.1016/S0967-0645(02)00377-6.

Boyer, T., S. Levitus, J. Antonov, M. Conkright, T. O'Brien, and C. Stephens, 1998: World Ocean Atlas 1998 Vol. 4: Salinity of the Atlantic Ocean. *U.S. Government Printing Office, Washington, D.C.*

Bretherton, C. S., M. Widmann, V. P. Dymnikov, J. M. Wallace, and I. Bladé, 1999: The Effective Number of Spatial Degrees of Freedom of a Time-Varying Field. *J. Clim.*, **12 (7)**, 1990–2009, doi:10.1175/1520-0442(1999)012⟨1990:TENOSD⟩2.0.CO;2.

Brodeau, L., B. Barnier, S. K. Gulev, and C. Woods, 2017: Climatologically Significant Effects of Some Approximations in the Bulk Parameterizations of Turbulent Air-Sea Fluxes. *J. Phys. Oceanogr.*, **47 (1)**, 5–28, doi:10.1175/JPO-D-16-0169.1.

Bryan, F., 1986: High-latitude salinity effects and interhemispheric thermohaline circulations. *Nature*, **323 (6086)**, 301–304, doi:10.1038/323301a0.

Bryan, F. O., R. Tomas, J. M. Dennis, D. B. Chelton, N. G. Loeb, and J. L. Mcclean, 2010: Frontal scale air-sea interaction in high-resolution coupled climate models. *J. Clim.*, **23 (23)**, 6277–6291, doi:10.1175/2010JCLI3665.1.

Byrne, D., M. Munnich, I. Frenger, and N. Gruber, 2016: Mesoscale atmosphere ocean coupling enhances the transfer of wind energy into the ocean. *Nature Communications*, **(May)**, 1–8, doi:10.1038/ncomms11867.

Caesar, L., S. Rahmstorf, A. Robinson, G. Feulner, and V. Saba, 2018: Observed fingerprint of a weakening Atlantic Ocean overturning circulation. *Nature*, **556 (7700)**, 191–196, doi:10.1038/s41586-018-0006-5.

Cai, W., and S. Godfrey, 1995: Surface heat flux parameterizations and the variability of the thermohaline circulation. *J. Geophys. Res.*, **100**.

Cayan, D. R., 1992: Latent and Sensible Heat Flux Anomalies over the Northern Oceans: The Connection to Monthly Atmospheric Circulation. *J. Clim.*, **5 (4)**, 354–369, doi:10.1175/1520-0442(1992)005⟨0354:LASHFA⟩2.0.CO;2.

Chelton, D. B., R. A. DeSzoeke, M. G. Schlax, K. El Naggar, and N. Siwertz, 1998: Geographical Variability of the First Baroclinic Rossby Radius of Deformation. *J. Phys. Oceanogr.*, **28 (3)**, 433–460, doi:10.1175/1520-0485(1998)028⟨0433:GVOTFB⟩2.0.CO;2.

Chelton, D. B., and M. H. Freilich, 2005: Scatterometer-Based Assessment of 10-m Wind Analyses from the Operational ECMWF and NCEP Numerical Weather Prediction Models. *Month. Weather Rev.*, **133**, 409–429, doi:10.1175/MWR3111.1.

Chelton, D. B., M. G. Schlax, M. H. Freilich, and R. F. Milliff, 2004: Satellite measurements reveal persistent small-scale features in ocean winds. *Science (New York, N.Y.)*, **303 (5660)**, 978–83, doi:10.1126/science.1091901.

Chelton, D. B., M. G. Schlax, and R. M. Samelson, 2007: Summertime Coupling between Sea Surface Temperature and Wind Stress in the California Current System. *J. Phys. Oceanogr.*, **37 (3)**, 495–517, doi:10.1175/JPO3025.1.

Chelton, D. B., M. G. Schlax, and R. M. Samelson, 2011: Global observations of nonlinear

mesoscale eddies. *Prog. Oceanogr.*, **91 (2)**, 167–216, doi:10.1016/j.pocean.2011.01.002.

Christian, J. R., M. A. Verschell, R. Murtugudde, A. J. Busalacchi, and C. R. McClain, 2002: Biogeochemical modelling of the tropical Pacific Ocean. I: Seasonal and interannual variability. *Deep Sea Res. Part II Top. Stud. Oceanogr.*, **49 (1-3)**, 509–543, doi:10.1016/S0967-0645(01) 00110-2.

Cornillon, P., and K. A. Park, 2001: Warm core ring velocities inferred from NSCAT. *Geophys. Res. Lett.*, **28 (4)**, 575–578, doi:10.1029/2000GL011487.

Cronin, M. F., and J. Sprintall, 2001: Wind- and Buoyancy-Forced Upper Ocean. *Encyclopedia of Ocean Sciences*, 3219–3227, doi:10.1016/B978-012374473-9.00624-X, arXiv:1011.1669v3.

Csanady, G. T., 2001: *Air-Sea Interaction Laws and Mechanisms*. 1st ed., Cambridge University Press, Cambridge, 1–239 pp.

Cunningham, S. A., S. G. Alderson, and B. A. King, 2003: Transport and variability of the Antarctic Circumpolar Current in Drake Passage. *J. Geophys. Res.*, **108 (C5)**, 8084, doi: 10.1029/2001JC001147.

Dee, D. P., and Coauthors, 2011: The ERA-Interim reanalysis: configuration and performance of the data assimilation system. *Q. J. R. Meteorol. Soc.*, **137 (656)**, 553–597, doi:10.1002/ qj.828.

Delworth, T. L., and Coauthors, 2006: GFDL's CM2 global coupled climate models. Part I: Formulation and simulation characteristics. *J. Clim.*, **19 (5)**, 643–674, doi:10.1175/JCLI3629. 1.

Delworth, T. L., and Coauthors, 2012: Simulated climate and climate change in the GFDL CM2.5 high-resolution coupled climate model. *J. Clim.*, **25 (8)**, 2755–2781, doi:10.1175/ JCLI-D-11-00316.1.

Dencausse, G., M. Arhan, and S. Speich, 2010: Routes of Agulhas rings in the southeastern Cape Basin. *Deep Sea Res. Part I Oceanogr. Res. P.*, **57 (11)**, 1406–1421, doi:10.1016/j.dsr.2010. 07.008.

Deremble, B., N. Wienders, and W. K. Dewar, 2013: CheapAML: A Simple, Atmospheric Boundary Layer Model for Use in Ocean-Only Model Calculations. *Mon. Wea. Rev.*, **141 (2)**, 809–821, doi:10.1175/MWR-D-11-00254.1.

Desbiolles, F., and Coauthors, 2017: Two decades [1992–2012] of surface wind analyses based on satellite scatterometer observations. *J. Mar. Sys.*, **168**, 38–56, doi:10.1016/j.jmarsys.2017. 01.003.

Dewar, W. K., and G. R. Flierl, 1987: Some Effects of the Wind on Rings. 1653–67 pp., doi: doi:10.1175/1520-0485(1987)017.

Duhaut, T., and D. Straub, 2006: Wind Stress Dependence on Ocean Surface Velocity: Implica-

tions for Mechanical Energy Input to Ocean Circulation. *J. Phys. Oceanogr.*, **(36)**, 202–211, doi:10.1175/JPO2842.1.

ECMWF, 2014: IFS documentation—Cy40r1. Operational im- plementation 22 November 2013. Part IV: Physical processes. ECMWF, accessed February 2018. Tech. rep.

Eden, C., and H. Dietze, 2009: Effects of mesoscale eddy/wind interactions on biological new production and eddy kinetic energy. *J. Geophys. Res.*, **114 (C5)**, C05 023, doi:10.1029/2008JC005129.

Eden, C., and R. J. Greatbatch, 2009: A diagnosis of isopycnal mixing by mesoscale eddies. *Ocean Model.*, **27 (1-2)**, 98–106, doi:10.1016/j.ocemod.2008.12.002.

Edson, J. B., and Coauthors, 2013: On the Exchange of Momentum over the Open Ocean. *J. Phys. Oceanogr.*, **43 (8)**, 1589–1610, doi:10.1175/JPO-D-12-0173.1.

Etling, D., 2008: *Theoretische Meteorologie: Eine Einführung*. 3rd ed., Springer Berlin, 37 pp.

Fairall, C. W., E. F. Bradley, J. E. Hare, A. A. Grachev, and J. B. Edson, 2003: Bulk parameterization of air-sea fluxes: Updates and verification for the COARE algorithm. *J. Clim.*, **16 (4)**, 571–591, doi:10.1175/1520-0442(2003)016⟨0571:BPOASF⟩2.0.CO;2.

Fichefet, T., and M. a. M. Maqueda, 1997: Sensitivity of a global sea ice model to the treatment of ice thermodynamics and dynamics. *J. Geophys. Res.*, **102 (C6)**, 12 609, doi:10.1029/97JC00480.

Flato, G., and Coauthors, 2014: Evaluation of climate models. *Climate change 2013- the physical science basis. Contribution of Working Group I to the Fifth Assessment Report of the Intergovernmental Panel on Climate Change*, Cambridge University Press, 741–866, doi:10.1017/CBO9781107415324.020.

Frenger, I., N. Gruber, R. Knutti, and M. Münnich, 2013: Imprint of Southern Ocean eddies on winds, clouds and rainfall. *Nat. Geosci.*, **6 (8)**, 608–612, doi:10.1038/ngeo1863.

Gaube, P., D. B. Chelton, R. M. Samelson, M. G. Schlax, and L. W. O'Neill, 2015: Satellite Observations of Mesoscale Eddy-Induced Ekman Pumping. *J. Phys. Oceanogr.*, **45 (1)**, 104–132, doi:10.1175/JPO-D-14-0032.1.

Gent, P. R., and J. C. Mcwilliams, 1990: Isopycnal Mixing in Ocean Circulation Models. *J. Phys. Oceanogr*, **20 (1)**, 150–155, doi:10.1175/1520-0485(1990)020⟨0150:IMIOCM⟩2.0.CO;2.

Goni, G. J., S. L. Garzoli, A. J. Roubicek, D. B. Olson, and O. B. Brown, 1997: Agulhas ring dynamics from TOPEX/POSEIDON satellite altimeter data. *J. Marine Research*, **55 (5)**, 861–883, doi:10.1357/0022240973224175.

Gordon, A. L., 1986: Interocean exchange of thermocline water. *Journal of Geophysical Research*, **91 (C4)**, 5037, doi:10.1029/JC091iC04p05037.

Griffies, S. M., and Coauthors, 2009: Coordinated Ocean-ice Reference Experiments (COREs).

Ocean Model., **26 (1-2)**, 1–46, doi:10.1016/j.ocemod.2008.08.007.

Griffies, S. M., and Coauthors, 2014: An assessment of global and regional sea level for years 1993-2007 in a suite of interannual core-II simulations. *Ocean Model.*, **78**, 35–89, doi:10.1016/j.ocemod.2014.03.004.

Griffies, S. M., and Coauthors, 2015: Impacts on ocean heat from transient mesoscale eddies in a hierarchy of climate models. *J. Clim.*, **28 (3)**, 952–977, doi:10.1175/JCLI-D-14-00353.1.

Hall, C., and J. R. Lutjeharms, 2011: Cyclonic eddies identified in the Cape Basin of the South Atlantic Ocean. *J. Mar. Sys.*, **85 (1-2)**, 1–10, doi:10.1016/j.jmarsys.2010.10.003.

Hersbach, H., and J.-R. Bidlot, 2008: The relevance of ocean surface current in the ECMWF analysis and forecast system. *Workshop on Ocean-Atmosphere Interactions*, 61–73.

Hewitt, H. T., and Coauthors, 2016: The impact of resolving the Rossby radius at mid-latitudes in the ocean: Results from a high-resolution version of the Met Office GC2 coupled model. *Geosci. Model Dev.*, **9 (10)**, 3655–3670, doi:10.5194/gmd-9-3655-2016.

Holmes, R. M., S. McGregor, A. Santoso, and M. H. England, 2018: Contribution of tropical instability waves to ENSO irregularity. *Clim. Dyn.*, **0 (0)**, 1–19, doi:10.1007/s00382-018-4217-0.

Horvat, C., E. Tziperman, and J. M. Campin, 2016: Interaction of sea ice floe size, ocean eddies, and sea ice melting. *Geophys. Res. Lett.*, **43 (15)**, 8083–8090, doi:10.1002/2016GL069742.

Hughes, C. W., and C. Wilson, 2008: Wind work on the geostrophic ocean circulation: An observational study of the effect of small scales in the wind stress. *J. Geophys. Res.*, **113 (C2)**, 1–10, doi:10.1029/2007JC004371.

Hurlburt, H. E., and P. J. Hogan, 2000: Impact of $1/8°$ to $1/64°$ resolution on Gulf Stream model–data comparisons in basin-scale subtropical Atlantic Ocean models. *Dyn. Atmos. Ocean.*, **32 (3-4)**, 283–329, doi:10.1016/S0377-0265(00)00050-6.

Hutchinson, D. K., A. M. C. Hogg, and J. R. Blundell, 2010: Southern Ocean Response to Relative Velocity Wind Stress Forcing. *J. Phys. Oceanogr.*, **40 (2)**, 326–339, doi:10.1175/2009JPO4240.1.

Jin, X., C. Dong, J. Kurian, J. C. McWilliams, D. B. Chelton, and Z. Li, 2009: SST–Wind Interaction in Coastal Upwelling: Oceanic Simulation with Empirical Coupling. *J. Phys. Oceanogr.*, **39 (11)**, 2957–2970, doi:10.1175/2009JPO4205.1.

Kelly, K. A., S. Dickinson, M. J. McPhaden, and G. C. Johnson, 2001: Ocean currents evident in satellite wind data. *Geophys. Res. Lett.*, **28 (12)**, 2469–2472.

Kobayashi, S., and Coauthors, 2015: The JRA-55 Reanalysis: General Specifications and Basic Characteristics. *Journal of the Meteorological Society of Japan. Ser. II*, **93 (1)**, 5–48, doi:10.2151/jmsj.2015-001.

Large, W., and S. Yeager, 2004: Diurnal to Decadal Global Forcing For Ocean and Sea-Ice

Models : The Data Sets and Flux Climatologies. Tech. Rep. NCAR Technical Note NCAR/TN-460+STR. doi:10.5065/D6KK98Q6.

Large, W. G., J. C. McWilliams, and S. C. Doney, 1994: Oceanic vertical mixing: A review and a model with a nonlocal boundary layer parameterization. *Reviews of Geophysics*, **32 (4)**, 363, doi:10.1029/94RG01872.

Large, W. G., and S. Pond, 1981: Open Ocean Momentum Flux Measurements in Moderate to Strong Winds. 324–336 pp., doi:10.1175/1520-0485(1981)011⟨0324:OOMFMI⟩2.0.CO;2.

Large, W. G., and S. Pond, 1982: Sensible and Latent Heat Flux Measurements over the Ocean. *J. Phys. Oceanogr.*, **12 (5)**, 464–482, doi:10.1175/1520-0485(1982)012⟨0464:SALHFM⟩2.0.CO;2.

Large, W. G., and S. G. Yeager, 2009: The global climatology of an interannually varying air–sea flux data set. *Clim. Dyn.*, **33 (2-3)**, 341–364, doi:10.1007/s00382-008-0441-3.

Le Bars, D., W. P. M. De Ruijter, and H. A. Dijkstra, 2012: A New Regime of the Agulhas Current Retroflection: Turbulent Choking of Indian–Atlantic leakage. *J. Phys. Oceanogr.*, **42 (7)**, 1158–1172, doi:10.1175/JPO-D-11-0119.1.

Levitus, S., and Coauthors, 1998: World Ocean Database 1998. *NOAA Atlas NESDID18*, **1**.

Livezey, R. E., and W. Y. Chen, 1983: Statistical Field Significance and its Determination by Monte Carlo Techniques. *Mon. Weather Rev.*, **111 (1)**, 46–59, doi:10.1175/1520-0493(1983)111⟨0046:SFSAID⟩2.0.CO;2.

Lohmann, G., R. Gerdes, and D. Chen, 1996: Sensitivity of the thermohaline circulation in coupled oceanic GCM—atmospheric EBM experiments. *Clim. Dyn.*, **12 (6)**, 403–416, doi:10.1007/BF00211686.

Lorenz, E., 1955: Available potential energy and the maintenance of the general circulation. *Tellus*, **VII**, 157–167.

Loveday, B. R., J. V. Durgadoo, C. J. C. Reason, A. Biastoch, and P. Penven, 2014: Decoupling of the Agulhas Leakage from the Agulhas Current. *J. Phys. Oceanogr.*, **44 (7)**, 1776–1797, doi:10.1175/JPO-D-13-093.1.

Lutjeharms, J. R. E., and J. Cooper, 1996: Interbasin leakage through Agulhas current filaments. *Deep Sea Res. Part I Oceanogr. Res. P.*, **43 (2)**, 213–238, doi:10.1016/0967-0637(96)00002-7.

Ma, X., and Coauthors, 2016: Western boundary currents regulated by interaction between ocean eddies and the atmosphere. *Nature*, **535 (7613)**, 533–537, doi:10.1038/nature18640.

Madec, G., 2011: *NEMO ocean engine*. Tech. rep. ed., 27, Inst. Pierre-Simon Laplace (IPSL), France.

Mantua, N. J., S. R. Hare, Y. Zhang, J. M. Wallace, and R. C. Francis, 1997: A Pacific interdecadal climate oscillation with impacts on salmon production. *Bull. Am. Meteorol. Soc.*,

78 (6), 1069–1079.

Marsland, S. J., H. Haak, J. H. Jungclaus, M. Latif, and F. Röske, 2003: The Max-Planck-Institute global ocean/sea ice model with orthogonal curvilinear coordinates. *Ocean Model.*, **5 (2)**, 91–127, doi:10.1016/S1463-5003(02)00015-X.

Minobe, S., A. Kuwano-Yoshida, N. Komori, S.-P. Xie, and R. J. Small, 2008: Influence of the Gulf Stream on the troposphere. *Nature*, **452 (7184)**, 206–9, doi:10.1038/nature06690.

Moore, A. M., and C. Reason, 1993: The response of a global ocean general circulation model to climatological surface boundary conditions for temperature and salinity. *J. Phys. Oceanogr.*, **23**, 300–328, doi:http://dx.doi.org/10.1175/1520-0485(1993)023⟨0300:TROAGO⟩2.0.CO;2.

Moulin, A., and A. Wirth, 2016: Momentum Transfer Between an Atmospheric and an Oceanic Layer at the Synoptic and the Mesoscale: An Idealized Numerical Study. *Boundary-Layer Meteorol.*, 1–18, doi:10.1007/s10546-016-0153-x.

Müller, W. A., and Coauthors, 2018: A Higher-resolution Version of the Max Planck Institute Earth System Model (MPI-ESM1.2-HR). *Journal of Advances in Modeling Earth Systems*, 1–31, doi:10.1029/2017MS001217.

Okumura, Y., S. P. Xie, A. Numaguti, and Y. Tanimoto, 2001: Tropical Atlantic air-sea interaction and its influence on the NAO. *Geophys. Res. Lett.*, **28 (8)**, 1507–1510, doi:10.1029/2000GL012565.

Oliver, E. C. J., T. J. O'Kane, and N. J. Holbrook, 2015: Projected changes to Tasman Sea eddies in a future climate. *J. Geophys. Res. Ocean.*, **120 (11)**, 7150–7165, doi:10.1002/2015JC010993.

Østerhus, S., W. R. Turrell, S. Jónsson, and B. Hansen, 2005: Measured volume, heat, and salt fluxes from the Atlantic to the Arctic Mediterranean. *Geophys. Res. Lett.*, **32 (7)**, 1–4, doi:10.1029/2004GL022188.

Pacanowski, R. C., 1987: Effect of Equatorial Currents on Surface Stress. *J. Phys. Oceanogr.*, **17 (6)**, 833–838, doi:10.1175/1520-0485(1987)017⟨0833:EOECOS⟩2.0.CO;2.

Pacanowski, R. C., and S. M. Griffies, 2000: MOM 3.0 Manual. Tech. rep., 3–6 pp.

Paiva, A., and E. Chassignet, 2001: The impact of surface flux parameterizations on the modeling of the North Atlantic Ocean. *J. Phys. Oceanogr.*, 1860–1879, doi:10.1175/1520-0485(2001)031⟨1860:TIOSFP⟩2.0.CO;2.

Perlin, N., E. D. Skyllingstad, R. M. Samelson, and P. L. Barbour, 2007: Numerical Simulation of Air–Sea Coupling during Coastal Upwelling. *J. Phys. Oceanogr.*, **37 (8)**, 2081–2093, doi:10.1175/JPO3104.1.

Pezzi, L. P., J. Vialard, K. J. Richards, C. Menkes, and D. Anderson, 2004: Influence of ocean-atmosphere coupling on the properties of tropical instability waves. *Geophys. Res. Lett.*,

31 (16), 4–7, doi:10.1029/2004GL019995.

Power, S. B., and R. Kleeman, 1994: Surface heat flux parameterization and the response of ocean general circulation models to high-latitude freshening. *Tellus. Series A: Dynamic Meteorology and Oceanography*, **0870**, 46A(1), 86–95, January 1994, doi:10.3402/tellusa.v46i1.15437.

Rahmstorf, S., and J. Willebrand, 1995: The Role of Temperature Feedback in Stabilizing the Thermohaline Circulation. *J. Phys. Oceanogr.*, **25 (5)**, 787–805, doi:10.1175/1520-0485(1995) 025⟨0787:TROTFI⟩2.0.CO;2.

Rath, W., R. J. Greatbatch, and X. Zhai, 2013: Reduction of near-inertial energy through the dependence of wind stress on the ocean-surface velocity. *J. Phys. Ocean.*, **118 (6)**, 2761–2773, doi:10.1002/jgrc.20198.

Renault, L., A. Hall, and J. C. McWilliams, 2016a: Orographic shaping of US West Coast wind profiles during the upwelling season. *Clim. Dyn.*, **46 (1-2)**, 273–289, doi:10.1007/ s00382-015-2583-4.

Renault, L., J. C. McWilliams, and S. Masson, 2017a: Satellite Observations of Imprint of Oceanic Current on Wind Stress by Air-Sea Coupling. *Sci. Rep.*, **7 (1)**, 17 747, doi:10.1038/ s41598-017-17939-1.

Renault, L., J. C. McWilliams, and P. Penven, 2017b: Modulation of the Agulhas Current Retroflection and Leakage by Oceanic Current Interaction with the Atmosphere in Coupled Simulations. *J. Phys. Oceanogr.*, **47 (8)**, 2077–2100, doi:10.1175/JPO-D-16-0168.1.

Renault, L., M. J. Molemaker, J. Gula, S. Masson, and J. C. McWilliams, 2016b: Control and Stabilization of the Gulf Stream by Oceanic Current Interaction with the Atmosphere. *J. Phys. Oceanogr.*, **46 (11)**, 3439–3453, doi:10.1175/JPO-D-16-0115.1, arXiv:1203.2692v4.

Renault, L., M. J. Molemaker, J. C. McWilliams, A. F. Shchepetkin, F. Lemarié, D. Chelton, S. Illig, and A. Hall, 2016c: Modulation of Wind Work by Oceanic Current Interaction with the Atmosphere. *J. Phys. Oceanogr.*, **46 (6)**, 1685–1704, doi:10.1175/JPO-D-15-0232.1, arXiv:1203.2692v4.

Ricciardulli, L., and F. Wentz, 2011: Reprocessed QuikSCAT (V04) wind vectors with Ku-2011 geophysical model function. *Remote Sensing Systems Technical Report*, 1–8.

Richardson, P. L., 2007: Agulhas leakage into the Atlantic estimated with subsurface floats and surface drifters. *Deep Sea Res. Part I Oceanogr. Res. P.*, **54 (8)**, 1361–1389, doi:10.1016/j. dsr.2007.04.010.

Roberts, M. J., H. T. Hewitt, P. Hyder, D. Ferreira, S. A. Josey, M. Mizielinski, and A. Shelly, 2016: Impact of ocean resolution on coupled air-sea fluxes and large-scale climate. *Geophys. Res. Lett.*, **43 (19)**, 10,430–10,438, doi:10.1002/2016GL070559.

Rong-hua, Z., 2013: Remote Effects of Tropical Cyclone Wind Forcing over. *Advances in Atmo-*

spheric Sciences, **30 (6)**, 1507–1525, doi:10.1007/s00376-013-2283-0.1.Introduction.

Samelson, R. M., E. D. Skyllingstad, D. B. Chelton, S. K. Esbensen, L. W. O'Neill, and N. Thum, 2006: On the coupling of wind stress and sea surface temperature. *J. Clim.*, **19 (8)**, 1557–1566, doi:10.1175/JCLI3682.1.

Schoonover, J., W. K. Dewar, N. Wienders, and B. Deremble, 2017: Local Sensitivities of the Gulf Stream Separation. *J. Phys. Oceanogr.*, **47 (2)**, 353–373, doi:10.1175/JPO-D-16-0195.1.

Schoonover, J., and Coauthors, 2016: North Atlantic Barotropic Vorticity Balances in Numerical Models. *J. Phys. Oceanogr.*, **46 (1)**, 289–303, doi:10.1175/JPO-D-15-0133.1.

Scott, R. B., and Y. Xu, 2009: An update on the wind power input to the surface geostrophic flow of the World Ocean. *Deep Sea Res. Part I Oceanogr. Res. P.*, **56 (3)**, 295–304, doi: 10.1016/j.dsr.2008.09.010.

Seager, R., M. B. Blumenthal, and Y. Kushnir, 1995: An Advective Atmospheric Mixed Layer Model for Ocean Modeling Purposes: Global Simulation of Surface Heat Fluxes. *J. Clim.*, **8 (8)**, 1951–1964, doi:10.1175/1520-0442(1995)008⟨1951:AAAMLM⟩2.0.CO;2.

Seo, H., A. J. Miller, and J. R. Norris, 2016: Eddy-wind interaction in the California Current System: dynamics and impacts. *Journal of Physical Oceanography*, **(1989)**, 151130150615 002, doi:10.1175/JPO-D-15-0086.1.

Shuckburgh, E., G. Maze, D. Ferreira, J. Marshall, H. Jones, and C. Hill, 2011: Mixed Layer Lateral Eddy Fluxes Mediated by Air–Sea Interaction. *Journal of Physical Oceanography*, **41 (1)**, 130–144, doi:10.1175/2010JPO4429.1.

Small, R., and Coauthors, 2008: Air–sea interaction over ocean fronts and eddies. *Dyn. Atmos. Ocean.*, **45 (3-4)**, 274–319, doi:10.1016/j.dynatmoce.2008.01.001.

Smith, R. D., M. E. Maltrud, F. O. Bryan, and M. W. Hecht, 2000: Numerical Simulation of the North Atlantic Ocean at 1/10°. *J. Phys. Oceanogr.*, **30 (7)**, 1532–1561, doi:10.1175/1520-0485(2000)030⟨1532:NSOTNA⟩2.0.CO;2.

Smith, S. D., 1988: Coefficients for sea surface wind stress, heat flux, and wind profiles as a function of wind speed and temperature. *J. Geophys. Res. Ocean.*, **93 (C12)**, 15 467–15 472, doi:10.1029/JC093iC12p15467.

Spall, M. a., 2007: Midlatitude Wind Stress–Sea Surface Temperature Coupling in the Vicinity of Oceanic Fronts. *J. Clim.*, **20 (15)**, 3785–3801, doi:10.1175/JCLI4234.1.

Sprintall, J., S. E. Wijffels, R. Molcard, and I. Jaya, 2009: Direct estimates of the indonesian throughflow entering the indian ocean: 2004-2006. *J. Geophys. Res. Ocean.*, **114 (7)**, 2004–2006, doi:10.1029/2008JC005257.

Storto, A., M. J. Martin, B. Deremble, and S. Masina, 2018: Strongly coupled data assimilation experiments with linearized ocean-atmosphere balance relationships. *Mon. Wea. Rev.*, MWR–

D–17–0222.1, doi:10.1175/MWR-D-17-0222.1.

Treguier, A. M., O. Boebel, B. Barnier, and G. Madec, 2003: Agulhas eddy fluxes in a 1/6° Atlantic model. *Deep Sea Res. Part II Top. Stud. Oceanogr.*, **50 (1)**, 251–280, doi:10.1016/S0967-0645(02)00396-X.

Treguier, A. M., C. Lique, J. Deshayes, and J. M. Molines, 2017: The North Atlantic Eddy Heat Transport and Its Relation with the Vertical Tilting of the Gulf Stream Axis. *J. Phys. Oceanogr.*, **47 (6)**, 1281–1289, doi:10.1175/JPO-D-16-0172.1.

Trenberth, K. E., J. T. Fasullo, and J. Kiehl, 2009: Earth's Global Energy Budget. *Bull. Amer. Meteor. Soc.*, **90 (3)**, 311–323, doi:10.1175/2008BAMS2634.1.

Troen, I. B., and L. Mahrt, 1986: A simple model of the atmospheric boundary layer; sensitivity to surface evaporation. *Boundary-Layer Meteorol.*, **37 (1-2)**, 129–148, doi:10.1007/BF00122760, arXiv:1011.1669v3.

Tsujino, H., and Coauthors, 2018: JRA-55 based surface dataset for driving ocean - sea-ice models (JRA55-do). *Ocean Model.*, doi:10.1016/j.ocemod.2018.07.002.

Visbeck, M., H. Cullen, G. Krahmann, and N. Naik, 1998: An ocean model's response to North Atlantic Oscillation-ike wind forcing. *Geophys. Res. Lett*, **25 (24)**, 4521–4524, doi:0094-8276/98/1998GL900162505.00.

von Storch, J.-S., C. Eden, I. Fast, H. Haak, D. Hernández-Deckers, E. Maier-Reimer, J. Marotzke, and D. Stammer, 2012: An Estimate of the Lorenz Energy Cycle for the World Ocean Based on the STORM/NCEP Simulation. *J. Phys. Oceanogr.*, **42 (12)**, 2185–2205, doi:10.1175/JPO-D-12-079.1.

Wallace, J. M., T. P. Mitchell, and C. Deser, 1989: The Influence of Sea-Surface Temperature on Surface Wind in the Eastern Equatorial Pacific: Seasonal and Interannual Variability. 1492–1499 pp., doi:10.1175/1520-0442(1989)002⟨1492:TIOSST⟩2.0.CO;2.

Walters, D., and Coauthors, 2017: The Met Office Unified Model Global Atmosphere 6.0/6.1 and JULES Global Land 6.0/6.1 configurations. *Geoscientific Model Development*, **10 (4)**, 1487–1520, doi:10.5194/gmd-10-1487-2017.

Wang, C., L. Zhang, S. K. Lee, L. Wu, and C. R. Mechoso, 2014: A global perspective on CMIP5 climate model biases. *Nat. Clim. Chang.*, **4 (3)**, 201–205, doi:10.1038/nclimate2118.

Wang, X., and S. S. Shen, 1999: Estimation of spatial degrees of freedom of a climate field. *J. Clim.*, **12 (5 I)**, 1280–1291, doi:10.1175/1520-0442(1999)012⟨1280:EOSDOF⟩2.0.CO;2.

Wiggert, J. D., R. G. Murtugudde, and J. R. Christian, 2006: Annual ecosystem variability in the tropical Indian Ocean: Results of a coupled bio-physical ocean general circulation model. *Deep Sea Res. Part II Top. Stud. Oceanogr.*, **53 (5-7)**, 644–676, doi:10.1016/j.dsr2.2006.01.027.

Wild, M., and Coauthors, 2015: The energy balance over land and oceans: an assessment based

on direct observations and CMIP5 climate models. *Clim. Dyn.*, **44 (11-12)**, 3393–3429, doi: 10.1007/s00382-014-2430-z.

Winton, M., S. M. Griffies, B. L. Samuels, J. L. Sarmiento, and T. L. Licher, 2013: Connecting changing ocean circulation with changing climate. *J. Clim.*, **26 (7)**, 2268–2278, doi:10.1175/ JCLI-D-12-00296.1.

Woodgate, R. a., T. J. Weingartner, and R. Lindsay, 2012: Observed increases in Bering Strait oceanic fluxes from the Pacific to the Arctic from 2001 to 2011 and their impacts on the Arctic Ocean water column. *Geophys. Res. Lett.*, **39 (24)**, 2–7, doi:10.1029/2012GL054092.

Xie, S. P., 2004: Satellite observations of cool ocean-atmosphere interaction. *Bull. Amer. Meteor. Soc.*, **85 (2)**, 195–208, doi:10.1175/BAMS-85-2-195.

Xu, C., X. Zhai, and X. D. Shang, 2016: Work done by atmospheric winds on mesoscale ocean eddies. *Geophys. Res. Lett.*, **43 (23)**, 12,174–12,180, doi:10.1002/2016GL071275.

Xu, Y., and R. B. Scott, 2008: Subtleties in forcing eddy resolving ocean models with satellite wind data. *Ocean Model.*, **20 (3)**, 240–251, doi:10.1016/j.ocemod.2007.09.003.

Yu, L., X. Jin, and R. A. Weller, 2008: Multidecade Global Flux Datasets from the Objectively Analyzed Air-sea Fluxes (OAFlux) Project: Latent and sensible heat fluxes, ocean evaporation, and related surface meteorological variables. Tech. Rep. January, 64 pp. doi: 10.1007/s00382-011-1115-0.

Zhai, X., and R. J. Greatbatch, 2007: Wind work in a model of the northwest Atlantic Ocean. *Geophys. Res. Lett.*, **34 (4)**, 1–4, doi:10.1029/2006GL028907.

Zhang, R. H., 2015: A hybrid coupled model for the pacific ocean-atmosphere system. Part I: Description and basic performance. *Advances in Atmospheric Sciences*, **32 (3)**, 301–318, doi:10.1007/s00376-014-3266-5.

Danksagung

Selbstständigkeitserklärung

Hiermit erkläre ich an Eides statt, dass ich die vorliegende Dissertation - abgesehen von der Beratung durch meinen Betreuer Prof. Dr. Claus Böning - selbstständig und ohne fremde Hilfe angefertigt, keine anderen als die angegebenen Quellen und Hilfsmittel benutzt und die den benutzten Quellen wörtlich oder inhaltlich entnommenen Stellen als solche kenntlich gemacht habe. Kapitel 3 dieser Arbeit ist in Ocean Science Discussion veröffentlicht. Die gekoppelten Modellläufe in Kapitel 2 und 3 sind mir von Helene Hewitt und Malcolm Roberts zur Verfügung gestellt worden. Kapitel 5 dieser Arbeit ist mit Hilfe von Torge Martin entstanden.

Diese Arbeit hat in gleicher oder ähnlicher Form noch keiner Prüfungsbehörde vorgelegen. Sie ist unter Einhaltung der Regeln guter wissenschaftlicher Praxis der Deutschen Forschungsgemeinschaft entstanden.

Kiel, 2018 _____

Rafael Abel